ALGORITHMS AND SOFTWARE TOOLS FOR EXTRACTING COASTAL MORPHOLOGICAL INFORMATION FROM AIRBORNE LiDAR DATA

A Thesis

by

YIGE GAO

Submitted to the Office of Graduate Studies of
Texas A&M University
in partial fulfillment of the requirements for the degree of

MASTER OF SCIENCE

May 2009

Major Subject: Geography

ALGORITHMS AND SOFTWARE TOOLS FOR EXTRACTING COASTAL MORPHOLOGICAL INFORMATION FROM AIRBORNE LiDAR DATA

A Thesis

by

YIGE GAO

Submitted to the Office of Graduate Studies of
Texas A&M University
in partial fulfillment of the requirements for the degree of

MASTER OF SCIENCE

Approved by:

Chair of Committee,	Hongxing Liu
Committee Members,	Andrew Millington
	Xinyuan Ben Wu
Head of Department,	Douglas J. Sherman

May 2009

Major Subject: Geography

ABSTRACT

Algorithms and Software Tools for Extracting Coastal Morphological Information from Airborne LiDAR Data. (May 2009)

Yige Gao, B.S.; B.S., Peking University, Beijing, China

Chair of Advisory Committee: Dr. Hongxing Liu

With the ever increasing population and economic activities in coastal areas, coastal hazards have become a major concern for coastal management. The fundamental requirement of coastal planning and management is the scientific knowledge about coastal forms and processes. This research aims at developing algorithms for automatically extracting coastal morphological information from LiDAR data. The primary methods developed by this research include automated algorithms for beach profile feature extraction and change analysis, and an object-based approach for spatial pattern analysis of coastal morphologic and volumetric change.

Automated algorithms are developed for cross-shore profile feature extraction and change analysis. Important features of the beach profile such as dune crest, dune toe, and beach berm crest are extracted automatically by using a scale-space approach and by incorporating contextual information. The attributes of important feature points and segments are derived to characterize the morphologic properties of each beach profile. Beach profiles from different time periods can be compared for morphologic and volumetric change analysis.

An object-oriented approach for volumetric change analysis is developed to identify and delineate individual elevation change patches as discrete objects. A set of two-dimensional and three-dimensional attributes are derived to characterize the objects, which includes planimetric attributes, shape attributes, surface attributes, volumetric attributes, and summary attributes.

Both algorithms are implemented as ArcGIS extension modules to perform the feature extraction and attribute derivation for coastal morphological change analysis. To demonstrate the utility and effectiveness of algorithms, the cross-shore profile change analysis method and software tool are applied to a case study area located at southern Monterey Bay, California, and the coastal morphology change analysis method and software tool are applied to a case study area located on Assateague Island, Maryland.

The automated algorithms facilitate the efficient beach profile feature analysis over large geographical area and support the analysis of the spatial variations of beach profile changes along the shoreline. The explicit object representation of elevation change patches makes it easy to localize erosion hot spots, to classify the elevation changes caused by various mechanisms, and to analyze spatial pattern of morphologic and volumetric changes.

DEDICATION

Dedicated to

My parents

ACKNOWLEDGMENTS

I would like to express my greatest gratitude to my advisor, Dr. Hongxing Liu. Your patient guidance and unceasing encouragement helped me to push my way along this research journey. I could never achieve this point without your guidance both in research and in life attitude.

Thanks to my committee members Dr. Andrew Millington and Dr. Xinyuan Ben Wu for your insightful advice and valuable comments on this research.

Thanks to Dr. Jinfeng Wang and all my colleagues in Lab201 back in China – I enjoyed all the time we spend together. Without your help and encouragement, I wouldn't have had the opportunity to be in this land of America.

Thanks to Dean, Zichuan, and everyone in water resources team in ESRI — I never expected such a wonderful internship and such a friendly working environment. Thanks for all your patient guidance in helping me to learn about hydrological and hydraulic modeling.

Thanks to Lei Wang, Sheng-jung Tang, and Zengwang Xu for all the wonderful time we spent together and your endless help and encouragement after graduation. Thanks to my good friends in Texas A&M: Bailiang Li, Li Li, Haibin Su, Bing-Sheng Wu, Rahul, Luti, Shinichi, Alehe, Iliyana, and Cara for your big-hearted support and all the fun time we shared during the past two years. Thanks to Songgang Gu and Zheng Cheng – I understand your choice and hope you have a bright future.

I also would like to share my joy and happiness with my dear friends Qian Di, Dong Han, Bin Leng, Xin Jin, and Shuangshi Yin in China, for their consistent understanding and encouragement during all these years, no matter where I am.

Last, but most important, I want to thank my parents for being such a wonderful example, teaching me to be a trustworthy person, be true to friends, be responsible for work, and always be positive towards life. Thanks for your endless love and support.

TABLE OF CONTENTS

Page

Page

LIST OF FIGURES

Page

Page

Page

LIST OF TABLES

Page

1 INTRODUCTION

1.1 Background

Coastal areas sustain a wealth of natural resources and economic activities. More than half of the world's population currently lives within 60 km of the coastline, and the coastal concentration of population is expected to increase dramatically in the future (CCSR, 2006). In the U.S., it is estimated approximately 53% percent of the nation's population lived in coastal counties in 2003, which is expected to increase by 12 million by 2015 (Crossett et al., 2004). With the ever increasing population and economic activities in coastal areas, coastal hazards have become a major concern for coastal management. The fundamental requirement of coastal management and planning is the scientific knowledge about coastal morphology and processes. The information about the coastal morphology change could facilitate decision-makers to better understand coastal process, to assess and predict the impacts of coastal hazards, and to formulate better management decisions regarding sustainable coastal developments.

Traditionally, coastal mapping has been based on ground surveys of transects perpendicular and parallel to the shoreline. In most cases it is time-consuming and labor-intensive. Transects are usually widely spaced due to time and cost restrictions. In recent years, airborne LiDAR remote sensing technology has been widely used in surveying, mapping and monitoring coastal environmental conditions and changes. LiDAR technique provides a much more cost-effective and efficient means of collecting topographic information, which allows a detailed analysis of micro-geomorphology of

---

This thesis follows the style of *Annals of the Association of American Geographers.*

the coastal area over a broad region (White and Wang, 2003; Brock et al., 2004; Zhang et al., 2005; Finkl et al., 2005). The technological advancements present both opportunities and challenges. One of the major challenges brought by the LiDAR technology is to develop methods to fully explore high resolution LiDAR data for information and knowledge extraction.

Cross-shore profile change analysis provides an important dimension in understanding morphological and volumetric changes in coastal area. Beach profiles can be extracted from the LiDAR surveys at a much higher resolution than those from traditional ground-based surveys for detailed change analysis (Brock et al., 2004). The available analytical techniques for beach profile change analysis include the comparison of successive surveys in terms of beach height, width, gradient, and shape, as well as the beach profile areas and volumes (Cooper et al., 2000). However, previous studies are primarily based on the visual interpretation of profiles and simple statistical analysis for extracting morphologic features of beach profiles such as dune crests and toes (Elko et al., 2002; Judge et al., 2003; Zhang et al., 2005; Gares et al., 2006; Robertson et al., 2007). This research intends to develop automated algorithms for extracting cross-shore profiles, identifying critical points, and calculating important cross-shore morphological properties from LiDAR data.

Information about spatial patterns of erosion and deposition and corresponding volumetric changes of the coastal zone are important for coastal hazard evaluation and coastal management. Previously, a cell-by-cell differencing method was commonly used for the volumetric change analysis based on LiDAR surveys (Woolard and Colby, 2002;

White and Wang, 2003; Shrestha et al., 2005; Zhang et al., 2005; Gares et al., 2006). The volume change is evaluated on a cell-by-cell basis by subtracting the LiDAR DEM acquired at an earlier time from the LiDAR DEM acquired at a later time. However, such an approach suffers from the difficulty in deriving localized information to analyze spatial patterns of morphologic and volumetric changes. It is also difficult to recognize elevation changes induced by factors other than erosion and deposition. In addition, it is not convenient with the cell-by-cell differencing method to associate the volumetric change information with other data for interpreting the causes and impacts of volumetric changes. This research aims to develop an object-based approach to morphologic and volumetric change analysis, which explicitly identifies each individual erosion and deposition patch as discrete object, and derive a set of spatial and volumetric attributes to characterize each object.

1.2 Objectives

The general goal of this research is to develop algorithms for automatically extracting coastal morphological change information. Specific objectives include:

- Develop automated algorithms for beach profile feature extraction and change analysis
- Develop an object-based approach for coastal morphological and volumetric change analysis
- Implement software tools for coastal morphological change analysis
- Test and validate coastal morphological change analysis methods for case study areas

1.3 Methodology

1.3.1 Automated feature extraction and change analysis for cross-shore profiles

This research will develop numerical algorithms for cross-shore profile feature extraction and change analysis based on repeat LiDAR data. Beach profiles perpendicular to the shoreline will be automatically generated at a given interval. The Gaussian filter will be applied to smooth the beach profiles. Slope and curvature values will be calculated for different sections of the beach profile. The dune crest and toe, as well as the beach berm crest will be identified based on the slope and curvature values. The attributes such as slopes for dune face and beach, as well as the heights and horizontal positions for dune crest and berm crest will be derived to characterize the morphologic properties of beach profile. To refine and improve the computation results from individual profiles, which are usually noisy, the contextual information of adjacent profiles are incorporated in the computation. The beach profiles from successive LiDAR surveys are compared for morphological and volumetric change analysis. This automated profile analysis method will be implemented as ArcGIS extension module to perform the feature extraction and attribute derivation from LiDAR beach profiles.

1.3.2 Object-based morphological and volumetric change analysis

This research will develop an object-based approach for volumetric change analysis using repeat LiDAR data. This approach automatically identifies and delineates individual erosion and deposition patches as discrete objects. These erosion and deposition objects, instead of individual cells in the elevation differencing grid, are used as basic spatial units for volumetric analysis. A set of two-dimensional and three-

dimensional attributes will be derived to characterize and quantify erosion and deposition objects, which includes planimetric attributes, shape attributes, volumetric attributes, and summary statistical attributes. The explicit object representation of erosion and deposition patches makes it easy to localize hot spots, to analyze spatial pattern of morphologic and volumetric changes, to discriminate the erosion and deposition caused by different factors, and to incorporate other GIS data to explore the causes and impacts of the changes. This method will be implemented as an ArcGIS extension module to perform the object identification and attribute derivation.

1.4 Organization of the thesis

This thesis consists of six sections. The present section introduces the research background, objectives, and methodology.

Section 2 reviews the existing coastal topography mapping techniques, the pixel-based method for coastal morphological and volumetric analysis, and the existing methods and softwares for feature extraction and change analysis of beach profile.

Section 3 introduces the airborne LiDAR remote sensing system and basic data products, and discusses the workflow for LiDAR data preprocessing.

Section 4 presents the automated method for beach profile feature extraction and attribute derivation, as well as the approach for profile change analysis based on sequential LiDAR data.

Section 5 presents the object-based method, which includes the identification and delineation of erosion and deposition objects, as well as the derivation of attributes for characterizing these objects.

Section 6 applies the change analysis method described in Section 4 and Section 5 to case study areas.

The last section summarizes the research findings and discusses the future research directions.

2 LITERATURE REVIEW

This section reviews the coastal mapping techniques and discusses the comparative advantages of airborne LiDAR technology. The pixel-based approach for coastal morphological and volumetric analysis is introduced and its limitations are discussed. In addition, the visual interpretation and conventional methods for feature extraction from beach profiles, and the existing change analysis methods and software tools are reviewed and summarized.

2.1 Coastal topography mapping techniques

The coastal topography measurements are required by many studies such as coastal flood forecasting, coastal defence structure design against flooding and erosion, coastal environmental management, and environment impact assessment for economic exploitation (Mason et al., 2000). Traditionally, coastal topography mapping is based on methods such as ground survey and photogrammetry. In recent years, the development of airborne LiDAR remote sensing technology provides a much more cost-effective and efficient method to acquire elevation information in coastal area.

Ground surveys for coastal areas are usually based on transects perpendicular and/or parallel to the shoreline. The elevation measurements along transects are acquired by using instruments such as engineer's levels, total stations, or Global Positioning System (GPS) instruments (Cooper et al., 2000). The ground surveys can obtain highly accurate elevation measurements along transects and are repeatable at different time periods, which is necessary for change analysis. The topography of the near-shore zones

can be monitored by extending transects below water surface. However, in most cases this method is time-consuming and labor-intensive. When a large area needs to be covered, it means either a significant increase in cost, time, and labor to measure sufficient number of transects to represent the topography, or a sparse sampling rate, which may not be representative of the topography in details, and thus compromise the objective of study. In addition, the ground surveys are always constrained by the tidal and weather conditions, as well as the safety and accessibility of the survey area.

The photogrammetric approach extracts the elevation information from stereoscopic aerial photography. By acquiring aerial photographs from different vantage view points of the landscape, the elevation measurements of the terrain surface in the overlapping areas of multiple photographs could be calculated based on stereoscopic parallax, which is the change of its viewing position from one photograph to the next relative to its background. The resulting digital elevation model (DEM) derived by photogrammetric approach could be at various scales (Jensen, 2007). This method could derive highly accurate elevation measurements and the data collection is repeatable. Depending on the required flying scale and level of accuracy, the cost could vary for both flying and image interpretation. Compared to ground survey methods, stereoscopic aerial photography could cover a large area with much better spatial resolution. However, the difficulty in identifying match points on featureless areas like beaches and dunes has seriously hindered photogrammetry application in coastal areas (Mason et al., 2000). The elevation extraction process from photogrammetry is relatively costly and time consuming. It cannot obtain the elevation measurements under water and cannot be used

for topography mapping in the near-shore zone. The flying missions are seriously constrained by weather and lighting conditions.

The airborne LiDAR technology is based on accurate measurements of the laser pulse travel time from the transmitter to the target and back to the receiver. The laser scanner sends thousands of laser beams per second to the ground. Using the sensor position derived from differential Global Positioning System (GPS) and the sensor orientation derived from Inertial Measurement Unit (IMU), the laser range measurements can be converted to highly accurate elevation values. For coastal topography mapping, most LiDAR systems use near-infrared laser light in the region from 1045 to 1065 nm, which may also be used for mapping topography in the near-shore zone depending on the water clarity. The LiDAR techniques could achieve high vertical accuracy of approximately 15 cm and horizontal accuracy of less than 1m (NOAA, 2008). Compared to ground surveys and photogrammetric data, LiDAR data can be collected at night if necessary because it is an active system and does not rely on the solar illumination. The requirements of LiDAR system for weather and lighting conditions are not as strict as that of aerial photography, and the data processing procedure is much simpler and more efficient. Overall, it provides a cost-effective and efficient way to collect detailed elevation measurements over a large coastal region.

2.2 Methods and software for beach profile feature extraction and change analysis

Beach profile surveying is a long-established and widely used technique for coastal monitoring. Cooper et al. (2000) provided a summary of the key elements of the beach

profile measurement, theory and analysis. They classified the beach profile change analysis methods into two categories: temporal analytical methods that assesses changes along one particular beach profile with respect to time, and spatial analytical methods that assesses variations between different profiles. The temporal analytical method can be used to identify the shore-term variation and long-term trends at a specific location and the spatial analytical method can be used to determine the spatial pattern of beach profile changes along the coastline. They summarized the available analytical techniques for comparison of successive surveys along a beach profile. The profiles can be compared in terms of beach level and width, which are regarded as the standard of natural coastal defence. Also, the profiles can be compared in terms of beach gradient to understand the trends for beach steepening or flattening, and in terms of beach profile areas and volumes to evaluate the 'health' of beach.

Most of the previous studies used visual interpretation approach to extract morphological features from beach profiles. In recent years, some efforts have been made to develop numerical methods to identify and extract features from beach profiles. Brock et al. (2004) developed LiDAR metrics for barrier island elevation profiles to analyze morphological changes. For each LiDAR-based cross-shore profile, they determined the ocean shoreline point, bay shoreline point, and the volume balanceline point. The LiDAR change metrics were developed to describe the ocean shoreline displacement, bay shoreline displacement, volume balanceline displacement, and the slice volume change. A morphodynamic classification was presented based on LiDAR change metrics. To support a storm impact scaling model for analyzing dune

vulnerability to storm-induced erosion (Sallenger, 2000), a semi-automated algorithm was developed for extracting dune crest and dune toe from LiDAR data (Elko et al., 2002). First, the approximate locations of the dune crest and toe line had to be digitized manually. The dune crest line or berm crest line were visually recognized and manually digitized from the aspect image as the transition line from seaward-sloping to landward-sloping regions. The dune base line was delineated from the slope image as the transition line between the flat beach and the steep dune face. The authors pointed out that the dune base delineation were generally more difficult because there might not be distinct break between dune face and beach. Then, a searching algorithm was utilized to automatically determine the actual heights of dune crests and toes within a buffer around the digitized line. To obtain the dune crest height, a neighborhood function was applied to select the pixel with maximum elevation value within the 7 m wide buffer around the digitized dune crest line. To avoid small perturbations with rapidly changing slopes near the dune toe, a smaller buffer area of 3-m wide was created around the digitized dune toe line, and a neighborhood function was applied to select the pixel with maximum value of the second derivative of elevation as the dune toe pixel. Stockdon et al. (2007) adopted this method to identify the pre-storm elevation of the dune crest and toe, which were used in conjunction with expected water levels to predict the spatially-varying storm-impact regime.

A quantitative method has been developed by USGS Center for Costal and Regional Marine Studies to automatically extract the location and elevation of the “first line of defense”, which could be the dune crest/ beach berm, or the top of the coastal

defense structures (USGS, 2008). First, this method smoothes the profile extracted from LiDAR data so as to eliminate the small variations in elevation measurements. Second, elevation peaks are identified based on the changes in direction of slope, and the “first line of defense” is identified as the first elevation peak landward of the shoreline on the profiles.

Coastal morphology analysis software such as the Beach Morphology Analysis Package (BMAP) (Wise, 1995) and Regional Morphology Analysis Package (RMAP) (Batten and Kraus, 2005) have been widely used by coastal community. Both of them are part of the Coastal Engineering Design and Analysis System (CEDAS), which is an interactive coastal design and analysis software developed by the U.S. Army Engineer Waterways Experiment Station (Veri-Tech, 2006). CEDAS includes four modules: the General module contains the numerical methods for coastal and hydraulic engineering applications, the Inlet module contains the models for tidal inlet analysis, the Beach module contains the tools for beach process analysis, and the Surface-water Modeling System is a graphical user environment for accessing a multi-dimensional hydrodynamic model ADCIRC and a variety of multi-dimensional surface water modeling programs.

Beach Morphology Analysis Package (BMAP) is an integrated set of interactive tools developed to support the analysis of the morphologic and dynamic properties of beach profiles. It is dynamically linked with SBEACH (Storm-induced BEAch CHange), which simulates cross-shore beach, berm, and dune erosion. The capabilities of BMAP in analyzing static properties of profiles include (Wise, 1995): plotting individual or multiple beach profile surveys, averaging multiple profile surveys within a given spatial

range, generating best-fit equilibrium profile for a single grain size, calculating profile volume with respect to specified reference elevation along the profile, generating synthetic profiles, as well as calculating bar properties such as minimum depth and location, maximum height and location, volume, and the center of mass. As for the beach profile change analysis, the capabilities of BMAP include: determining cut and fill areas with respect to cross-shore distance, calculating volume change and elevation change between two successive profiles, and calculating cross-shore sand transport rate by integrating the equation for conservation of sand.

The Regional Morphology Analysis Package (RMAP), which is evolved from BMAP, also belongs to the Beach module of CEDAS (Batten and Kraus, 2005). While BMAP is limited in distance-elevation space, RMAP can manipulate, visualize, and analyze shoreline data and beach profiles spatially. Particularly, the shoreline positions and beach profiles can be projected and displayed on aerial photographs or maps. Data can be examined in both beach profile view and map view, which facilitates the quality control, visualization, and analysis process. RMAP has the capability to import beach profiles, shorelines, and baselines data from ASCII files, BMAP files, and spreadsheets. It can also import shorelines and baselines from ESRI Shapefiles. Since the distance and elevation values of each point along the profile are required to analyze the beach morphology, RMAP can calculate the distance from the known profile origin coordinates for each point along the transect using its XY coordinates. In order to locate points along the profile on the map, RMAP can also calculate the XY coordinates for each point using its distance and elevation values.

The Beach Profile Analysis Toolbox (BPAT) is a software for archiving, viewing, and analyzing beach profile information, which has been developed by the National Institute of Water and Atmospheric Research (NIWA) and Katoa Software in New Zealand. It includes an Archive mode and an Analysis mode. The Archive mode is used to view existing data and enter new data. The surveys within a study area are arranged hierarchically by regions, cross-sections, and the benchmarks. The Analysis mode is used to analyze beach profiles, which supports plotting groups of surveys for a specified cross section, aligning surveys at a given elevation or on the basis of common marker, calculating the slope and volume for each horizontal slice for selected single survey by choosing a starting elevation and an elevation increment, calculating the slope and volume for each vertical slice for selected single survey by choosing a starting offset and an offset increment, and calculating cut/fill volume of surveys taken at different times.

The Shoreline and Nearshore Data System (SANDS) is a coastal data capture, monitoring and analysis software developed by Halcrow Group Ltd, UK (Halcrow, 2008). It is capable of importing beach profile survey data as well as time series wave, wind or tide level records. In SANDS, beach profile surveys can be analyzed using different methods. The standard beach profile analysis method include the “chainage” method, which works by dividing profile into vertical sections and calculating the beach level at each section, and the “level” method which looks at the horizontal strips of profile. In addition, SANDS can calculate the cross-sectional areas and volumes in relation to a ‘master profile’, which is a rock or clay bed layer under the beach material. As for volumetric analysis, SANDS enables the ability to group specific beach profile

locations to form a “Coastal Process Unit” and calculate volumes of beach materials for these units. In SANDS, maps can be imported as backdrop for reference and may also have data attached to it. However, SANDS is not a GIS system and the map data needs to be prepared using other GIS software.

The visual interpretation of beach profile extracted from LiDAR data provides an intuitive way to analyze the beach morphological change. Despite the recent development of semi-automated algorithms, more efficient and accurate methods are needed for automatically extracting beach profiles, identifying critical points, calculating important morphological properties, and extracting profile change information from LiDAR data. The available software provide useful tools for beach profile data management and analysis. However, they failed to take advantage of dense datasets collected by LiDAR systems to analyze data spatially. First, the elevation measurements along beach profiles can only be imported from existing text files and be displayed on the background map, but cannot be directly extracted from LiDAR DEM. Second, the important features such as dune crest and toe, and berm crest are identified based on visual interpretation, which restricts a quantitative change analysis of profiles for a large geographic area. Third, although the beach profiles could be displayed spatially on the background map, it is still difficult to visualize and analyze the spatial variations of changes between different profiles along the shoreline. Fourth, the beach profile information is not fully integrated with geographic information system and cannot be edited and visualized interactively.

To address the above research gaps, this research presents automated algorithms for cross-shore profile feature extraction and change analysis. Important features of the beach profile are identified automatically based on the calculation of slope and curvature values. The attributes such as slopes for dune face and beach, as well as the heights and horizontal positions for dune crest and berm crest are derived to characterize the morphologic properties of each beach profile. The quantitative identification and attributes derivation of profile features enables more efficient coastal morphology analysis for a large geographic area. The spatial patterns of the beach profile features and the related changes can be visualized and analyzed along the shoreline. The object representation of profile features could also facilitate the analysis in conjunction with other GIS data for exploring the causes and impacts of the morphological and volumetric changes at the cross-shore dimension.

2.3 Pixel-based morphological change analysis

Traditionally, the pixel-based differencing method was commonly used for the morphological and volumetric change analysis based on LiDAR surveys (Meredith et al., 1999; Woolard and Colby 2002; White and Wang 2003; Zhang et al. 2005; Gares et al. 2006). The volumetric change is evaluated by subtracting the LiDAR DEM acquired at an earlier time from the LiDAR DEM acquired at a later time. A negative elevation difference of a cell indicates that the surface material was eroded during the time span between two LiDAR surveys. A positive elevation difference indicates that the sediment accretion occurred, and a zero value indicates that there was no net change.

For the traditional pixel-based approach, the spatial pattern of morphological changes can be visually interpreted. However, it cannot explicitly represent individual elevation change patches and extract information for each patch. For early coastal change studies based on LiDAR data, the morphological change information was usually only derived for the entire study area. In recent years, some efforts have been made to localize the change information. Woolard and Colby (2002) evaluated dune volume changes for two small study sites (100 x 200 m) located in Cape Hatteras National Seashore, North Carolina for a 1-year period of time using sequential LiDAR DEM. The volumetric change measurements were compared at spatial resolutions ranging from 1 x 1 to 20 x 20 m to decide which resolution provides the most reliable representation of coastal dunes and the most accurate change measurements. In their study, only the total volume of erosion, deposition, and net change results were calculated and compared.

Meredith et al. (1999) assessed hurricane-induced beach erosion between fall 1997 and fall 1998 along the entire North Carolina coastline (approximately over 500 km long). Their research use LiDAR technology for regional-scale volumetric change analysis. The beach sections were arbitrarily divided by inlets. For 21 beach sections, the volume of sediment gain or loss by unit length of each beach section was determined, and the spatial patterns of erosion were analyzed. Several parameters were calculated for each beach section to describe a regional pattern of volumetric change including the average sand gain or loss per unit length, the total volume of erosion, deposition, and net change, as well as the average volume change over each beach area.

White and Wang (2003) used LiDAR DEM to study an approximately 70-km stretch of the southern North Carolina coastline and investigated the spatial patterns of morphologic change occurred to five barrier islands between 1997 - 2000. First, the spatial pattern of morphologic changes was analyzed by a visual comparison of DEMs for different years. Then, the total volumetric change was quantified by using pixel-by-pixel differencing method. To facilitate the spatial analysis of erosion and deposition, areas of interests (AOIs) were created for each island. Each AOI "designates a particular segment of coastline and consists of the primary portion of the dune line and dry beach". The total volumetric change of the beach and sand dunes within each AOI was summarized from the cell-by-cell differencing results. Statistics of net volumetric change per unit area of all AOIs on each island were calculated. The means of net volumetric change per unit area of AOIs were calculated for three categories of management practices (developed, undeveloped, and nourished) to facilitate the comparison of morphological changes that occur naturally or human-induced.

Zhang et al. (2005) compared 40km of beaches along the central Florida Atlantic coast surveyed before and after Hurricane Floyd in 1999. The whole study area was split into 35 separate tiles, each 1km long in the north-south direction. Net beach volume change for each tile was calculated using the pixel-based differencing method. The along-shore spatial pattern of net volume change and net volume changes per unit shoreline of all the tiles was analyzed. Within each tile, the volume changes occurred between adjacent transects with an interval of 10 m were calculated and depicted.

Gares et al. (2006) used LiDAR surveys to monitor a beach nourishment project at Wrightsville Beach, North Carolina, from 1997 to 2000. The study area was divided into beach and dune zones based on specific elevations. Each zone was further divided into several segments including non-nourished, transition, and nourished zones. The volumetric changes in the beach and dune zones were summarized for each individual area of interest. The spatial variations of volumetric change per shoreline length were analyzed by examining all the nourishment zones in both beach and dune zones.

Coastal elevation changes can be caused by many factors other than erosion and deposition, such as vegetation dynamics, human impacts, and data noise. The traditional pixel-based method has difficulty in recognizing changes caused by various mechanisms. As pointed out by Woolard and Colby (2002), the laser pulses returned from the vegetations or man-made structures could result in artifact changes. To avoid the complexity in evaluating the dune volume changes, they selected the Cape Hatteras National Seashore as the experiment sites for their research. In this area, the vegetation may have introduced spurious changes, but the issue of man-made structure were not of concern because the development in that area is sparse and tightly controlled. A further example comes from the research by White and Wang (2003), in which areas of interests (AOIs) were initially used to localize the information about erosion and deposition, the authors pointed out that another important purpose of using AOIs is to exclude the heavily vegetated areas and man-made structures such as houses and piers, which may introduce significant error into the analysis.

In summary, for traditional pixel-based differencing method, the spatial pattern of volumetric changes can be visually interpreted for a qualitative analysis. However, the pixel-based differencing method suffers from several problems. First, most previous studies only calculate and report overall erosion, deposition and net volume change for the entire study area, but since the individual erosion and deposition patches were not explicitly represented, the localized information about distinct erosion and deposition regions cannot be derived. Second, the elevation changes could be introduced by many factors other than erosion and deposition. The cell-by-cell differencing is subject to data noise and data processing errors involving the accuracy of the horizontal and vertical data values. In vegetated and developed areas, laser pulses may be returned from the dense vegetation cover, or the top of man-made structures instead of the ground surface, which may introduce the spurious elevation changes. Using pixel-based differencing method, it is difficult to recognize and correct artifact changes caused by various factors. The splitting of the beach into sections or tiles in the previous research is often arbitrary, and each section or tile may contain beach erosion and deposition patches. The statistical summary for each section/tile may be misleading or difficult to interpret.

To address the above research gaps, this research presents an object-based method for morphological and volumetric change analysis. Individual erosion and deposition patches are automatically identified and delineated as discrete objects, which are used as basic spatial units for morphologic and volumetric analysis. A set of two-dimensional and three-dimensional attributes are derived to characterize and quantify erosion and deposition objects, which provide comprehensive quantitative information

for various aspects of coastal morphology. The localized attributes about individual patches provides a higher level of information about volumetric change, which could facilitate the analysis of various properties of each patch and the spatial pattern of these patches. In addition, the quantitative analysis of attributes could support the discrimination and classification of individual change objects into different classes to achieve a better understanding of the nature and characteristics of morphological changes for each class. The derived information could be used for a more detailed assessment of the impacts of hazardous coastal events such as storms and hurricanes and the effects of human interventions such as the beach nourishments and constructions of costal defense structures.

3 LiDAR DATA PREPROCESSING

This section introduces the airborne LiDAR survey technology and the basic LiDAR data products. Commonly used operations and algorithms for preprocessing LiDAR data are discussed.

3.1 Airborne LiDAR remote sensing system

The airborne LiDAR, an acronym for Light Detection and Ranging, is an integrated system consisting of laser scanner, differential Global Positioning System (GPS), and Inertial Measurement Unit (IMU). The laser scanner sends thousands of laser beams per second to the ground and measures the time it takes each laser beam to reflect back to the sensor receiver. The onboard differential GPS and IMU are used to determine the precise position and attitude of the laser scanner. Using the aircraft position and orientation information from GPS and IMU, the laser range measurements can be converted to highly accurate elevation values.

In coastal areas, the high-resolution topographic data provided by LiDAR is important for human/ property safety and coastal habitat management. LiDAR data has been used for coastal applications such as floodplain mapping, storm surge and tsunami modeling, sea level rise scenarios analysis, shoreline mapping and change analysis, coastal planning and development, and emergency response (NOAA, 2008b). Since 1996, to address the needs in coastal communities, NOAA Coastal Service Center has been collecting and delivering coastal LiDAR data through working with state and local programs. LiDAR data along the U.S. coast are archived and available online at NOAA

Coastal Service Center (http://maps.csc.noaa.gov/TCM/). The coastal LiDAR surveys usually occurred during the fall because the beach is generally at its widest after sand accumulation over the summer months. Survey flights are often scheduled within a few hours of low tide so that the maximum extent of the beach is exposed.

For coastal topographic mapping, most LiDAR systems use near-infrared laser light in the region from 1045 to 1065 nm (NOAA, 2008b). The flight altitude is usually in the range of 300-2000 m. The range of spatial resolution is usually between 0.75 m and 2 m. The horizontal position accuracy of measurement point data is less than 1 m and vertical accuracy is approximately 15 cm.

3.2 Basic LiDAR products

LiDAR technology is based on the accurate laser range measurement R between the LiDAR sensor and the object, which is determined by:

$$R = \frac{1}{2} tc \tag{3.1}$$

where t is the traveling time of a pulse of laser light from the transmitter to the target and back to the receiver, and c is the speed of light.

By combining the information from the GPS-derived antenna position (latitude, longitude, and ellipsoidal height), IMU-derived antenna orientation (roll, pitch, and heading), and the range measurement, LiDAR post-processing system could produce an array of points defined by its latitude, longitude, and altitude (x, y, z) coordinates, which is known as mass points. Since each laser pulse transmitted from the aircraft could generate multiple returns when encountering materials with local relief, the mass points

are associated with multiple returns files such as first return, possible intermediate returns, and last return file. The first return comes from the materials with local relief, such as the canopy top, building roof, and other unobstructed surfaces. The last return comes from the laser pulse that reaches the ground and is backscattered toward the receiver.

The initial LiDAR mass points are irregularly spaced and can be interpolated to create a regular grid of elevation values. The values for each given cell in the elevation grid can be determined by using an Inverse Distance (IDW) method, by averaging all of the point elevation values in that cell, or by taking the minimum/ maximum value of all the point elevation values in that cell. The elevation grid can also be created using a Triangular Irregular Network (TIN) which is generated from mass points.

The mass points associated with first return could be interpolated into a Digital Surface Model (DSM), which contains elevation information about all features in the landscape, such as vegetation and man-made structures. A bare-Earth Digital Terrain Model (DTM), which contains elevation information about the bare-Earth surface, could be created by extracting and removing mass points that come from features extending above the bare ground. A semiautomatic filtering algorithm can be first applied to identify the mass points that are vegetation and man-made structures. Visual interpretation and manual editing are then performed to create the final bare-Earth elevation model.

3.3 LiDAR data preprocessing

To conduct coastal morphological change analysis, a number of pre-processing operations are needed for the repeat LiDAR surveys separated in time. LiDAR datasets acquired at different time should first be referenced to a common datum and projection, and then be horizontally co-registrated and vertically calibrated.

The measurements of both the horizontal coordinates and the elevation of laser points are subject to errors due to the uncertainties in determination of aircraft trajectory, orientation, and laser ranging. The total error of LiDAR measurement could be decomposed into two components: random error and mean error (Sallenger et al., 2003). The mean error refers to the systematic bias, which is indicated by the mean difference between two datasets. The random error is indicated by the variation about the mean of differences between datasets. The mean error, which is often attributed to drift in the differential GPS, is the major error source and vary between different flight missions.

The reliability and accuracy of volumetric change analysis depends on the relative accuracy between two successive LiDAR surveys used for the comparison. By conducting horizontal co-registration and vertical calibration, we could remove the systematic mean errors and enhance the accuracy of morphological and volumetric change analysis. The horizontal misalignment of two LiDAR datasets could generate misleading changes, especially in the areas with high surface slope or man-made structures. If the horizontal alignment error σ_h is significantly larger than the LiDAR DEM cell size, a horizontal co-registration of two LiDAR datasets will be necessary to avoid the possible artifact changes induced by the misalignment. The vertical error in

each LiDAR dataset could also directly generate errors in resulting elevation changes. Given a nominal vertical accuracy σ_v of LiDAR elevation measurements, the error of the elevation differences can be as large as $\sqrt{2}\ \sigma_v$. It is necessary to perform vertical calibration to avoid the possible artifact changes in volumetric analysis.

The horizontal registration and vertical calibration can be conducted by using pseudo invariant features as tie points. Pseudo invariant features are stable natural or man-made objects whose planimetric position and elevation are known and can be assumed unchanged over the time between LiDAR surveys at different time. The good candidates for pseudo invariant features could be large buildings with a flat roof, parking lots, paved roads, airport runways, etc. Horizontal co-registration requires point features like the corners of building and the intersections of roads. Vertical calibration requires linear features such as paved roads and polygon features such as parking lots if no tilt is present. The pseudo invariant features can be identified from hill-shaded images and LiDAR intensity images.

For horizontal co-registration, a similarity (conformal) transform in Equations (3.2) and (3.3) or an affine transform in Equations (3.4) and (3.5) can be fitted to correct the horizontal misalignment. The similarity (conformal) transform accounts for the translational, rotation and scale differences. The affine transform accounts for additional skew shape (aspect ratio) changes. In most cases, similarity transform is adequate to meet the requirements of horizontal co-registration.

Similarity transforms:

$$x = ax' + by' + c \tag{3.2}$$

$$y = -bx' + ay' + f \tag{3.3}$$

Affine transforms:

$$x = ax' + by' + c \tag{3.4}$$

$$y = dx' + ey' + f \tag{3.5}$$

where (x, y) are the planimetric coordinates of the first LiDAR data set, (x',y') are planimetric coordinates of the second LiDAR data set, and a, b, c, d, e, and f are coefficients to be fitted from pseudo invariant features using the least-squares method.

For vertical calibration, a linear plane surface in Equation (3.6) can be fitted to correct the vertical errors.

$$\delta z = Ax + By + C \tag{3.6}$$

where δz is the correction value of the second LiDAR data set relative to the first LiDAR data set, (x,y) are the planimetric coordinates after horizontal co-registration, and A, B, C are the coefficients to be fitted through pseudo invariant features. The coefficients A and B represent the gradients of the tilt plane along the x and y directions, which are equal to zero if no tilt is detected between two LiDAR surfaces. The coefficient C represents the systematic offset between two LiDAR surfaces.

Horizontal co-registration should be performed before vertical calibration. After vertical calibration, the accuracy of volumetric change analysis would be only influenced by the random errors of the LiDAR measurements, which is indicated by the standard deviation about the mean of differences between datasets. The level of random errors can be reduced by applying low-pass filter such as median filter or Gaussian filter. The median filter and Gaussian filter are edge-preserving. They can remove data noise

without distorting the object boundaries, which represents an advantage over linear filters. The random error after filtering can be estimated by calculating the standard deviation of elevation change along a pseudo invariant feature such as a paved road. The resulting error will be used to establish the range of possible variation about the mean volumetric changes, and to determine the thresholds for assuming that elevation change has occurred between successive LiDAR surveys.

4 MORPHOLOGIC ATTRIBUTES EXTRACTION AND CHANGE ANALYSIS BASED ON BEACH PROFILES

In this section, the concepts and definitions of beach morphological features are reviewed, and basic mathematical principles for extracting these morphological features from a hypothetical beach profile are discussed. Numerical algorithms are designed and refined to handle complex real world beach profiles. A scale-space approach is introduced to identify critical morphological feature points on each beach profile, and the profile is subsequently divided into a number of sections. A set of morphological attributes are derived for characterizing the beach profile and the corresponding changes. Numerical algorithms are implemented as an ArcGIS extension module-Profile Analyst, to perform the morphological profile feature extraction and change analysis from the LiDAR-derived beach profiles.

4.1 Mathematical principles for extracting morphological features from beach profiles

4.1.1 Typical beach profile and definition of morphological features

Beach profile analysis represents one-dimensional approach to the studies of coastal geomorphology, which is widely used by geomorphologists. A beach profile shows elevation variations along a cross-section which is usually perpendicular to the shoreline. A profile often extends from the backshore cliff or dune to the shoreline. It may also extend seaward across the foreshore into the inner continental shelf of the nearshore zone where waves and currents do not transport sediment to and from the beach (Figure

4.1). Beach profiles extracted from airborne LiDAR data often cover part of upland and the entire backshore up to the shoreline, and the foreshore under water surface is not included due to lack of the water penetration capability of topographical LiDAR systems. The shape of the beach profile determines the vulnerability of the coast to storms, the extent of usable beach for habitat and creation, and the legal boundary distinguishing public and private ownership of land. Profiles taken at different dates can be compared to illustrate and quantify storm, seasonal, and longer-term changes in beach width, height, volume, and shape.

The Atlantic and Gulf coasts of North America are characterized by gently sloping seashores as the result of gradual submergence of the continent's edges. Coastal dunes and sandy beaches are common and extensive along most of the coastline. In contrast, much of the west coast of North America is characterized by the precipitous cliffs, steep-walled bluffs, and rocky headlands. Coastal bluffs and sea cliffs are the seaward edges of marine terraces, shaped by ocean waves and currents, and uplifted from the ocean floor. Rocky headlands are composed of igneous rocks that are resistant to wave erosion. Coastal bluffs are composed mainly of sedimentary rocks that are particularly prone to erosion. To design numerical algorithms for coastal feature extraction, we need to define and characterize morphological features associated with two different types of profiles: sandy beach profile and bluff profile. The former prevails in the Atlantic and Gulf coasts of North America, and the latter in the west Pacific coast of North America. A typical beach profile is adapted from the Coastal Engineering Manual by US Army Corps of Engineers (Morang and Parson, 2002) (Figure 4.1) to

illustrate and define beach morphological features (Morang and Parson, 2002; Schwartz, 2005).

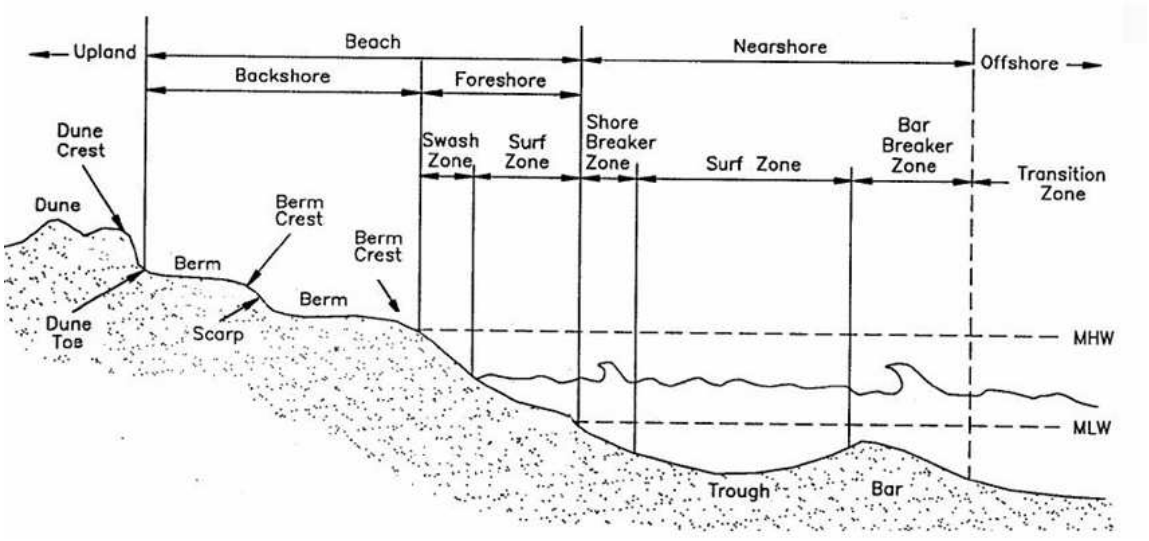

(a)

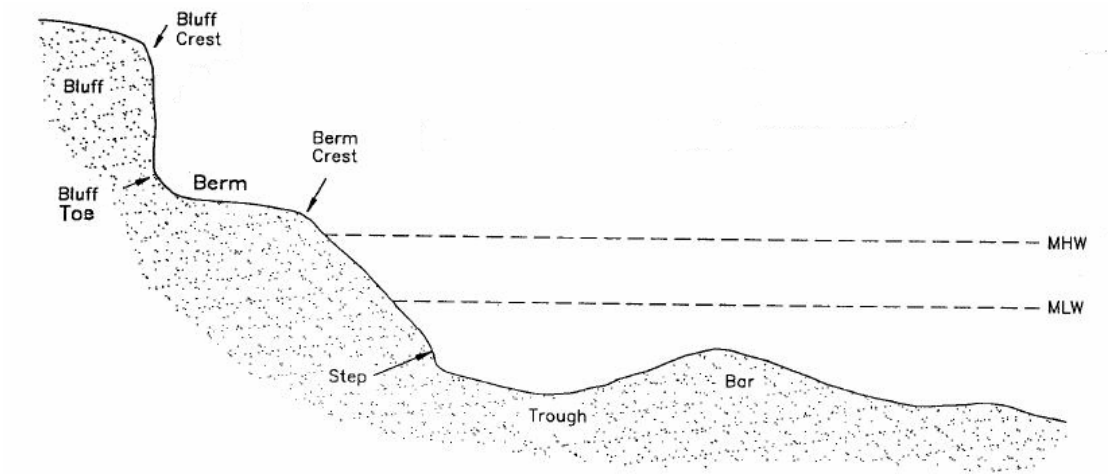

(b)

Figure 4.1 Illustration of morphological features of the coastal zone. (a) A typical beach profile; (b) A typical bluff profile (Adapted from Coastal Engineering Manual by US Army Corps of Engineers)

The backshore runs from the seaward-most dune to the land and water intersection. The backshore is the more landward and higher part of the beach and is typically a near-horizontal to gently landward-sloping surface. The backshore is not affected by the run-up of waves except during storm events and so it is the typical dry part of the beach. The landward limit of the active beach (beach head) includes dunes, cliffs/ bluffs, or engineered structures such. Dunes are windblown sand mounds on the backshore, usually in the form of small hills or ridges, stabilized by vegetation or control structures. The dune crest is the ridge line, and the dune toe is the point of break in slope between a dune and a backshore. Beach berms are broad, near-horizontal areas and are depositional features created from the wave-induced onshore accumulation of sediment, typically during summer. One or more berms may appear on a beach, depending on seasonal changes in water level. Beach scarps are nearly vertical slopes produced by wave erosion, which occur when the slope of the beachface is lowered during storm events. The height of a beach scarp may be just a few centimeters or a meter, depending on the degree of wave action and the type of beach material. Beach scarps may disappear by the return of sand onshore during berm accretion. The seaward margin of the berm is typically defined by a rather abrupt change in slope from the near horizontal surface of the berm to the inclined surface of the beachface. The line defined by this change in slope is called the berm crest or berm edge. The beach intersects the water at the foreshore, and the foreshore (beachface) is the more seaward part of the beach and typically a plane slope that extends over a water level range from low tide to high tide.

Figure 4.1b shows a typical bluff profile, in which bluff crest, bluff toe, berm, berm crest, and step are illustrated. A coastal bluff is an escarpment or high, steep face of rock, decomposed rock, or soil rising above the shore, caused by wave undercutting of the cliff toe. A bluff crest is the upper edge or margin of a bluff. Bluff toe is the base of a bluff where it meets the beach. A bluff face is the sloping portion of a high bank between bluff crest and toe. A seacliff beach berm is a flat and narrow stretch of sand between the bluff (cliff) and the ocean, and beach berm crest is the seaward limit of the flat berm with a rather abrupt change in slope to the inclined beachface.

4.1.2 Morphological feature extraction from an ideal beach profile

For each location on a beach profile, several indicators could be derived to quantify the morphological characteristics of major beach features at that location:

1) $z = f(x)\,\big|_{x=x_0}$ defines the elevation of the profile at location x_0

2) $z' = \dfrac{df(x)}{dx}\,\big|_{x=x_0}$ is the first derivative of the profile at location x_0, which defines the slope at this location. When $z' > 0$, the elevation is increasing ($\uparrow$); while when $z' < 0$, the elevation is decreasing ($\downarrow$).

3) $z'' = \dfrac{df^2(x)}{dx^2}\,\big|_{x=x_0}$ is the second derivative of the profile at location x_0, which defines the rate of slope change at this location. When $z'' > 0$, the profile is concave up ($\cup$); while when $z'' < 0$, the profile is concave down (convex) ($\cap$).

4) $|\kappa| = \dfrac{|z''|}{(1+z'^2)^{3/2}}\,\big|_{x=x_0}$ is the curvature of the profile at location x_0. The smaller the curvature, the flatter the curve is at this point. The larger the curvature, the sharper turn the curve has at this point.

The extraction of critical feature points such as dune crest, dune toe, and berm crest can be based on the combination of second derivative and curvature, which could also be represented as signed curvature:

$$\kappa = \frac{z''}{(1+z'^2)^{3/2}} \Big|_{x=x_0} \tag{4.1}$$

The sign of κ indicates the direction of slope change, and the absolute value of κ indicates the sharpness of the curve.

The concepts and algorithms for feature extraction are illustrated using a simplified beach profile shown in Figure 4.2. Based on discrete distance measurements whose resolution is determined by cell size Δx, the elevation of the beach profile is defined as:

$$z = f(x) \qquad x = 0, \Delta x, 2\Delta x, \ldots \tag{4.2}$$

where x is the horizontal distance from current location to the shoreline, and z is the elevation measurement at current location. For each point on this simplified beach profile, first derivative (slope) is calculated based on central difference using one point on each side of the current point:

$$f'(x) = \frac{f(x+\Delta x) - f(x-\Delta x)}{2(\Delta x)} \tag{4.3}$$

The second derivative is also calculated based on central difference, using slope value of one point on each side of the current point:

$$f''(x) = \frac{f'(x+\Delta x) - f'(x-\Delta x)}{2(\Delta x)} \tag{4.4}$$

For each point, the signed curvature is calculated as:

$$\kappa = \frac{f''(x)}{(1+f'(x)^2)^{3/2}} \tag{4.5}$$

By applying Equation (4.3) and (4.5), slope and signed curvature value are calculated for the simplified hypothetic beach profile. The results are shown in Figure 4.3.

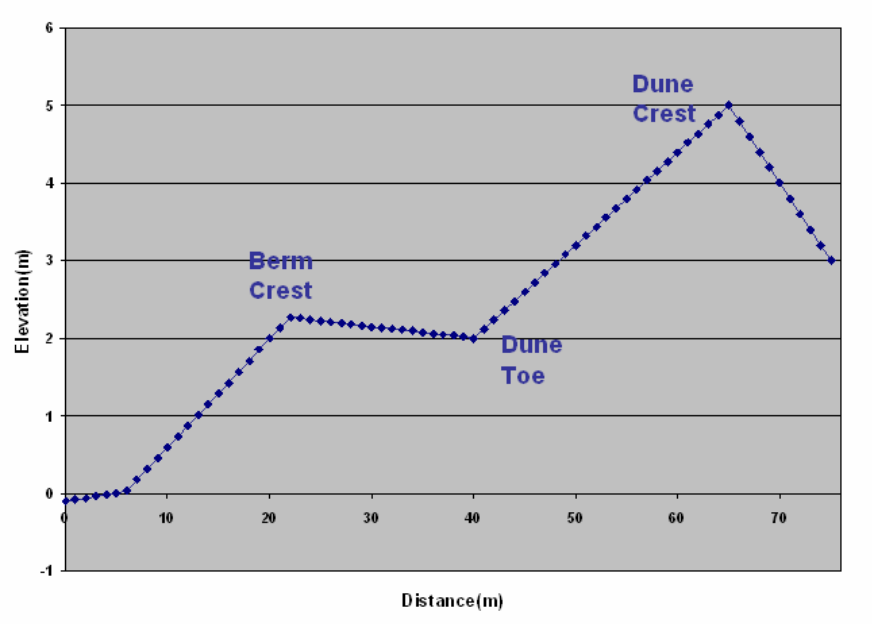

Figure 4.2 A simplified hypothetic beach profile

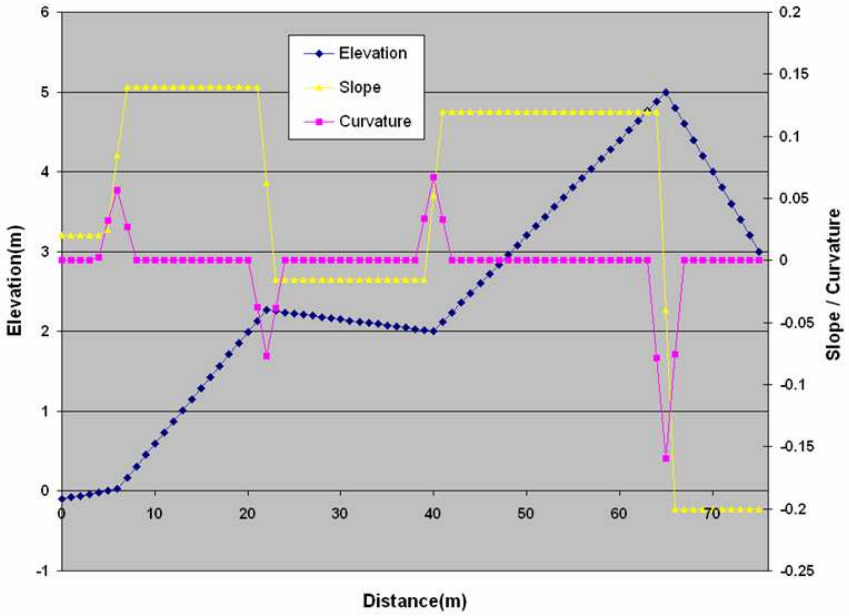

Figure 4.3 Slope and curvature derived for a simplified hypothetic beach profile

The geometric characteristics of morphological features on the beach profile are summarized as follows:

1) Dune/bluff crest: High elevation value, abrupt slope change, and negative signed curvature with high absolute value;

2) Dune/bluff toe: A sudden slope increase from the beach berm to the dune/bluff face, and positive signed curvature with relatively high value;

3) Beach berm: Low surface slope value;

4) Beach scarp: High positive slope value;

5) Berm crest: Relatively low elevation and a sharp break in slope from near-vertical surface of scarp or the inclined surface of beachface to the near horizontal surface of berm.

To constrain the search space for morphological features, a vertical threshold is given to roughly divide the beach zone and dune zone. When searching in the direction from the shoreline to the dune, the berm crest corresponds to the point with the minimum signed curvature value in the beach zone, and the dune/bluff crest corresponds to the point with the minimum signed curvature value in the dune zone. Once the locations of dune crest and berm crest are determined, the dune/bluff toe can be identified by searching for the point with maximum signed curvature between the dune/bluff crest and the berm crest, which indicates a dramatic slope change and a substantially concave profile shape.

4.2 Morphological feature extraction from natural beach profiles

The real-world natural beach profiles are far more complex than the simplified hypothetic profile illustrated above in Section 4.1. If the same algorithm is applied to natural beach profile (Figure 4.4), many peak and trough points may be identified in terms of the first derivative (slope) and signed curvature criteria, which will be confused with the actual dune/bluff crest, dune/bluff toe, and berm crest. This is because the natural beach profiles are noisy and contain the small-scale local variations (Figure 4.5). The challenge is how to make algorithms robust to data noise and to be able to differentiate dune/bluff crest, dune/bluff toe and beach berm crest from micro-level topographic variations. This research develops a scale-space approach to the analysis of beach profile at various scales, and the contextual information is also utilized to achieve a robust detection of morphological features.

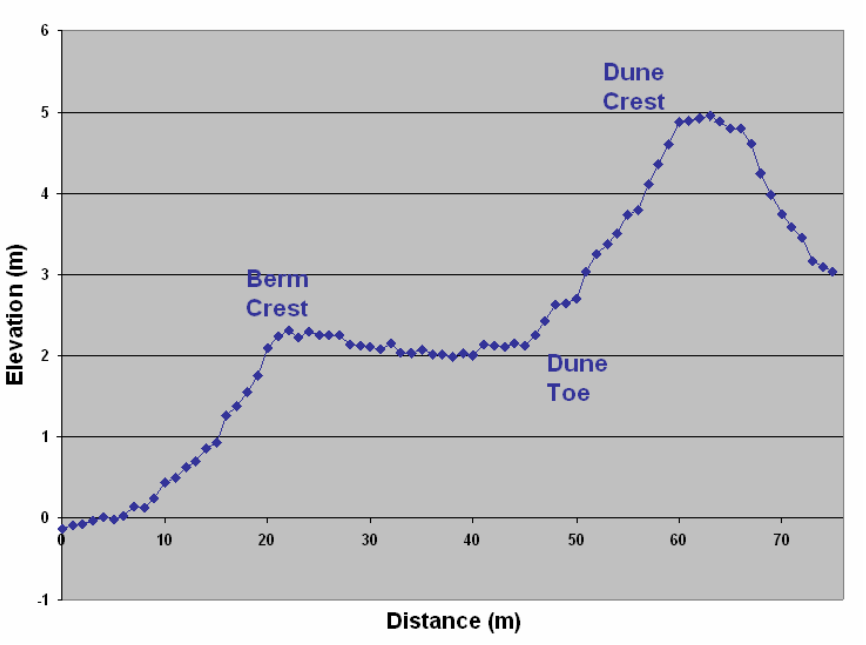

Figure 4.4 A natural beach profile

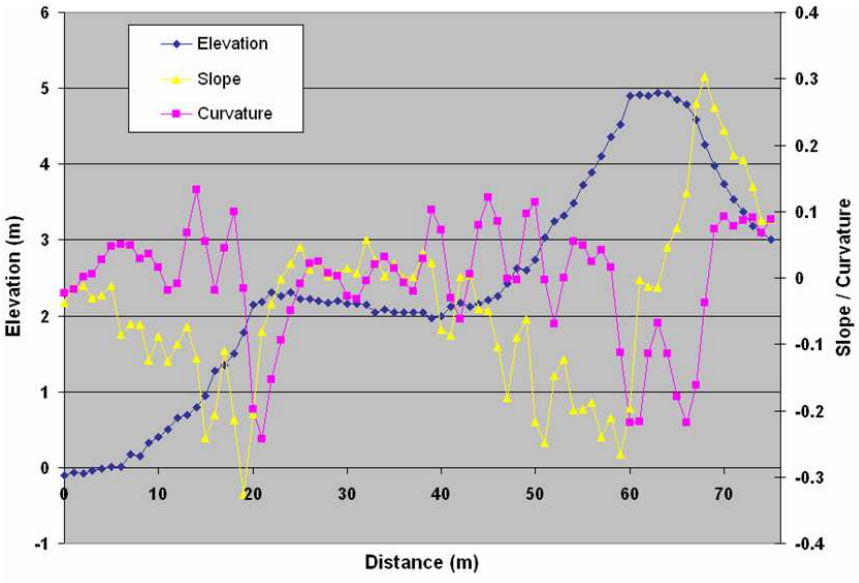

Figure 4.5 Slope and curvature derived for a natural beach profile

4.2.1 Scale-space approach to feature extraction from beach profiles

A successful extraction of the important morphological features from the natural beach profiles depends upon the selection of appropriate scale of analysis. The need for a multi-scale signal analysis method arises when we need to automatically derive information from real world measurement (Lindeberg, 1994). The scale-space approach (Witkin, 1983) is one of the most well-developed and commonly used methods of multi-scale analysis, which can be used to represent a curve as a family of curves smoothed at various detail levels. The essential requirement for multi-scale analysis is that new structures, which do not correspond to the simplifications of corresponding structures at finer scale, should not be created at a coarser scale. A set of standard scale-space axioms has been used to derive the appropriate low-pass kernel type. The uniqueness of Gaussian kernel result in its suitability for the scale-space approach, which includes linearity, shift invariance, the semi-group structure, scale invariance, rotational invariance, non-creation of local extrema, and non-enhancement of local extrema.

A Gaussian kernel follows the Gaussian distribution. For continuous variable *x*, the standard Gaussian distribution $G(x)$ with mean $\mu = 0$ and standard deviation σ is given by:

$$G(x,\sigma) = \frac{1}{\sqrt{2\pi}\sigma}\exp(-\frac{x^2}{2\sigma^2}) \tag{4.6}$$

Gaussian distributions centered at mean of zero with different standard deviations are graphed in Figure 4.6. As shown, the larger the standard deviation value σ, the more spread out the kernel distribution is.

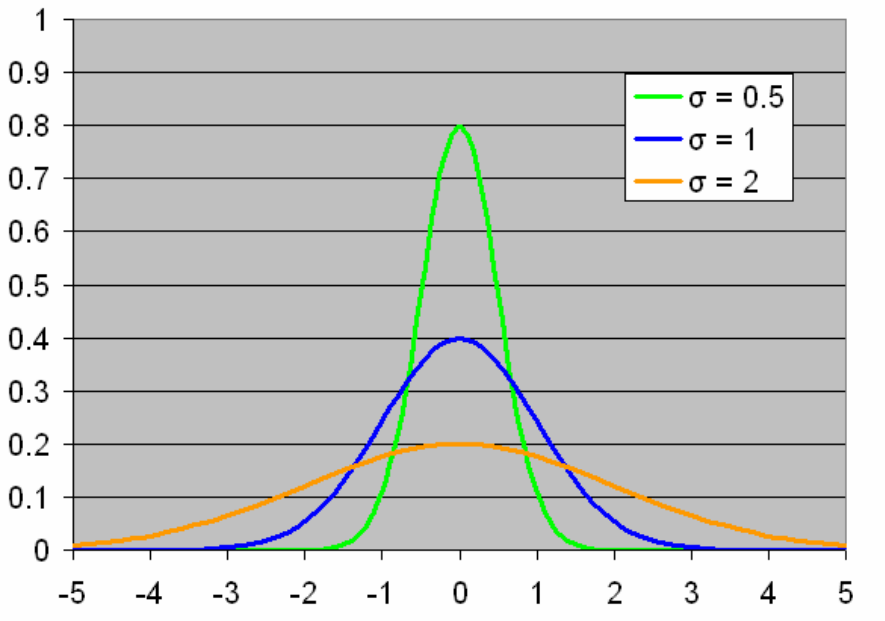

Figure 4.6 Gaussian distributions with different standard deviations

For a given curve *u(x)*, its Gaussian scale-space representation is a family of curves defined by its convolution with the Gaussian kernel with varying standard deviation values:

$$U(x,\sigma) = u(x) * G(x,\sigma) \tag{4.7}$$

The standard deviation σ controls the smoothing degree of the filter. The larger the standard deviation, the larger the scale of analysis and the less details (local variations) will remain in the curve.

The critical features of the elevation curve correspond to the points of dramatic slope changes, which are associated with the extreme points on the curvature curve. By selecting different standard deviation values for Gaussian filter, the elevation curve can be smoothed at different scales, so that the critical features can be extracted at different scale from the resulting curvature curve.

When dealing with elevation curve based on discrete distance measurements, the Gaussian distribution $G(n,\sigma)$ needs to be discretized:

$$G(n,\sigma)=\frac{1}{\sqrt{2\pi}\sigma}\exp(-\frac{(n\Delta x)^2}{2\sigma^2}) \qquad n=\ldots,-2,-1,0,1,2,\ldots \tag{4.8}$$

where σ is standard deviation and Δx is the cell size. Since the Gaussian function decays rapidly, 95.45% of the area in the Gaussian function is contained in the window $[-2\sigma_0, 2\sigma_0]$, given an analysis scale σ_0. Therefore, to construct a discrete Gaussian filter, the filter window could be truncated and be implemented as $[-b, b]$, where b is the minimum integer that satisfies $b\Delta x \geq 2\sigma_0$. For each pixel $n \in [-b, b]$ in the filter window, its value for the Gaussian filter could be calculated as:

$$G(n,\sigma_0)=\frac{1}{\sqrt{2\pi}\sigma_0}\exp(-\frac{(n\Delta x)^2}{2{\sigma_0}^2}) \qquad n=-b,-b+1,\ldots,-1,0,1,\ldots,b-1,b \tag{4.9}$$

Given the elevation curve $z=f(n)$, the smoothed curve of $f(n)$ at specific scale σ_0 is defined by its convolution with the Gaussian kernel:

$$F(n,\sigma_0)=f(n)*G(n,\sigma_0)=\sum_{m=-b}^{b} f(m)*G(n-m,\sigma_0) \tag{4.10}$$

$$n=-b,-b+1,\ldots,-1,0,1,\ldots,b-1,b$$

After smoothing elevation curve $z=f(n)$ at scale σ_0, the first derivative, second derivative, and curvature could be calculated for the smoothed elevation curve $F(n,\sigma_0)$. The critical features of the elevation curve could be identified as extreme points on curvature curve at various analysis scales.

For example, when a Gaussian filter with standard deviation σ=1 is applied to smooth the elevation curve shown in Figure 4.4, the resulting slope and curvature curves (Figure 4.7) are much smoother than the results from the original elevation dataset (Figure 4.5). On the curvature curve, the points corresponding to the critical features could be recognized as the extreme points, although there are some local extreme points in the neighborhood with very high curvature value, which may still cause confusion in the feature extraction process.

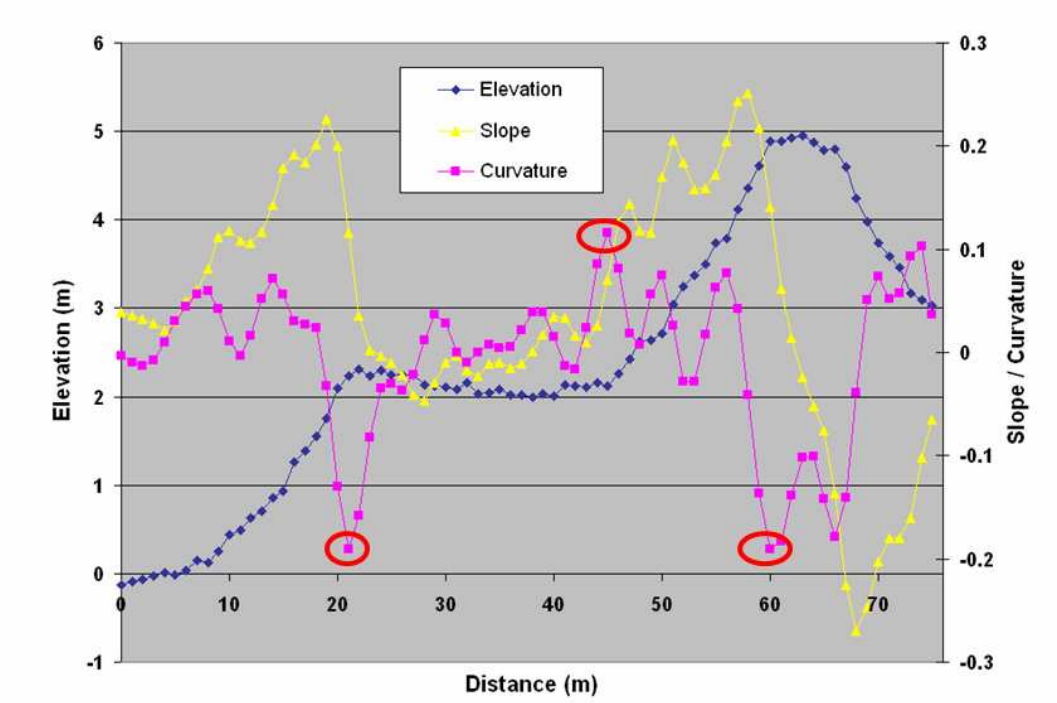

Figure 4.7 Feature extraction of beach profile at smooth scale σ=1

When a Gaussian filter with standard deviation σ=2 is applied to smooth the elevation curve shown in Figure 4.4, the resulting slope and curvature curve are even more smooth (Figure 4.8). On the curvature curve, the points corresponding to the

important features could be easily distinguished as the extreme points, and there is almost no local extreme point in the neighborhood that could cause confusion when identifying the important features.

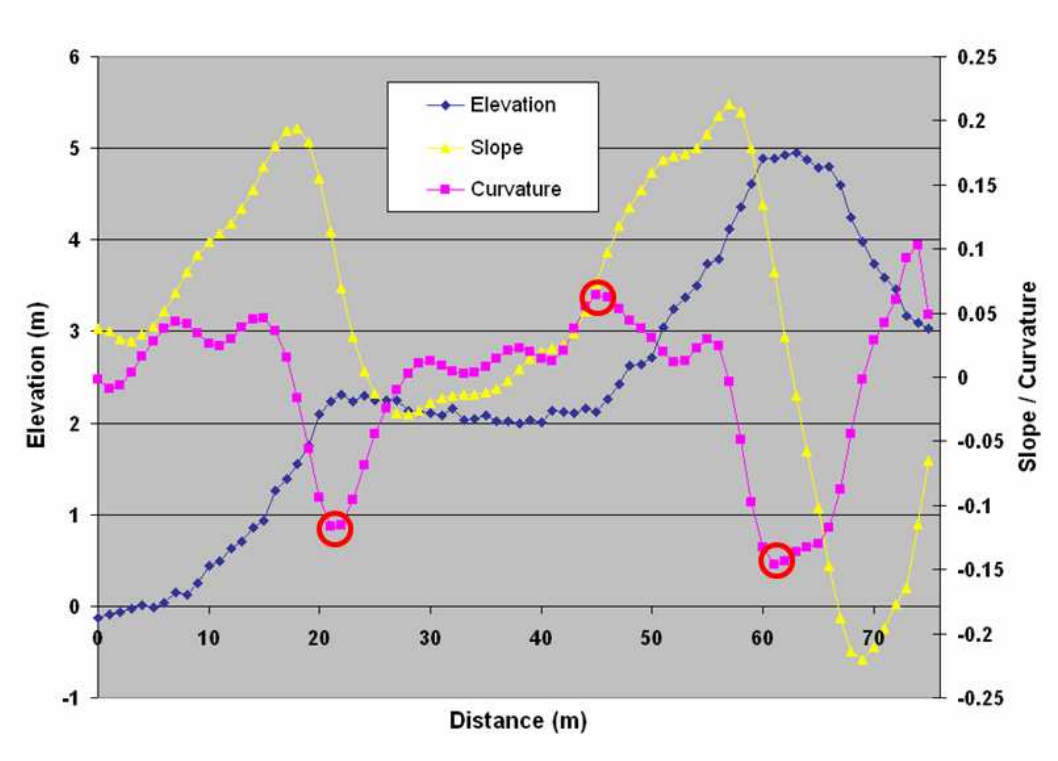

Figure 4.8 Feature extraction of beach profile at smooth scale σ=2

When a Gaussian filter with standard deviation σ=4 is applied to smooth the elevation curve shown in Figure 4.4, the slope and curvature curve are further smoothed (Figure 4.9). On the curvature curve, the points corresponding to the important features still can be recognized as the extreme points, but are not as distinctive as they were when σ=2. Besides, the extreme points shift from the locations that exactly correspond to the original slope change point of the elevation curve, which is caused by the larger analysis window.

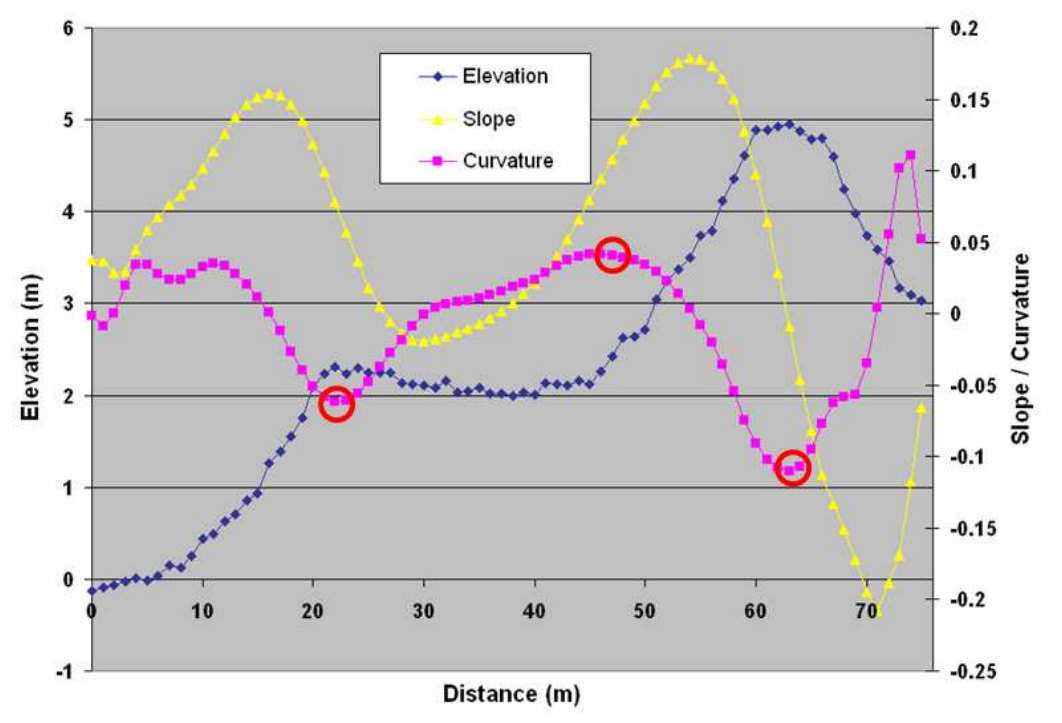

Figure 4.9 Feature extraction of beach profile at smoothing scale σ =4

Overall, analyzing the original beach profile at different detail levels will create different results for feature extraction. At a small scale of analysis, the local variations of elevation curve will result in the unwanted fluctuations in the slope and curvature curve, which may cause difficulty in distinguishing the critical feature points from many other local extreme points in the neighborhood. By increasing the scale of analysis, the curvature curve will become smoother, which will make the points that correspond to critical features more prominent. However, when the scale of analysis is further increased and becomes too large, the original elevation curve will be over smoothed, which may result in serious shift of the detected location of the critical features or even the failure in detecting certain features. The determination of appropriate scale of analysis is critical to achieve a desired result of beach profile feature extraction.

4.2.2 Incorporate contextual information for feature extraction of beach profile

The scale-space approach presented above works well in most cases, especially when the beach profiles have a relatively regular shape. However, in some cases the information about elevation, slope, and curvature of a single beach profile is not sufficient to determine the critical feature points satisfactorily, especially when some other points with a dramatic slope change exist. For example, for the profile shown in Figure 4.10, using a scale-space approach at smooth scale σ=2, the dune crest will be located on the back of the dune because of the presence of the lowest signed curvature value, which means a sharper slope change.

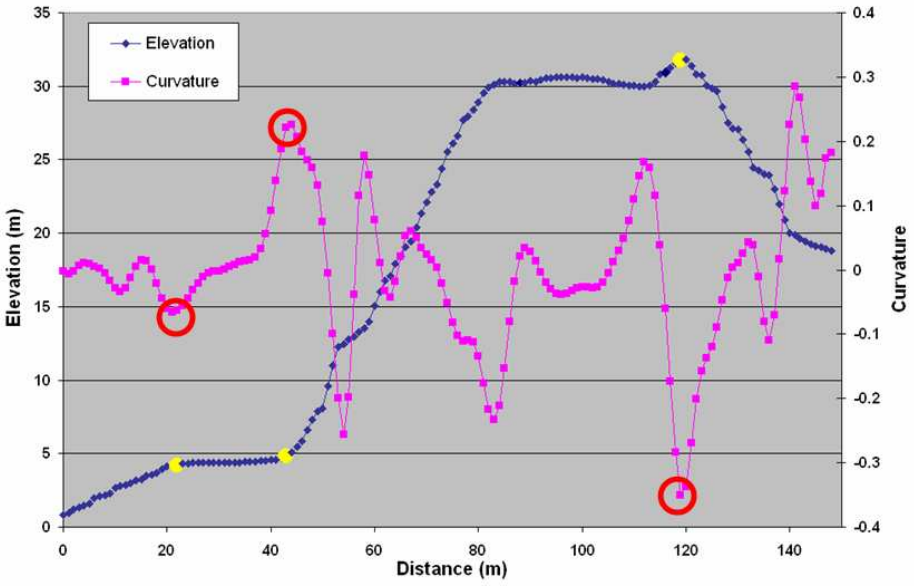

Figure 4.10 Mistakenly identified dune crest (smoothing scale σ=2)

To improve the accuracy and reliability in locating the feature points, the contextual information from the neighboring profiles could be incorporated based on the

assumption that the horizontal distance from origin point and the elevation of feature points are continuous or change gradually along a small segment of shoreline.

For the dune crest point identified based on curvature property for the profile shown in Figure 4.10. Its elevation and the horizontal distance from the shoreline are not consistent and compatible with its neighbors (Figure 4.11).

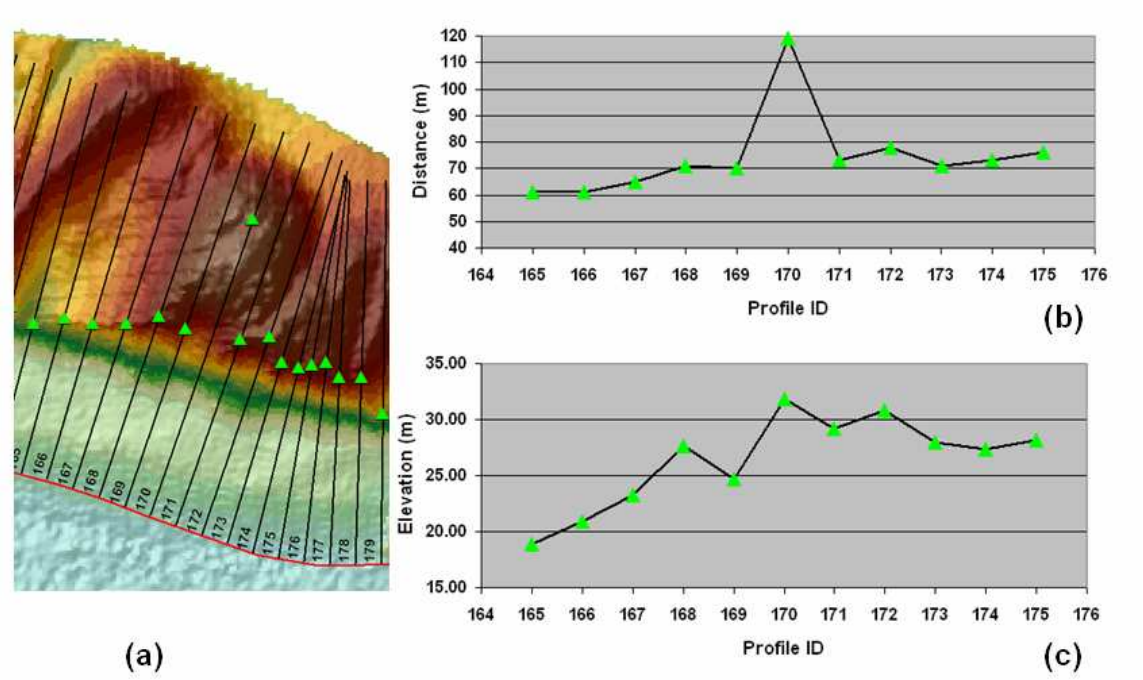

Figure 4.11 Example of dune crest identification based on information from individual beach profile. (a) Mistakenly identified dune crest (Profile ID = 170); (b) Inconsistency in horizontal distance from shoreline; (c) Inconsistency in elevation values

To incorporate the contextual information from the neighboring profiles, the compatibility and consistency analysis is performed for morphological points extracted for each beach profile in comparison with its neighboring profiles. If a dramatic difference exists between the location (horizontal and/or vertical) of its dune crest and the neighboring dune crests, the current location of the dune crest on profile is identified

as a potential error. Then several other locations which meet the elevation and curvature criteria are selected as candidate dune crest points on the beach profile. The compatibility of each candidate dune crest point with the dune crests on neighboring profiles is calculated based on both the horizontal distance to the origin point and the elevation. The dune crest point will be adjusted to the candidate location with most compatible horizontal distance and elevation value. Gaussian distribution is assumed for both the horizontal distances and elevation values of the dune crests of beach profiles within a given neighborhood of the shore segment. For each individual beach profile, the algorithms are as follows:

Step 1: Calculate the means and standard deviations of elevation and horizontal distance of the neighboring dune crest points in the given neighborhood:

$$\overline{z_{DC}} = \frac{1}{N}\sum_{i=1}^{N} z_{DC}^{i} \tag{4.11}$$

$$\overline{x_{DC}} = \frac{1}{N}\sum_{i=1}^{N} x_{DC}^{i} \tag{4.12}$$

where N is the total number of neighboring profiles in the given window size. $\overline{z_{DC}}$ is the average elevation of all the neighboring dune crests in this given window; z_{DC}^{i} is the elevation of the dune crest on profile *i*. Similarly, $\overline{x_{DC}}$ is the average horizontal distance from each neighboring dune crests to its corresponding origin point; x_{DC}^{i} is the horizontal distance from the dune crest on profile *i* to its origin point.

$$\sigma(z_{DC}) = \sqrt{\frac{1}{N-1}\sum_{i=1}^{N}(z_{DC}^{i} - \overline{z_{DC}})^2} = \sqrt{\frac{1}{N-1}[\sum_{i=1}^{N}(z_{DC}^{i})^2 - N(\overline{z_{DC}})^2]} \tag{4.13}$$

$$\sigma(x_{DC}) = \sqrt{\frac{1}{N-1}\sum_{i=1}^{N}(x_{DC}^{i} - \overline{x_{DC}})^2} = \sqrt{\frac{1}{N-1}[\sum_{i=1}^{N}(x_{DC}^{i})^2 - N(\overline{x_{DC}})^2]} \qquad (4.14)$$

where N is the total number of neighboring profiles in the given window size; $\sigma(z_{DC})$ is the standard deviation of elevation of all the neighboring dune crests in the given neighborhood; $\sigma(x_{DC})$ is the standard deviation of horizontal distance from all the neighboring dune crests to the corresponding origin point.

Step 2: Determine if the elevation and/or horizontal distance of the dune crest is compatible with its neighborhood. Use z_{DC} to denote the elevation of the dune crest on current profile, and x_{DC} to denote the horizontal distance from the dune crest to its origin point. The location of the dune crest will be identified as incompatible if the difference between the current location and the mean value of the neighborhood exceeds a certain threshold, i.e.:

$$| z_{DC} - \overline{z_{DC}} | \geq k\sigma(z_{DC}) \qquad \text{or}$$

$$| x_{DC} - \overline{x_{DC}} | \geq k\sigma(x_{DC}) \qquad (4.15)$$

where k is the multiplicative factor (usually ranging from 1.0 to 3.0). Once a dune crest location is identified as incompatible and thus may need to be adjusted, the following steps need to be executed.

Step 3: Determine the candidate locations for dune crest. The candidate location for dune crest could be selected based on combination of several criteria: (1) having an elevation above the minimum threshold; (2) having a signed curvature value lower than the maximum threshold; and (3) being the local minimum curvature point.

Step 4: Calculate the compatibility of each candidate dune crest with other dune crests on the neighboring profiles based on Gaussian distribution.

The probability density function of the standard Gaussian distribution with mean $\mu = 0$ and standard deviation $\sigma = 1$ is given by:

$$\varphi_{0,1}(x) = \frac{1}{\sqrt{2\pi}} \exp(-\frac{x^2}{2}) \tag{4.16}$$

The cumulative distribution function of a probability distribution is the probability of the event that a random variable *X* with that distribution is less than or equal to *x*. The cumulative distribution function of standard Gaussian distribution is given by:

$$P_{0,1}(X \le x) = \Phi_{0,1}(x) = \int_{-\infty}^{x} \frac{1}{\sqrt{2\pi}} \exp(-\frac{u^2}{2}) du \tag{4.17}$$

Thus the probability of the event that a random variable *X* with standard Gaussian distribution has an absolute value larger than $|x|$ is:

$$P_{0,1}(|X| > |x|) = 1 - P_{0,1}(-|x| < |X| < |x|) = 2\Phi_{0,1}(-|x|) \tag{4.18}$$

For a random variable *X* that follows Gaussian distribution with mean μ and standard deviation σ, the probability of the event that *X* has an absolute value larger than $|x|$ is:

$$P(|X| > |x|) = P_{0,1}(\left|\frac{X-\mu}{\sigma}\right| > \left|\frac{x-\mu}{\sigma}\right|) = 2\Phi_{0,1}(-\left|\frac{x-\mu}{\sigma}\right|) \tag{4.19}$$

When *x* equals to μ, the probability equals to 1. The larger the distance of *x* from mean value μ, the lower the probability of the event that *X* has an absolute value large than $|x|$, and the probability is approaching to 0 when *x* is moving further away from the mean value μ.

Assuming the elevation and horizontal distance measurements of dune crest follows Gaussian distribution, the normalized measurements follows a standard Gaussian distribution, which means:

$$P(|Z| > |z_{DC}|) = 2\Phi_{0,1}(-\left|\frac{z_{DC} - \overline{z_{DC}}}{\sigma(z_{DC})}\right|) \tag{4.20}$$

$$P(|X| > |x_{DC}|) = 2\Phi_{0,1}(-\left|\frac{x_{DC} - \overline{x_{DC}}}{\sigma(x_{DC})}\right|) \tag{4.21}$$

The compatibility of the dune crest on current beach profile with the dune crests in the neighborhood could be derived based on both the elevation and horizontal distance measurements:

$$Q_{DC} = P(|Z| > |z_{DC}|)P(|X| > |x_{DC}|) = 4\Phi_{0,1}(-\left|\frac{z_{DC} - \overline{z_{DC}}}{\sigma(z_{DC})}\right|)\ \Phi_{0,1}(-\left|\frac{x_{DC} - \overline{x_{DC}}}{\sigma(x_{DC})}\right|) \tag{4.22}$$

The commonly used algorithm to approximate the cumulative distribution function of standard Gaussian distribution is from Abramowitz and Stegun (1964). Given:

$$\varphi_{0,1}(x) = \frac{1}{\sqrt{2\pi}}\exp(-\frac{x^2}{2}) \tag{4.23}$$

The cumulative normal distribution is given by:

$$\Phi_{0,1}(x) = 1 - \varphi_{0,1}(x)(b_1 t + b_2 t^2 + b_3 t^3 + b_4 t^4 + b_5 t^5) + \varepsilon \tag{4.24}$$

where $t = 1/(1 + 0.2316419x)$, b_1=0.319381530, b_2=-0.356563782, b_3= 1.781477937, b_4 = -1.821255978, b_5 = 1.330274429. This approximation has a maximum absolute error of $7.5e^{-8}$.

Step 5: Adjust the dune crest point to the location that has the highest compatibility.

As shown in Figure 4.10, the compatibility function is calculated for the local minimum points which satisfy the requirement of elevation and curvature (in this case elevation > 10m and curvature < -0.1). The local minimum point with the highest compatibility value is identified as dune crest (Figure 4.12 and Table 4.1). The relocated dune crest is more consistent with its neighbors in terms of elevation and distance from origin point on the shoreline (Figure 4.13).

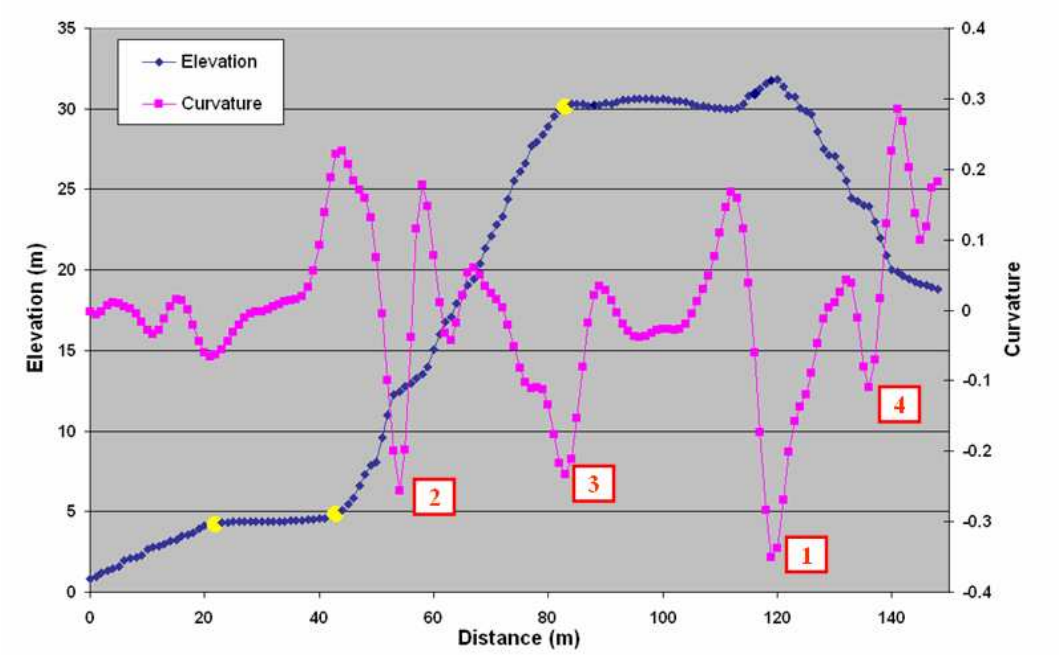

Figure 4.12 Adjustment of dune crest location using compatibility values

Table 4.1 Compatibility values calculated based on contextual information

Local minimum point	Curvature	Distance (meter)	Elevation (meter)	Compatibility
1	-0.3505	119	31.79	0.00064
2	-0.2569	54	12.45	0.00021
3	-0.2336	82	30.12	0.25300
4	-0.1101	136	23.97	1.91E-05

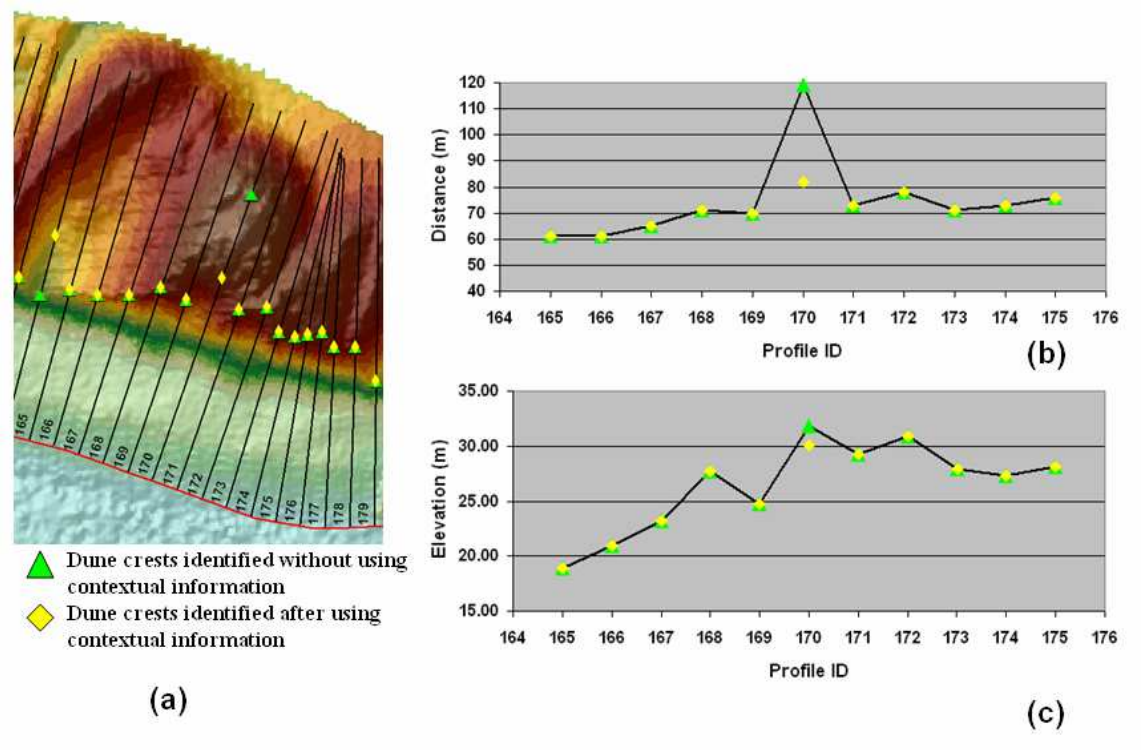

Figure 4.13 Example of dune crests identification. (a) Comparison between dune crests identified before and after incorporating contextual information; (b) Improved consistency in horizontal distance from origin point; (c) Improved consistency in elevation values

Using the similar algorithm, the location of the beach berm crest of each profile can be adjusted by incorporating the contextual information. Then the dune toe can be relocated based on the updated location of berm crest and dune crest.

4.2.3 Procedures for deriving morphologic attributes for beach profiles along the shoreline

The traditional ground survey transects are approximately perpendicular to the shoreline. Similarly, to automatically generate beach profiles from LiDAR DEM, the first step is to extract the shoreline as the reference to orientate transects. Shoreline is the spatially continuous line of contact between the land and the sea. More accurately, shoreline is defined as the intersection line between the land and the mean high water level (MHWL). This definition is adopted by many US agencies such as the United States Army Corps of Engineers, Federal Emergency Management Agency, and U.S. Census Bureau (Graham et al., 2003). Based on LiDAR elevation data, shoreline can be extracted using object-based or contour-based approach. In most cases, the shoreline extracted from high resolution LiDAR data contains too much spatial detail for generating perpendicular transects. The shoreline needs to be smoothed to eliminate the unnecessary details to ensure the orientation of transects vary smoothly and gradually.

After the shoreline is extracted and smoothed, the location of the starting point of each transect can be determined along the shoreline at a regular interval. The length of the transects can be specified according to the practical needs at particular study area. The orientation of each transect is calculated based on the local segments of the shoreline. A moving window with a selected size is centered at the starting point of each profile. A linear regression line is fit for the shoreline within the window. The orientation of the profile is then set to be perpendicular to this local regression line.

After the transects are located, the corresponding elevation values can be extracted from the LiDAR DEM along each transect line. The Gaussian filter at optimum scale is applied to smooth the elevation curve. The first derivative, second derivative, and curvature are then derived for the smoothed elevation curve to extract the critical beach features from each individual beach profile. Then the contextual information from the neighborhood of each beach profile can be incorporated to identify the feature points that are not consistent with its neighbors in terms of elevation and/or horizontal distance. The locations of those incompatible feature points can be adjusted based on the compatibility analysis of candidate locations.

After the feature points for each beach profile are derived, the feature points on beach profile and the segments between feature points can be converted from raster-based grid format to vector-based point and polyline format. Both the raster and vector representations of the points and segments of the profile are maintained in the database. For raster representation, each profile is stored as a series of grid cells with the ID number of feature points. For vector representation, the feature points and segments are located on the profile using linear referencing and dynamic segmentation techniques. By definition, linear referencing is the method of storing geographic location by using relative positions along a measured linear feature, while the dynamic segmentation refers to the process of calculating the absolute locations of events using linear referencing system and locating them on the map (Brennan and Harlow, 2002). First, a route can be created from each profile line by using profile length to accumulate the route measures. Then a point event table can be created for all the feature points, which records the ID of

the profile that each point belongs to, as well as the distance of the feature point to the origin point of the profile. At last, a route event layer can be generated based on profile routes and point event table by linking the points to the corresponding profile using route ID, and locating the points on the profile using its distance from the origin point as measure values. Similarly, a line event table can be created for all the segments between feature points. A route event layer can be generated using profile routes and line event table by linking each segment to its corresponding profiles using route ID, and locating the segments on the profile using the distance measurement of its from-point and to-point. Compared to raster representation, the vector format of feature points and segments of profile is much easier to be displayed, edited, and analyzed in a GIS environment in association with other data layers.

4.2.4 Derivation of attributes for characterizing beach profiles and profile changes

Based on the object representation of feature points and segments of each profile, a set of attributes can be extracted to support a detailed quantitative analysis of coastal morphology in the cross-shore direction. For beach feature points such as berm crest, dune crest, and dune toe, the elevation of the points and their horizontal distance from the origin point of corresponding profile can be calculated. For segments between the point features, such as dune face and beach berm, the corresponding height, width, and slope of each segment can be derived.

If time series of profiles from repeat LiDAR surveys are available, the magnitude of changes can be calculated for each attributes, such as the horizontal and vertical displacement of each feature point, as well as the change in height, width, and slope of

each segment along the profile. The dune volumetric change is calculated based on the horizontal position of pre-surface dune toe and the dune crest location that is furthest from shoreline among different time periods. Limited by the water penetration ability of topographic LiDAR system, the beach volumetric change can only be calculated from the position of shoreline to the horizontal position of pre-surface dune toe.

4.3 ArcGIS extension module for beach profile analysis

To support the beach profile feature extraction and attribute derivation, an ArcGIS extension module – Profile Analyst, is developed in the environment of Microsoft Visual Studio .NET 2003. The core algorithms are programmed as a series of DLLs using the C++ language, and the graphical interface is developed by VB .NET and the relevant ArcObjects. This extension module can be used seamlessly with ArcGIS package. The graphical interface for Profile Analyst is shown in Figure 4.14. The capabilities of this module include:

(1) Generate cross sections: This software routine has a customized dialogue menu which guides the user to load the input data and to set the relevant parameter values to delineate cross sections (Figure 4.14b). The required input data are LiDAR DEM and shoreline, which may be extracted or digitized based on LiDAR data and /or high-resolution remote sensing imagery. The parameters to be specified include the beach profile length and profile interval. Transects perpendicular to the shoreline can be automatically generated at the specified interval. The elevation values for all the grids on each transect can be sampled from the LiDAR DEM and be stored as a list in memory.

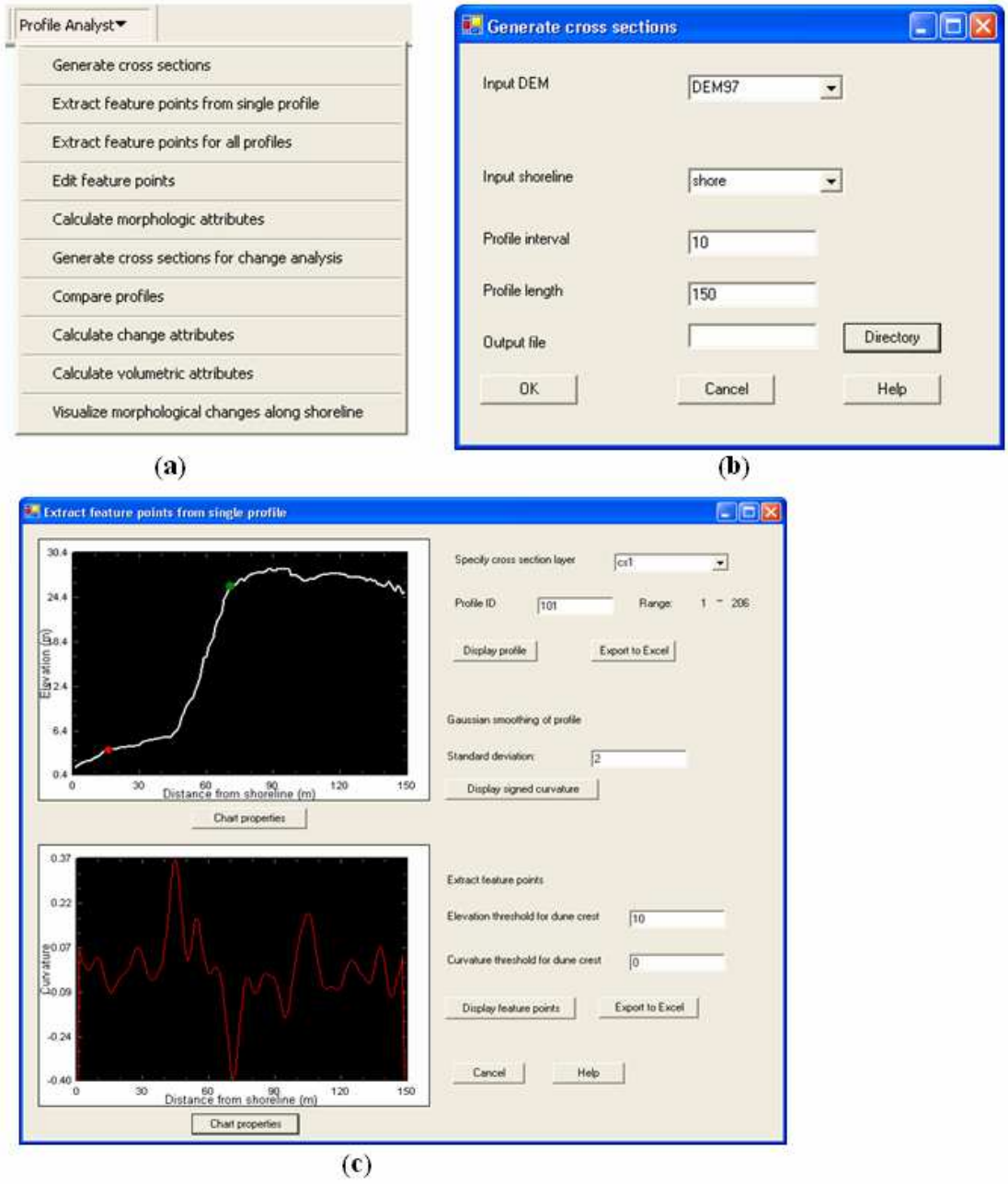

Figure 4.14 ArcGIS extension module – Profile Analyst. (a) Pull-down menu for the extension module; (b) Dialogue form for generating cross sections; (c) Dialogue form for extracting feature points from single profile; (d) Dialogue form for extracting feature points for all profiles; (e) Dialogue form for editing feature points; (f) Dialogue form for calculating morphologic attributes; (g) Dialogue form for generating cross sections for change analysis; (h) Dialogue form for comparing profiles; (i) Dialogue form for calculating change attributes;(j) Dialogue form for calculating volumetric attributes; (k) Dialogue form for visualizing morphological changes along shoreline

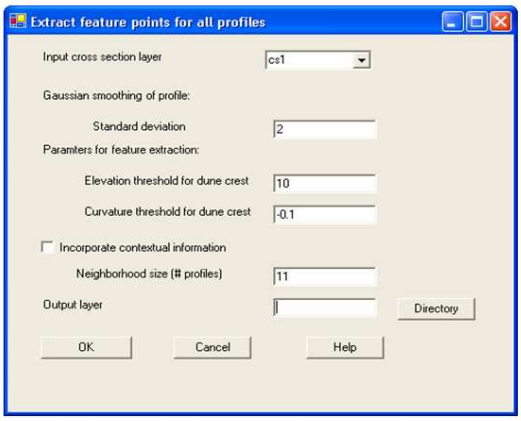

(d)

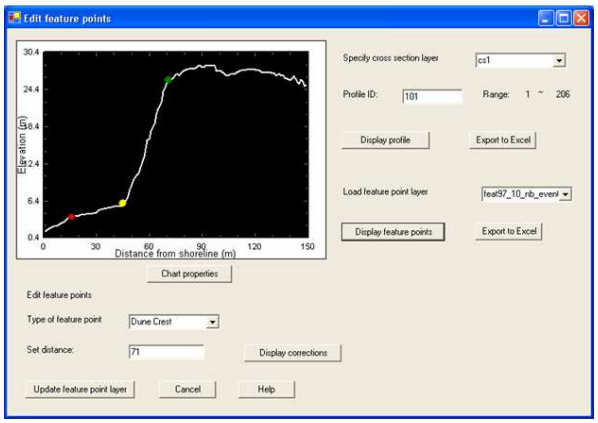

(e)

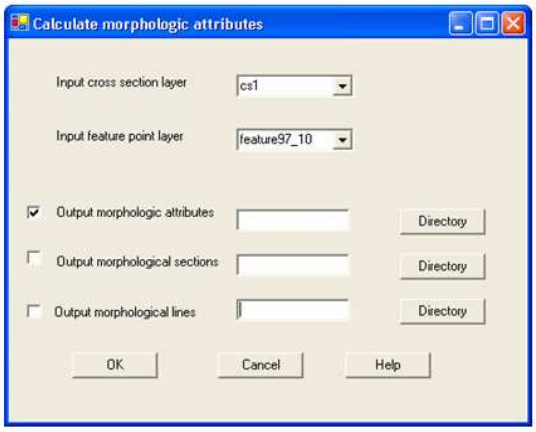

(f)

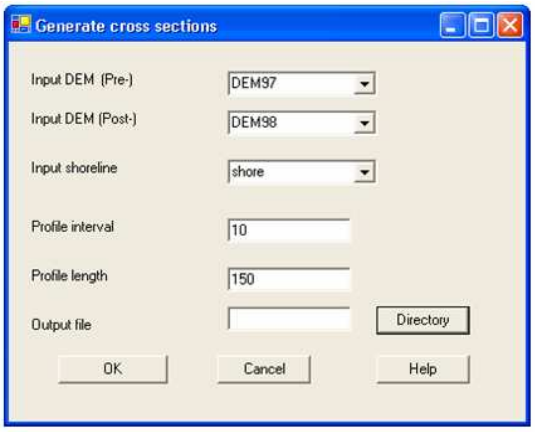

(g)

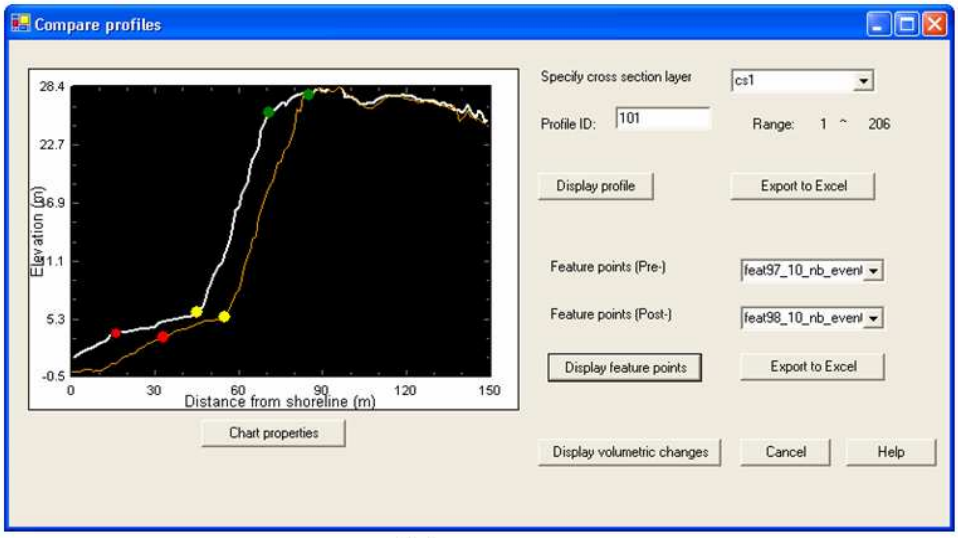

(h)

Figure 4.14 (Continued)

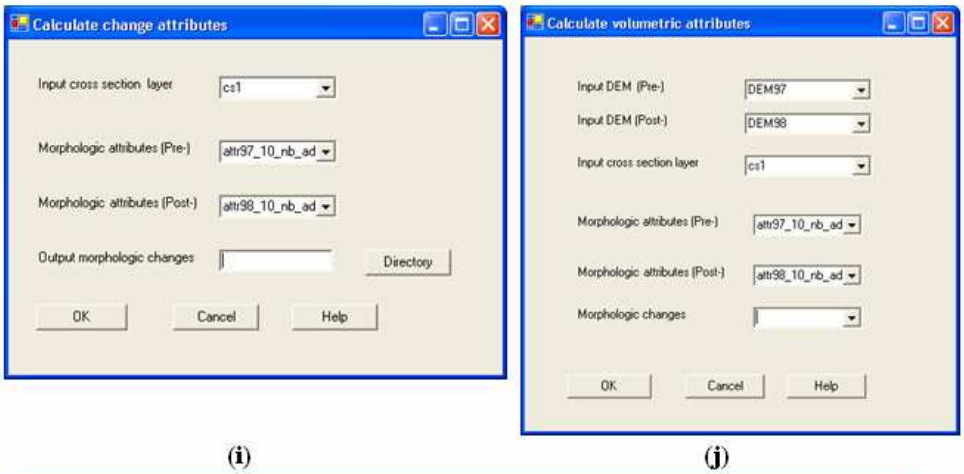

(i) (j)

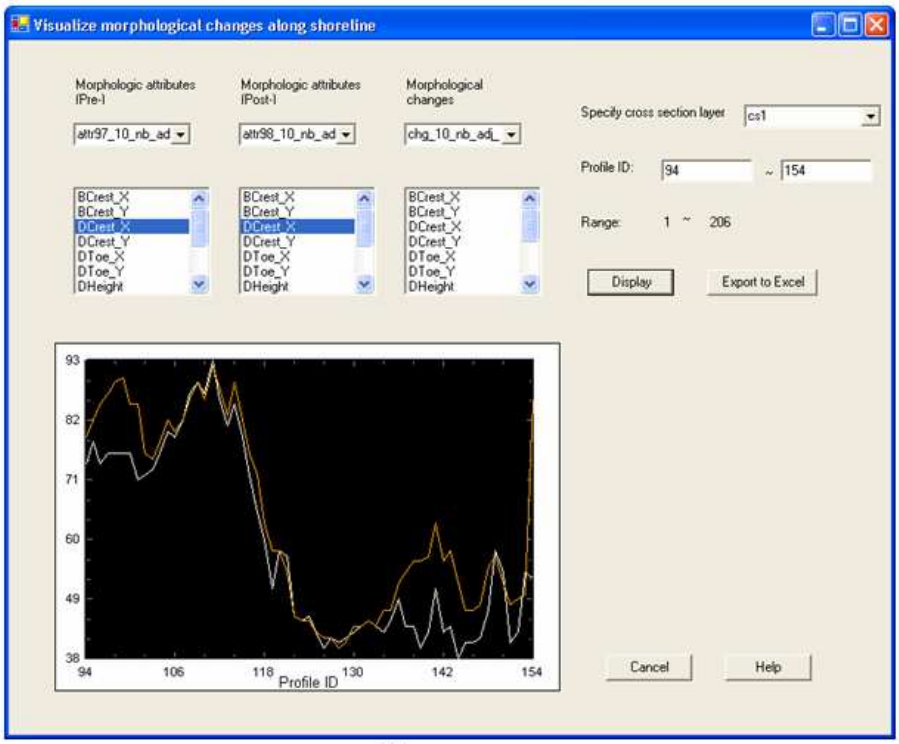

(k)

Figure 4.14 (Continued)

(2) Interactively extract feature points from single profile: This routine allows the user to preview selected profile curve and to determine appropriate parameters for feature extraction (Figure 4.14c). First, the selected profile curve can be displayed. The standard deviation value can be set for the Gaussian filter to smooth the original elevation curve at different scales, and the resulting signed curvature curve can be displayed in a separate window. By setting a vertical threshold to roughly divide the profile into beach zone and dune zone, the resulting feature points could be derived and displayed on the beach profile. After several experiments on various profiles, the optimum scale of analysis and the elevation threshold can be determined. The elevation values along the profile and the coordinates for identified feature points can be exported to Excel for a detailed analysis.

(3) Extract feature points for all profiles: After the optimal parameters are determined based on experiments on representative profiles, this software routine allows users to apply these parameters for the case study area to extract critical features (Figure 4.14d). Feature points can be extracted based on geometric information of each individual beach profile, and can also be adjusted by incorporating the contextual information from the neighboring profiles. To incorporate the contextual information, the user needs to set the number of profiles in the neighborhood to calculate the compatibility value.

The resulting feature points such as beach berm crest, dune/bluff crest and dune/bluff toe are initially stored in memory as distance-elevation pair for each profile. By using a set of ArcObjects related to linear referencing and dynamic segmentation in

ArcGIS, the feature points and segments can be saved in event tables and be displayed in vector format.

(4) Edit feature points: After the automatic profile feature extraction, the manual editing can fix feature points that are not correctly located by the automatic algorithms (Figure 4.14e). For a selected profile, the distance-elevation pair of feature points can be read from the feature point layer created by previous steps and be displayed on the corresponding elevation curve. With this software routine, the location of the feature points can be interactively edited, added, or deleted. The feature point layer can be updated after the new location of feature point is determined.

(5) Calculate morphologic attributes: After the automatic feature extraction and manual editing, a set of morphological attributes can be derived for each beach profile (Figure 4.14f). The attributes for feature point include the elevation and the horizontal distance to the shoreline. The attributes for dune/bluff face and beach berm include the height, width, and slope. The feature points of the same type can be connected to form the feature line, such as dune crest line, dune toe line, and berm crest line.

(6) Generate cross sections for change analysis: This routine allows user to perform change analysis between two successive LiDAR surveys (Figure 4.14g). The user can specify the two LiDAR DEMs to be compared and the reference shoreline. Similar to the single DEM analysis, the user is allowed to set the beach profile length and profile interval. After transects are generated, the elevation values can be extracted for two DEMs along each transect.

(7) Compare profiles: This routine allows user to compare the elevation profiles measured at two different time periods (Figure 4.14h). The identified feature points can be displayed on the profiles to reveal their displacements. The cut and fill areas can be displayed on the cross-shore view and the total volumetric change for each profile can be calculated.

(8) Calculate change attributes: This routine allows user to calculate the attribute changes during the temporal span between two LiDAR surveys (Figure 4.14i). The change attributes include the horizontal distance and elevation changes for feature points, as well as the height, width, and slope change for dune/bluff face and beach berm. The volumetric change attributes are also derived for beach and dune sections (Figure 4.14j).

(9) Spatial pattern of profile feature attributes and change attributes: This routine facilitates the visualization of the spatial variations of morphologic attributes for each survey and the analysis of change attributes between two surveys (Figure 4.14k). Several attributes can be selected and displayed at the same time, which is helpful in interpreting and analyzing coastal morphological change patterns.

5 OBJECT-BASED METHOD FOR MORPHOLOGICAL AND VOLUMETRIC CHANGE ANALYSIS

This section presents the object-based method for morphological and volumetric change analysis. The object-oriented method represents a two-dimensional approach to the analysis of coastal morphology and its changes. The basic spatial units for object-oriented analysis method are the erosion and deposition patches and zones, in contrast to the profiles in the one-dimensional profile analysis approach. This section starts with the presentation of algorithms for identifying and delineating the positive change and negative change objects. Then, algorithms and software tools are presented for deriving attributes for characterizing these morphological change objects.

5.1 Identification and delineation of elevation change objects

The main procedures of change object identification and delineation include three steps: pixel-based elevation differencing, morphological change classification, and object identification.

For change analysis, LiDAR surveys at two different times for the same region needs to be preprocessed, including geo-referencing, horizontal co-registration, vertical adjustment, and low-pass filtering. Then, the two LiDAR DEMs can be differenced for change analysis as in Equation (5.1):

$$\Delta z_{ij} = z_{ij}^{t2} - z_{ij}^{t1} \tag{5.1}$$

where z_{ij}^{t1} and z_{ij}^{t2} are the elevation measurements for the cell (i, j) respectively at the early time t_1 and the late time t_2, and Δz_{ij} is the elevation difference for the cell (i, j). A

positive elevation difference value indicates that the surface materials have been added at this location, while a negative elevation difference value indicates that the surface materials have been removed (Figure 5.1c).

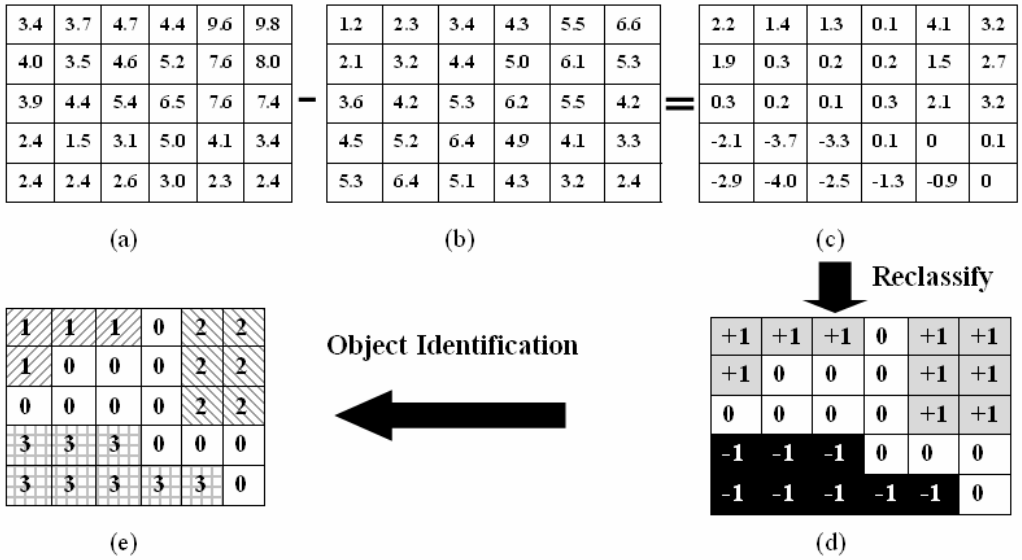

Figure 5.1 Identification of elevation change objects. (a) DEM at the time t_2; (b) DEM at the time t_1; (c) Elevation difference values; (d) Morphological change classification values; (e) Resulting objects with ID numbers

In the resulting pixel-based elevation difference imagery, the cells with elevation change value can be further classified into three morphological change categories: positive change cells, negative change cells, and unchanged cells (Figure 5.1d). As discussed in Section 3, "Unchanged" can be defined as the case when elevation change value is within a range of the measurement error. Given σ_d as the random error for elevation difference measurements and k as the multiplicative factor (usually ranging from 1.0 to 3.0), the elevation differencing image could be reclassified into three categories: positive change (1), negative change (-1), and unchanged (0) according to Equation (5.2):

$$c_{ij} = \begin{cases} 1, & if\ \Delta z_{ij} > k\sigma_d \\ -1, & if\ \Delta z_{ij} < -k\sigma_d \\ 0, & if -k\sigma_d < \Delta z_{ij} < k\sigma_d \end{cases} \quad (5.2)$$

where c_{ij} is the morphological change code for the grid cell (i, j).

In this object-based volumetric change analysis method, the unchanged cells are considered as background and the individual positive change and negative change patches are considered as objects (Figure 5.1e). For example, a positive change object is defined as a continuous spatial aggregation of cells with a positive elevation change value, in which any two cells are spatially connected. Two cells are considered to be spatially connected if there exits a path between two cells that consists of a series of adjacent cells. In this case, two cells are defined as adjacent to each other when one cell is the four immediate neighbor of the other. A recursive connected-component expansion algorithm (Sonka et al., 1999; Liu and Jezek, 2004) is used to identify and index positive change objects based on the spatial connectivity of cells. First, the elevation difference grid is scanned in a row-wise manner, and a seed is set at the first cell with a positive elevation change value. Second, this seed is expanded to include all the positive change cells located in the four immediate neighborhood of the current cell. The expansion is continued recursively until all the spatially connected positive change cells are included in the current patch. In this way, the first positive change object is delineated and indexed. As repeating this recursive expansion process to identify positive change objects one-by-one, the objects are indexed incrementally with a unique identification number. Following the same procedure, the negative change objects could

be delineated and indexed. Positive (negative) change objects with different identification numbers are spatially detached to each other, which is guaranteed by the algorithm. However, a positive change object and a negative change object might be adjacent to each other. As a final result, the recursive connected-component expansion algorithm creates a series of discrete elevation change objects which are embedded in the background of unchanged cells.

When applying the algorithm to real LiDAR data, the identification of objects may be subject to errors for various reasons such as data noise, residual horizontal alignment error, and resolution limitation during image acquisition. The delineated objects may have small holes and breaks, and their boundaries may have a rough and jagged shape. To generalize the shape of the objects, three steps of morphology operations are applied. First, a closing operation (Sonka et al., 1999) is applied to smooth the object boundaries and close the small gaps in objects. The closing operation consists of a dilation operation followed by an erosion operation. The dilation operation adds cells to the perimeter of each object, and thus potentially closes broken areas. Erosion operation etches cells away from the perimeter of each object and therefore shrinks the object. Second, a fill operation is applied to close small interior holes and cavities whose size is smaller than a specified threshold. Third, a trim operation is applied to eliminate those isolated objects whose size is smaller than the specified threshold.

After the discrete objects are generalized by the morphologic operations, they are converted from raster-based grid format to vector-based polygon format. Both the raster

and vector representations of the objects are maintained in the database. For raster representation, each object is stored as a list of spatially-connected grid cells with a same identification number, and the object attributes are stored in an associated attribute table with the same identification number. For vector representation, each object is stored as a polygon, and a feature attribute table is associated with the polygon layer. The feature attribute table contains object identification numbers and various spatial and volumetric properties of corresponding objects as described in the next section. The vector format of elevation change objects can be directly displayed, edited and analyzed in a GIS environment in association with other data layers.

5.2 Attribute derivation for characterizing erosion and deposition objects

Based on the object representation of elevation change patches, a set of spatial and volumetric attributes can be derived to support a detailed quantitative analysis of coastal morphology change. Individual elevation change patch is treated as the basic spatial units for morphological and volumetric change analysis. First, the internal composition and heterogeneity for each object can be characterized by a set of variables. For example, the range and standard deviation of vertical elevation changes could describe the internal heterogeneity of elevation changes within an object. Second, each object could be treated as homogenous entities and be characterized by a set of spatial and volumetric properties. Third, the spatial pattern of erosion and deposition objects could be measured by aggregation and distribution properties, over specified sub-regions or across the entire landscape.

From successive LiDAR datasets, five categories of attributes are calculated for each elevation change object, which include planimetric attributes, shape attributes, surface attributes, volumetric attributes, and summary statistical attributes. The combination of these attributes could provide comprehensive quantitative information for investigating morphological and volumetric characteristics of elevation change patches. Thematic attributes could also be calculated for each object if other ancillary data sources such as multi-spectral remote sensing imagery are incorporated. A combination of various attributes could facilitate the classification of elevation changes caused by different mechanisms.

This research aims at providing an analytical framework and software tool for object-based morphological and volumetric change analysis, so that a large list of attributes are deduced and calculated. For specific research purpose or specific study area, the users may select the attributes that are most useful for characterizing particular aspects of coastal morphology.

5.2.1 Planimetric attributes

The planimetric attributes describe the geographical position, horizontal dimensions and size of the elevation change objects. Those include the coordinates $(\bar{x}, \bar{y})$ of centroid point, perimeter (p), area (A), thickness (THK), as well as the length (l) and width (w) of the minimum bounding rectangle. The numerical definitions of these attributes are listed in Table 5.1. The centroid point is the gravity center of the object and indicates the geographical location of the object. The perimeter measures the length of the object boundary. The thickness of an object is defined as the maximum distance of interior cells

of the object to its nearest boundary, namely the distance of the deepest cell inside the object to its boundary. The length and width of the minimum bounding rectangle gives the measurements on the horizontal dimensions of the object.

Table 5.1 Definitions of planimetric attributes

Attributes	**Definition**
Centroid point ($\bar{x}, \bar{y}$)	$\bar{x} = \frac{1}{n}\sum_{i=1}^{n} x(i); \quad \bar{y} = \frac{1}{n}\sum_{i=1}^{n} y(i)$ *n* is the number of cells consisting of an object, (x_i, y_i) are the horizontal and vertical coordinates of the *i*th cell of the object
Perimeter (*P*)	$p = m_1 r + \sqrt{2} m_2 r$ m_2 is the number of boundary cell in diagonal step, m_1 is the number of boundary cell in horizontal or vertical orientation, and r is the grid cell size
Area (*A*)	$A = nr^2$ *n* is the number of cells consisting of an object, and *r* is the grid cell size.
Thickness (*THK*)	$THK = \max\{d_i\}$ d_i is the distance of the cell *i* to the nearest boundary.
Length (*l*)	length of the minimum bounding rectangle enclosing the object
Width (*w*)	width of the minimum bounding rectangle enclosing the object

5.2.2 Shape attributes

Shape attributes describe the planar geometric shape of the objects. Due to the differences in the nature of changes and diverse coastal processes, the elevation change objects may have different shape characteristics and complexity. Some have compact forms, while others have narrow and elongated shapes. Some have simple, regular, and

smooth boundaries, while others have convoluted, rugged and complex boundaries. The different shape characteristics of elevation change objects could be used to facilitate the inference of the underlying coastal processes. A set of attributes are calculated for characterizing different aspects of the shape property, including compactness index (*CI*), elongatedness (*ELG*), asymmetry (*ASM*), orientation (ϕ), fractal dimension (*D*), rectangularity (*REC*), ellipticity (*ELP*), and triangularity (*TRI*) (**Table 5.2**).

Compactness index (CI) is a widely used shape indicator (Davis, 2002), which is defined based on the perimeter and area measure of the object. The most compact object in a Euclidean space is a circle. A circle-shaped object has a compactness index of one, and so that the compactness index is also known as the circularity measure (Pratt, 1991). Elongatedness is defined as a ratio between the length and width of the fitted minimum bounding rectangle. The circle and square have the smallest value for the elongatedness, which equals to one. The asymmetry is defined based on the best-fit ellipse of the object, which is the ratio of the major and minor axes of the ellipse. The circle and square have an asymmetry value of zero. The orientation is defined as an angle in degree between the horizontal axis and the major axis of the best-fit ellipse measured counterclockwise from 0 to 180.

Rectangularity, ellipticity and triangularity respectively measure the similarity of the shape of an object to typical rectangle, ellipse and triangle shapes. The rectangularity is defined by the ratio between the area of the object to the area of the minimum bounding rectangle. The ellipticity and triangularity are defined based on the affine moment invariant (Flusser and Suk, 1993; Rosin, 1993). All the rectangularity, ellipticity,

and triangularity values range from 0 to 1. The larger the value, the more similar an object is to the corresponding typical shape.

Table 5.2 Definitions of shape attributes

Attributes	**Definition**
Compactness index (*CI*)	$CI = \frac{4\pi A}{p^2}$
Elongatedness (*ELG*)	$ELG = \frac{l}{w}$
Asymmetry (*ASM*)	$ASM = 1 - \frac{b}{a}$ $\quad \mu_{pq} = \frac{1}{n}\sum_{i-1}^{n}(x_i - \bar{x})^p (y_i - \bar{y})^q$ $a = \sqrt{\frac{2(\mu_{20} + \mu_{02} + \sqrt{(\mu_{20} - \mu_{02})^2 + 4\mu_{11}^2})}{\mu_{00}}}$ $b = \sqrt{\frac{2(\mu_{20} + \mu_{02} - \sqrt{(\mu_{20} - \mu_{02})^2 + 4\mu_{11}^2})}{\mu_{100}}}$ *a* and *b* are the semi-major and semi-minor of the best-fit ellipse, μ_{pq} are the central moments.
Orientation (ϕ)	$\phi = \frac{1}{2}\tan^{-1}\left(\frac{2\mu_{11}}{\mu_{20} - \mu_{02}}\right)$ μ_{pq} are the central moments.
Fractal dimension (*D*)	$N(r) = cr^{1-D}$ *r* is the width of box, N(r) is the counts of the boxes contain the object.
Rectangularity (*REC*)	$REC = \frac{A}{lw}$
Ellipticity (*ELP*)	$ELP = \begin{cases} 16\pi^2 I_1 & \text{if } I_1 \le 1/16\pi^2 \\ \frac{1}{16\pi^2 I_1} & \text{otherwise} \end{cases}$ $I_1 = \frac{\mu_{20}\mu_{02} - \mu_{11}^2}{\mu_{00}^4}$ μ_{pq} are the central moments and I_1 is the affine moment invariant.
Triangularity (*TRI*)	$TRI = \begin{cases} 108 I_1 & \text{if } I_1 \le 1/108 \\ \frac{1}{108 I_1} & \text{otherwise} \end{cases}$ I_1 is the affine moment invariant.

The shape complexity of object boundary can be measured in terms of a perimeter-to-area ratio or fractal dimension (Mandelbrot 1983, Burrough 1981). Both the perimeter-to-area ratio and the fractal dimension increase with the increasing complexity of the object boundary. The problem with the perimeter-area ratio method is that it is size dependent. For two objects of the same shape, the larger object has a lower perimeter-area ratio than that of the smaller object. To avoid the size dependency problem of perimeter-area ratio, the fractal dimension is selected as the indicator to measure the complexity of object boundary. The fractal dimension is calculated for each object using the box-counting method, which includes the following steps (Foroutan-pour, 1999):

Step 1: Use a grid with a cell size r_i to cover the object, and then count the number of cells N_i that contain part of the boundary of object.

Step 2: Vary the cell size and record a series of counts $\{ r_1, N_1 \}$, $\{ r_2, N_2 \}$, …, $\{ r_m, N_m \}$.

Step 3: Fit a linear regression line of points $\{ \log(r_1), \log(N_1) \}$, $\{ \log(r_2), \log(N_2) \}$, …, $\{ \log(r_m), \log(N_m) \}$.

Step 4: Determine the fractal dimension *D* using the linear regression equation:

$$\log(N(r)) = \log(K) + D\log(r) \qquad (K \text{ is a constant}) \qquad (5.3)$$

To generalize the shape and orientation of each object, a minimum bounding rectangle could be fitted to enclose the object, which is the smallest rectangle that contains all cells of the object and aligned with the major and minor principal axes of the

object (Figure 5.2). The algorithms of determining minimum bounding rectangle include the following steps (Chaudhuri and Samal 2007; Suesse and Voss, 2001):

Step 1: Compute the centroid point $(\bar{x}, \bar{y})$ of object and the angle of the major axis with the horizontal axis θ (Figure 5.3a).

Step 2: Compute the upper and lower furthest boundary points with respect to both major and minor axes (Figure 5.3b). Each boundary point (x_i, y_i) can be classified to be upper, lower, and on with respect to the major axis using:

$$V = (y_i - \bar{y}) - \tan\theta(x_i - \bar{x}) \tag{5.4}$$

Boundary point (x_i, y_i) is an upper boundary point with respect to major axis when $V > 0$, a lower boundary point when $V < 0$, and on the major axis if $V = 0$. Then the upper and lower furthest boundary points with respect to major axis could be determined within each groups. Similarly, by using $U = (y_i - \bar{y}) + \cot\theta(x_i - \bar{x})$, the upper and lower furthest boundary points with respect to minor axis could be determined.

Step 3: Compute the vertices of the four corners of the minimum bounding rectangle (Figure 5.3c). Let (x_1, y_1) and (x_2, y_2) be the upper and lower furthest boundary points with respect to major axis, and let (x_3, y_3) and (x_4, y_4) be the upper and lower furthest boundary points with respect to minor axis. The vertices are determined by finding the intersections of four lines: two lines are parallel to major axis and respectively pass through (x_1, y_1) and (x_2, y_2); another two lines

are parallel to minor axis and respectively pass through (x_3, y_3) and (x_4, y_4). The resulting coordinates of the four corners are:

Top left corner A:

$$x = \frac{x_1 \tan\theta + x_3 \cot\theta + y_3 - y_1}{\tan\theta + \cot\theta} \tag{5.5}$$

$$y = \frac{y_1 \cot\theta + y_3 \tan\theta + x_3 - x_1}{\tan\theta + \cot\theta} \tag{5.6}$$

Top right corner B:

$$x = \frac{x_1 \tan\theta + x_4 \cot\theta + y_4 - y_1}{\tan\theta + \cot\theta} \tag{5.7}$$

$$y = \frac{y_1 \cot\theta + y_4 \tan\theta + x_4 - x_1}{\tan\theta + \cot\theta} \tag{5.8}$$

Bottom left corner C:

$$x = \frac{x_2 \tan\theta + x_3 \cot\theta + y_3 - y_2}{\tan\theta + \cot\theta} \tag{5.9}$$

$$y = \frac{y_2 \cot\theta + y_3 \tan\theta + x_3 - x_2}{\tan\theta + \cot\theta} \tag{5.10}$$

Bottom right corner D:

$$x = \frac{x_2 \tan\theta + x_4 \cot\theta + y_4 - y_2}{\tan\theta + \cot\theta} \tag{5.11}$$

$$y = \frac{y_2 \cot\theta + y_4 \tan\theta + x_4 - x_2}{\tan\theta + \cot\theta} \tag{5.12}$$

Step 4: Connect the corresponding vertices to get the minimum bounding rectangle of the current object.

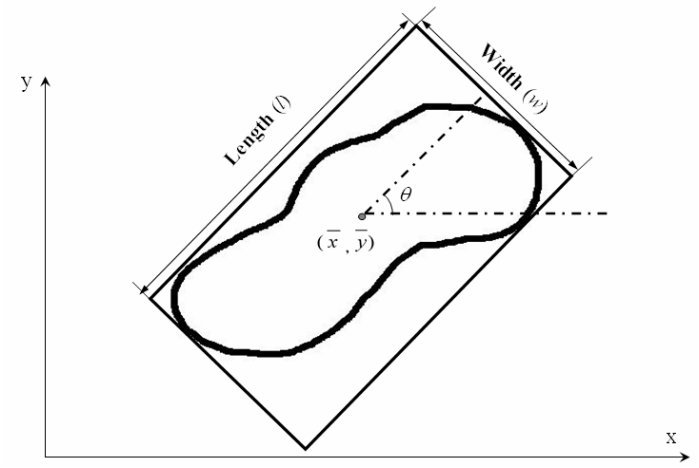

Figure 5.2 A minimum bounding rectangle and its parameters

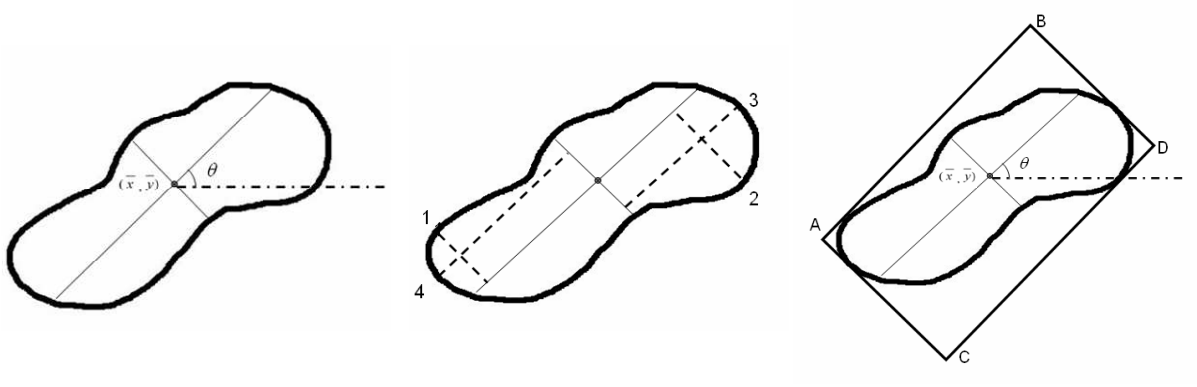

(a) (b) (c)

Figure 5.3 Steps of fitting minimum bounding rectangle. (a) Centroid and axes; (b) Upper and lower furthest points; (c) Vertices of minimum bounding rectangle

The best-fit ellipse of an object can be determined using all the cells within the object (Figure 5.4). The center of the ellipse is located at the centroid point. The principal axes of the ellipse are the eigenvector of the covariance matrix obtained by treating the cells within the object as random variables. The major principal axis corresponds to the eigenvector of the larger eigenvalue. Three parameters of the ellipse including semi-major axis (a), semi-minor axis (b), and orientation (ϕ) can be calculated

using the lower-order central moments of the objects (Teague, 1980; Mulchrone and Choudhury, 2004). The algorithms of determining best-fit ellipse include the following steps:

Step 1: Compute the centroid point $(\bar{x}, \bar{y})$ of the object.

Step 2: Compute the central moments of the object:

$$\mu_{pq} = \sum_{i=1}^{n} (x_i - \bar{x})^p (y_i - \bar{y})^q \qquad (p = 0, 1; q = 0, 1) \tag{5.13}$$

Step 3: Compute the semi-major axis, semi-minor axis, and orientation of the ellipse

$$a = \sqrt{\frac{2(\mu_{20} + \mu_{02} + \sqrt{(\mu_{20} - \mu_{02})^2 + 4\mu_{11}^2})}{\mu_{11}}} \tag{5.14}$$

$$b = \sqrt{\frac{2(\mu_{20} + \mu_{02} - \sqrt{(\mu_{20} - \mu_{02})^2 + 4\mu_{11}^2})}{\mu_{11}}} \tag{5.15}$$

$$\phi = \frac{1}{2} \tan^{-1}\left(\frac{2\mu_{11}}{\mu_{20} - \mu_{02}}\right) \tag{5.16}$$

Step 4: Draw the best-fit ellipse.

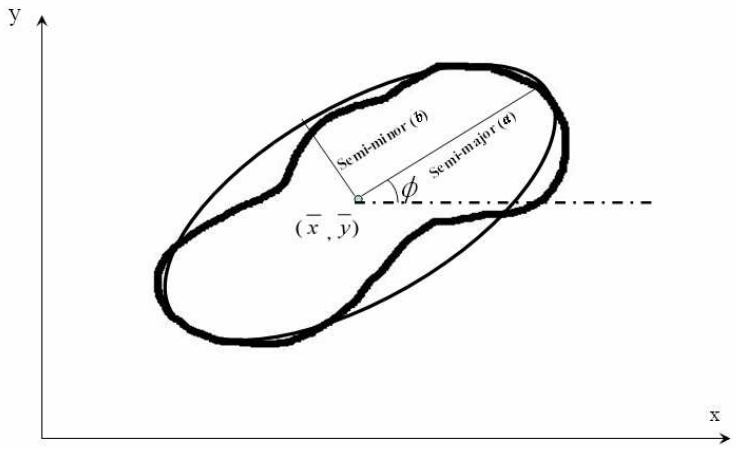

Figure 5.4 Best-fit ellipse and its parameters

5.2.3 Surface attributes

Surface attributes describe the three-dimensional surface morphology and its changes in terms of slope, aspect and curvature. To support the exploration of the interaction and relationship between surface geomorphology and the coastal processes, a set of surface attributes are calculated for each elevation change object, which includes: original-surface average elevation (*AV_EL1*), subsequent-surface average elevation (*AV_EL2*), average elevation difference (*AV_EL_DIF*), original-surface average slope (*AV_SL1*), subsequent-surface average slope (*AV_SL2*), surface slope difference (*AV_SL_DIF*), original-surface average aspect (*AV_AS1*), subsequent-surface average aspect (*AV_AS2*), average surface aspect difference (*AV_AS_DIF*), original-surface curvature (*AV_CV1*), subsequent- surface curvature (*AVF_CV2*), and average surface curvature difference (*AV_CV_DIF*) (Table 5.3). The average value for surface elevation, slope (in percent rise), or curvature for original and subsequent surfaces are simply calculated as the arithmetic mean of all the cells within the object. The average value for surface aspect is calculated through trigonometric operations as it is a circular direction measure in degree (Davis, 2002). For aspect values θ_1, θ_2, …, θ_n, the average aspect is calculated as:

$$\theta_R = \arctan \frac{\sum_{i=1}^{n} \sin \theta_i}{\sum_{i=1}^{n} \cos \theta_i} \tag{5.17}$$

Table 5.3 Definitions of surface attributes

Attributes	**Definition**
Original-surface average elevation (*AV_EL*$_1$) Subsequent-surface average elevation (*AV_EL*$_2$) Average elevation difference (*AV_EL_DIF*)	$AV\_EL_1 = \frac{1}{n}\sum_{i=1}^{n} z_i^{t1} \qquad AV\_EL_2 = \frac{1}{n}\sum_{i=1}^{n} z_i^{t2}$ $AV\_EL\_DIF = AV\_EL_2 - AV\_EL_1$ z_i^{t1} and z_i^{t2} are the elevation of cell *i* of the object respectively at time *t1* and *t2*
Original-surface average slope (*AV_SL*$_1$) Subsequent-surface average slope (*AV_SL*$_2$) Average slope difference (*AV_SL_DIF*)	$AV\_SL_1 = \frac{1}{n}\sum_{i=1}^{n} s_i^{t1} \qquad AV\_SL_2 = \frac{1}{n}\sum_{i=1}^{n} s_i^{t2}$ $AV\_SL\_DIF = AV\_SL_2 - AV\_SL_1$ s_i^{t1} and s_i^{t2} are the slope of cell *i* of the object respectively at time *t1* and *t2*
Original-surface average aspect (*AV_AP*$_1$) Subsequent-surface average aspect (*AV_AP*$_2$) Average aspect difference (*AV_AP_DIF*)	$AV\_AP_1 = \tan^{-1}\left(\frac{\sum_{i=1}^{n}\sin\theta_i^{t1}}{\sum_{i=1}^{n}\cos\theta_i^{t1}}\right) \qquad AV\_AP_2 = \tan^{-1}\left(\frac{\sum_{i=1}^{n}\sin\theta_i^{t2}}{\sum_{i=1}^{n}\cos\theta_i^{t2}}\right)$ $AV\_AP\_DIF = AV\_AP_2 - AV\_AP_1$ θ_i^{t1} and θ_i^{t2} are the aspect of cell *i* of the object respectively at time *t1* and *t2*
Original-surface average curvature (*AV_CV*$_1$) Subsequent-surface average curvature (*AV_CV*$_2$) Average curvature difference (*AV_CV_DIF*)	$AV\_CV_1 = \frac{1}{n}\sum_{i=1}^{n} v_i^{t1} \qquad AV\_CV_2 = \frac{1}{n}\sum_{i=1}^{n} v_i^{t2}$ $AV\_CV\_DIF = AV\_CV_2 - AV\_CV_1$ v_i^{t1} and v_i^{t2} are the curvature of cell *i* of the object respectively at time *t1* and *t2*

5.2.4 Volumetric attributes

The volumetric attributes gives direct measurements on the magnitude and variation of elevation change within an object, which include average vertical change (Δz_{av}), maximum vertical change (Δz_{max}), standard deviation of vertical change (Δz_{std}), vertical change rate (*ZR*), volume change (*VOL*), and volume change rate (*VR*) (Table 5.4). The average vertical change (Δz_{av}) measures the central tendency of the elevation change for each object. The maximum vertical change (Δz_{max}) and the standard deviation of vertical change (Δz_{std}) measure the variation and the internal heterogeneity of the elevation change within each object. The vertical change rate (*ZR*) quantifies the average elevation change rate at a certain temporal scale. The volume change (*VOL*) and volume change rate (*VR*) quantify the total change in the volume of surface material during the time span between two surveys and the averaged change rate for each object.

5.2.5 Summary statistical attributes

After the erosion and deposition objects are identified based on a combination of planimetrc, shape, surface, and volumetric attributes, summary statistics can be calculated to quantify the extent, amount, spatial composition and configuration of overall erosion, deposition, and net change for a certain region. Summary statistical attributes include the number of erosion object (*NUM_ER*), average size of erosion objects (*AV_AREA_ER*), total erosion area (*AREA_ER*), total erosion volume (*VOL_ER*), the number of deposition object (*NUM_DE*), average size of deposition object (*AV_AREA_DE*), total deposition area (*AREA_DE*), total deposition volume (*VOL_DE*),

net volume change (*NET_VOL*), and annual net volume change rate (*NET_VOL_RT*) (Table 5.5).

Table 5.4 Definitions of volumetric attributes

Attributes	**Definition**
Average vertical change (Δz_{av})	$\Delta z_{av} = \frac{1}{n}\sum_{i=1}^{n}\Delta z_i$ Δz_i is the elevation change of cell *i* of the object
Maximum vertical change (Δz_{max})	$\Delta z_{\max} = \max\{\Delta z_i\}$
Standard deviation of vertical changes (Δz_{std})	$\Delta z_{std} = \frac{1}{n-1}\sqrt{\sum_{i=1}^{n}(\Delta z_i - \Delta z_{av})^2}$
Vertical change rate (*ZR*)	$ZR = \frac{\Delta z_{av}}{\Delta t}$ Δt is the elapsed time between two successive topography surveys (t2-t1)
Volume change (*VOL*)	$VOL = r^2\sum_{i=1}^{n}\Delta z_i$ r is the grid cell size
Volume change rate (*VR*)	$VR = \frac{VOL}{\Delta t}$

Table 5.5 Definitions of summary statistical attributes

Attributes	**Definition**
Number of erosion objects (*NUM_ER*) Number of deposition objects (*NUM_DE*)	*NUM_ER = Number of erosion objects* *NUM_DE = Number of deposition objects*
Total erosion area (*AREA_ER*) Total deposition area (*AREA_DE*)	$AREA\_ER = \sum_{j=1}^{NUM\_ER} A_j^e$ $AREA\_DE = \sum_{j=1}^{NUM\_DE} A_j^d$ A^e_j is the area of the *j*th erosion object A^d_j is the area of the *j*th deposition object
Average size of erosion object (*AV_AREA_ER*) Average size of deposition object (*AV_AREA_DE*)	$AV\_AREA\_ER = \frac{1}{NUM\_ER} \sum_{j=1}^{NUM\_ER} A_j^e$ $AV\_AREA\_DE = \frac{1}{NUM\_DE} \sum_{j=1}^{NUM\_DE} A_j^e$
Total erosion volume (*VOL_ER*) Total deposition volume (*VOL_DE*)	$VOL\_ER = \sum_{j=1}^{n1} VOL_j^e$ $VOL\_DE = \sum_{j=1}^{NUM\_DE} VOL_j^d$ VOL^e_j is the volume change of the *j*th erosion object. VOL^d_j is the volume change of the *j*th deposition object.
Net volume change (*NET_VOL*)	*NET_VOL=VOL_DE – VOL_ER*
Net volume change rate (*NET_VOL_RT*)	$NET\_VOL\_RT = \frac{NET\_VOL}{\Delta t}$

5.3 ArcGIS extension module for volumetric change analysis

To support the object-based morphological and volumetric change analysis method, an ArcGIS extension module – Coastal Volumetric Analyst, is developed under the environment of Microsoft Visual Studio .NET 2003. The core algorithm, including object identification and attribute derivation, are programmed as a series of DLLs (Dynamic-Link Library) using the C++ language. The graphical interface for the Volumetric Analyst extension module is developed through a VB .NET program that calls the DLLs and the relevant ArcObjects. The ArcObjects are a set of platform independent software components designed by ESRI Inc. specifically for programming with ArcGIS applications. This extension module can be used seamlessly with ArcGIS package.

The graphical interface for Coastal Volumetric Analyst is shown in Figure 5.5. This customized dialogue menu guides the user to load the input data, to set the relevant parameter values, and to select the attributes to be calculated for each objects. The required input data are two LiDAR DEMs, which are acquired at different time and cover the same area. After calculating the pixel-based elevation difference, the users could set the parameter of the relative error and multiplicative factor to determine the threshold of three morphological categories: positive change, negative change and unchanged. Before the object identification, the minimum object size could be determined to remove small noisy objects. The users can decide which groups of attributes are going to be calculated and included in the attribute table. In addition, the

user can choose to output the minimum bounding rectangles and the best-fit ellipses for all the elevation change objects as separate polygon layers.

The initial set of objects identified may include many change patches that were induced by various factors other than erosion and deposition. A combination of different attributes could be used to accomplish the classification of elevation change objects and distinguish the changes caused by erosion and deposition. Once the erosion and deposition objects are identified, the attributes can be selected and calculated for these objects again, so as to support the spatial analysis of morphological and volumetric change.

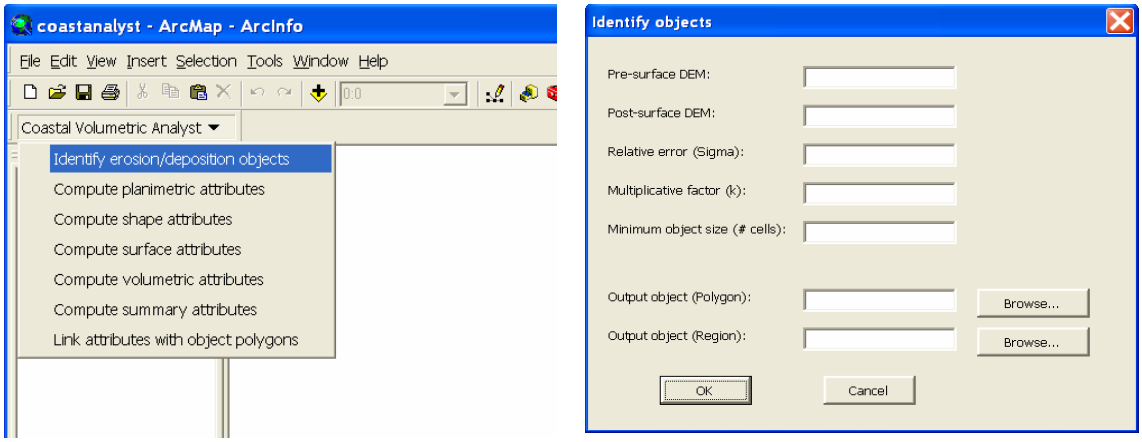

(a) (b)

Figure 5.5 ArcGIS extension module - Coastal Volumetric Analyst. (a) Pull-down menu for the extension module; (b) Dialogue form for identifying elevation change objects; (c) Dialogue form for computing planimetric attributes; (d) Dialogue form for computing shape attributes; (e) Dialogue form for computing surface attributes; (f) Dialogue form for computing volumetric attributes; (g) Dialogue form for computing summary statistical attributes; (h) Dialogue form for linking attribute tables with object polygon layer

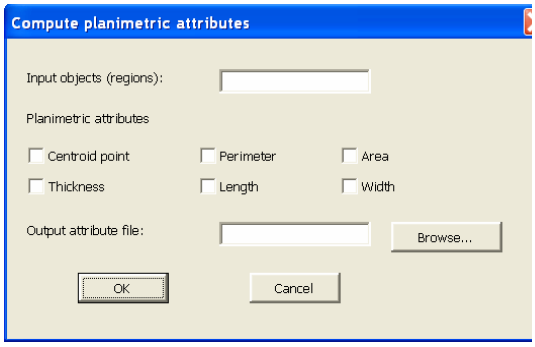

(c)

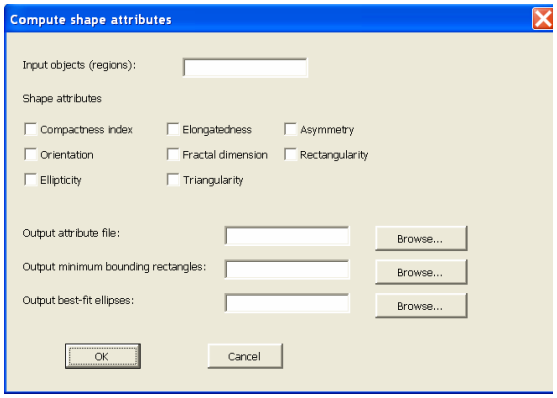

(d)

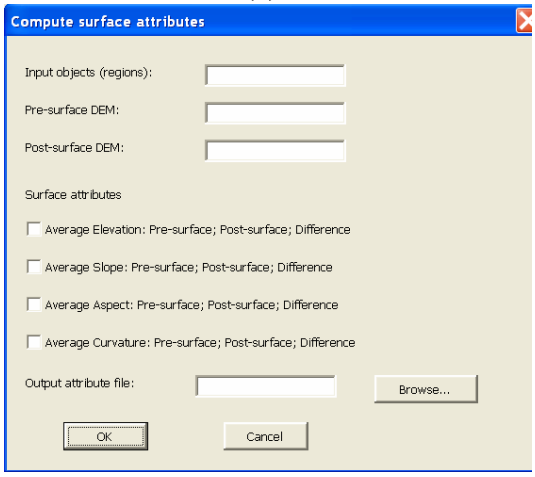

(e)

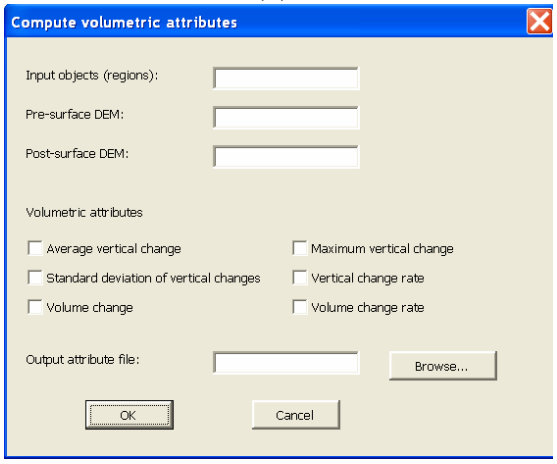

(f)

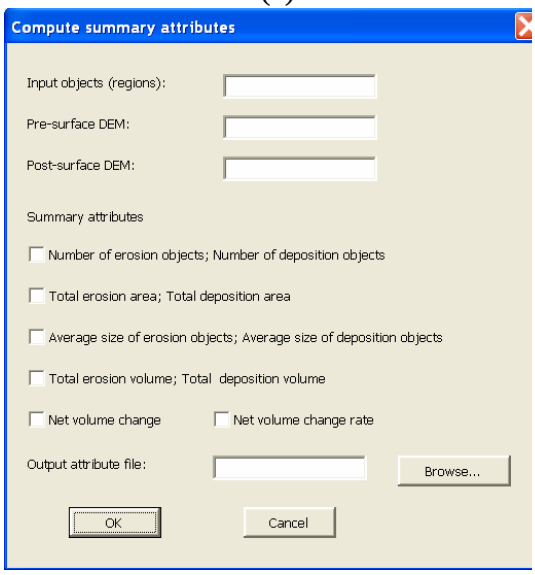

(g)

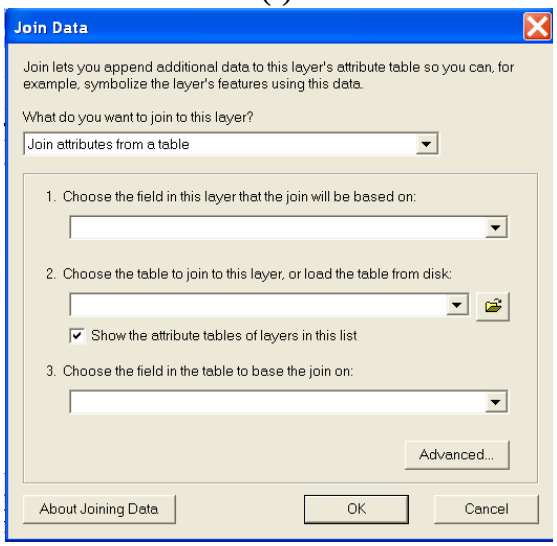

(h)

Figure 5.5 (Continued)

6 CASE STUDIES

To demonstrate the utility and effectiveness of algorithms, this section applies the analysis method and software tool to case study areas. The cross-shore profile change analysis method is applied to a case study area located at southern Monterey Bay, California, and the coastal morphology change analysis method is applied to a case study area located on Assateague Island, Maryland.

6.1 A case study for beach profile feature extraction and change analysis

The automated algorithm for beach profile feature extraction and change analysis is applied to a case study area located at southern Monterey Bay, California, in the Pacific coast of the US (Figure 6.1). Southern Monterey Bay is characterized by a sandy shoreline backed by extensive bluffs. Beach sands are originated from the sediments of Salinas River and blown onshore by wind. It is a characteristic erosive coastline and on average, the dunes south of the Salinas River are eroding at the highest rate in California (Hapke et al., 2006). Bluff erosion occurs when storm waves coincide with high tides. During the 1997-1998 El Nino winter, significant bluff recessions were observed, as a result of anomalously high tides and high wave energy (Thornton et al., 2006).

Figure 6.1 The geographical settings of Marina, southern Monterey Bay, California

6.1.1 LiDAR data preprocessing

Two successive LiDAR surveys are used in this case study. The first survey was conducted on October 13th, 1997, and the second was on April 18th, 1998. Both two LiDAR surveys were acquired by NASA Airborne Topographic Mapper (ATM) LiDAR system through the NOAA/USGS/NASA Airborne LiDAR Assessment of Coastal Erosion (ALACE) Project. The raw LiDAR measurements have a vertical accuracy within 0.15 m and a horizontal accuracy around 0.8 m. The raw LiDAR measurement points were interpolated into Digital Elevation Model (DEM) grid at 1 m spatial resolution.

Two LiDAR DEMs were projected to the UTM (zone 10) coordinate system and horizontally referenced to North American Datum of 1983 (NAD83). The vertical datum is North American Vertical Datum of 1988 (NAVD88). The overlapping areas were extracted from two LiDAR surveys to conduct change analysis. The hillshading images were created for both DEMs to provide a three-dimensional view of the topography, which could also facilitate the horizontal registration and vertical calibration. The vertical calibration was conducted by using the asphalt parking lot behind Stillwell Hall as a pseudo invariant feature (Figure 6.2).

Figure 6.2 Stillwell Hall, Marina, CA. Photograph copyright © 2002 Kenneth & Gabrielle Adelman (http://www.californiacoastline.org/)

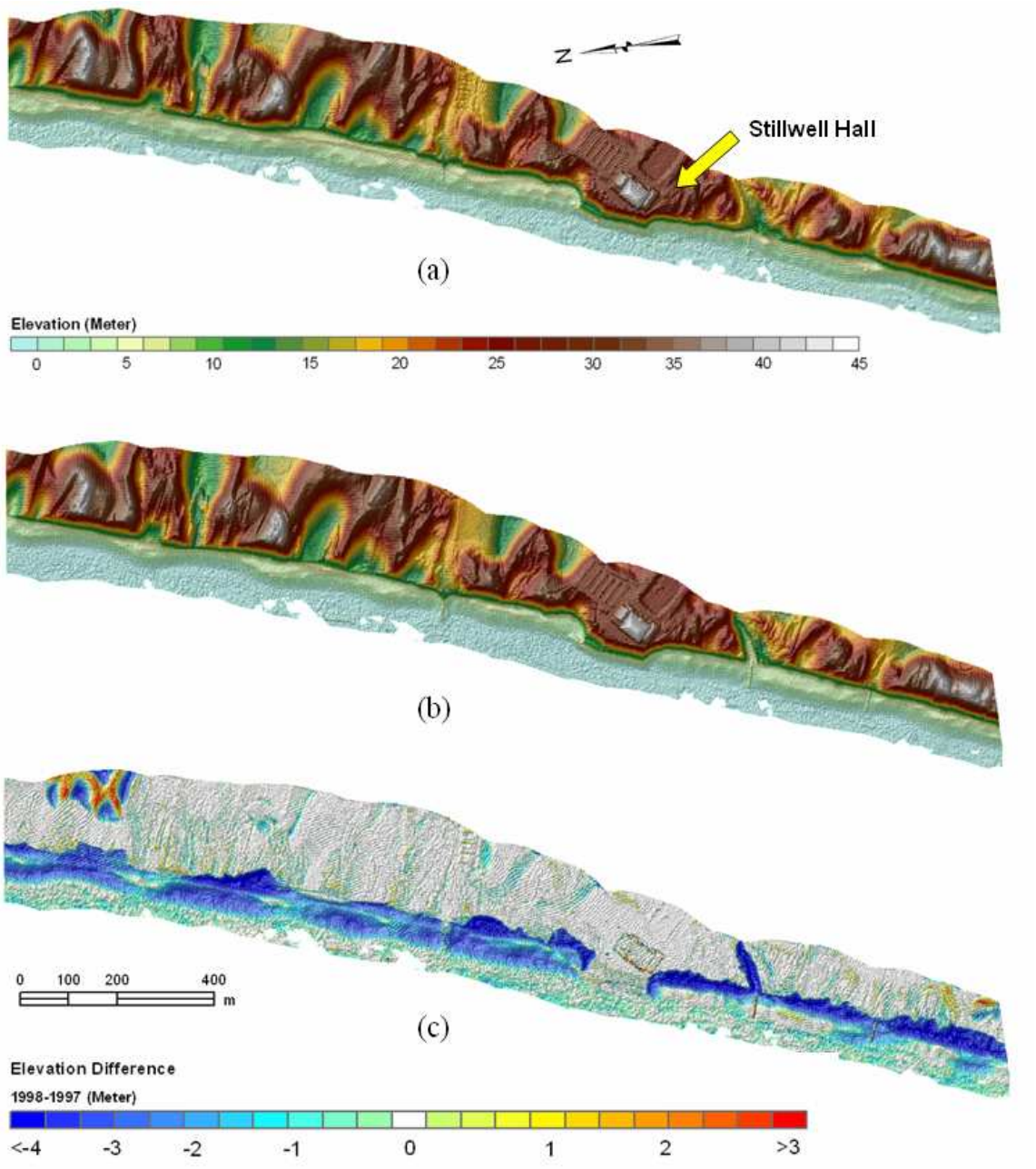

Figure 6.3 LiDAR DEMs and the elevation difference grid. (a) DEM acquired in 1997; (b) DEM acquired in 1998; and (c) Cell-by-cell elevation changes during 1997-1998

6.1.2 Beach profile feature extraction and change analysis

The elevation change grid was created by subtracting the 1997 LiDAR DEM (Figure 6.3a) from the 1998 LiDAR DEM (Figure 6.3b) as in Equation (6.1):

$$\Delta z_{ij} = z_{ij}^{1998} - z_{ij}^{1997} \tag{6.1}$$

where z_{ij}^{1998} and z_{ij}^{1997} are the elevation measurements for the cell (i, j) respectively at the year 1998 and the year 1997, and Δz_{ij} is the elevation difference for the cell (i, j).

Figure 6.3c shows the spatial pattern of elevation changes. Given a vertical accuracy of 0.15m, the random error of elevation differences could be as large as σ_d = 0.21m ($\sqrt{2} \times 0.15$ m). In Figure 6.3c, the absolute elevation change less than 0.42m is represented in white color. Blue-green color represents a decrease in elevation and red-yellow color represents an increase in elevation. Strong erosion occurred both in the bluff face and beach zone. Also, on the south side of Stillwell Hall, a breach was opened in the coastal bluff.

Bluff recession can be better measured and analyzed from the cross-shore profiles. To determine the location of beach transects, the shoreline was extracted based on a monthly mean high water level of 1.417 m in April 1998 (Figure 6.4). The beach transects were generated normal to shoreline at a regular interval of 10m, with a uniform width of 150 m (Figure 6.5).

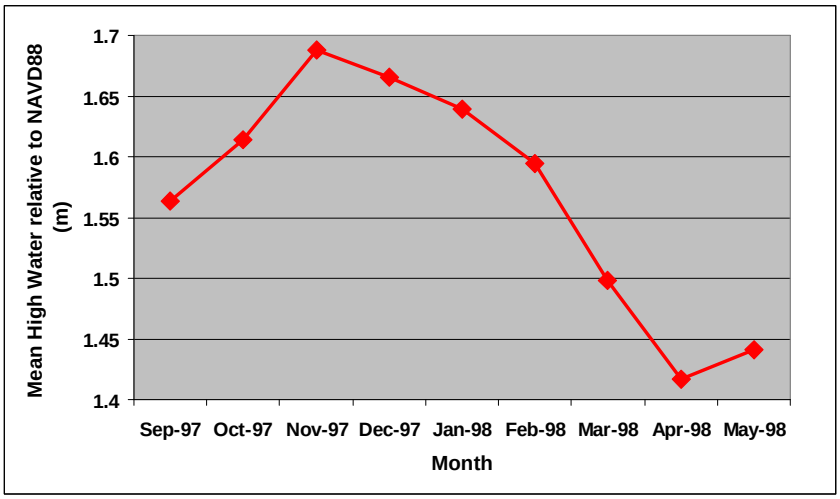

Figure 6.4 Monthly mean high water level relative to NAVD88 during 1997-1998 winter (Source: NOAA historical water level data for NOS station 9413450 – Monterey, CA. http://tidesandcurrents.noaa.gov)

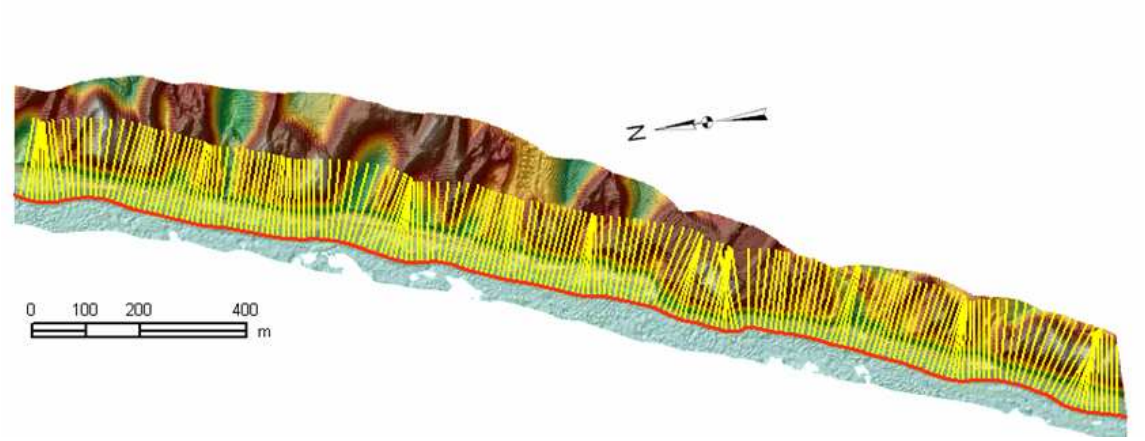

Figure 6.5 Beach transects generated along the shoreline

After several experiments, the standard deviation of Gaussian filter to smooth the beach profile was determined as $\sigma = 2$. Based on the calculation of slope and curvature, the feature points including bluff crest, bluff toe, and beach berm crest were identified for each beach profile (Figure 6.6a). The contextual information was incorporated to improve the feature point identification (Figure 6.6b). By incorporating the information

from neighboring profiles, most errors in the feature extraction results were corrected (Figure 6.7a, Figure 6.7b, and Figure 6.7c). However, in some specific areas, a few feature points were still problematic, which may need to be manually edited or deleted (Figure 6.7d and Figure 6.7e).

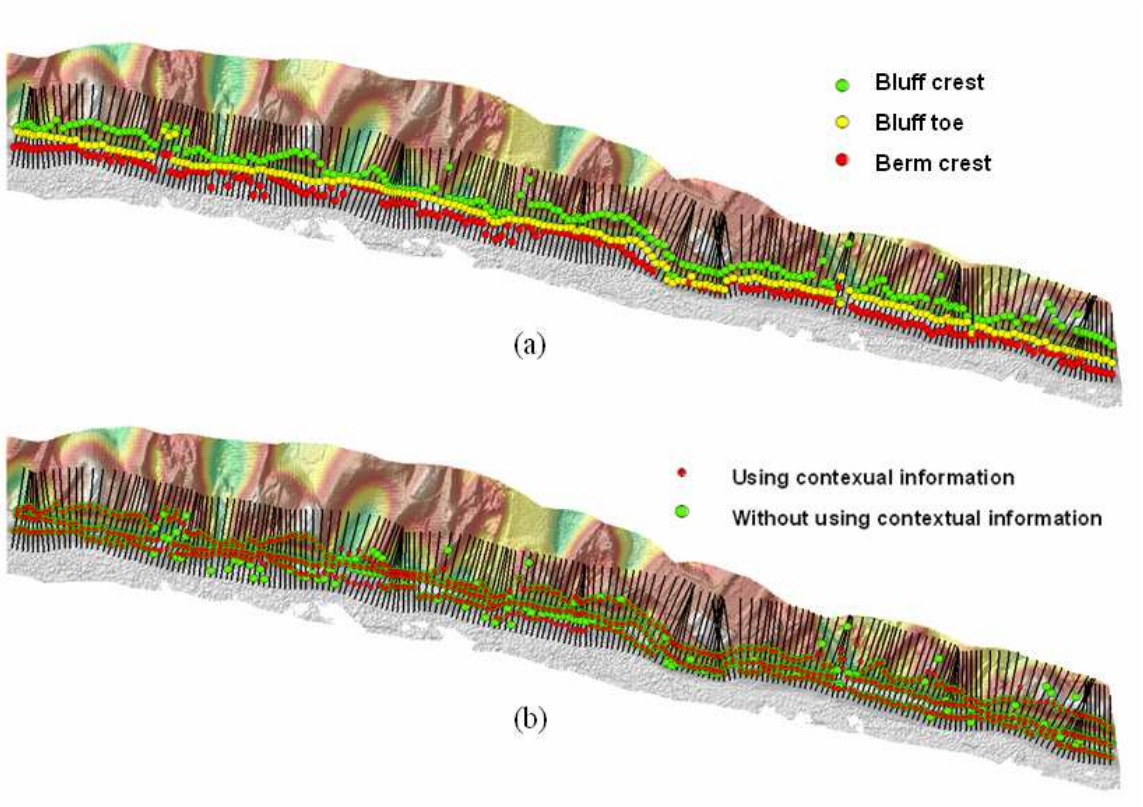

Figure 6.6 Beach feature extraction from spring 1998 LiDAR data. (a) Feature points identified without using contextual information; (b) Comparison between the feature points identified with and without using contextual information

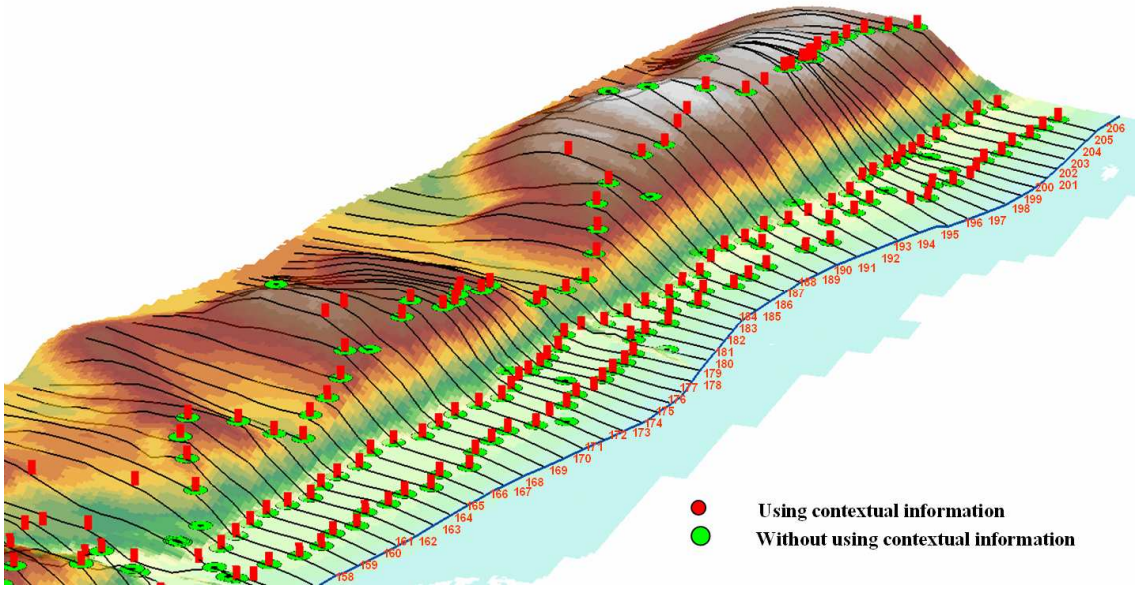

(a)

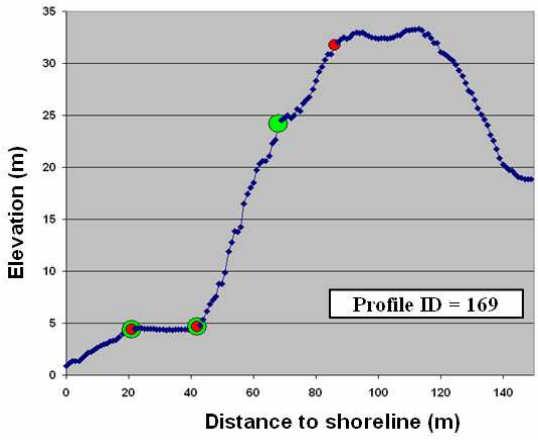

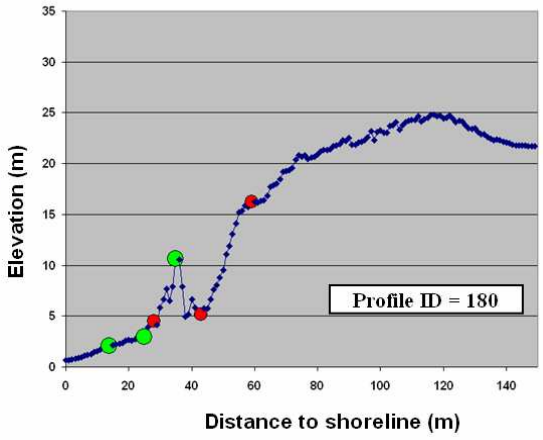

(b) (c)

Figure 6.7 Comparison between the feature points identified with and without using contextual information (Spring 1998; Profile 158 – 206). (a) 3D view of feature points comparison; (b) Profile 169; (c) Profile 180; (d) Profile 30; (e) Profile 120

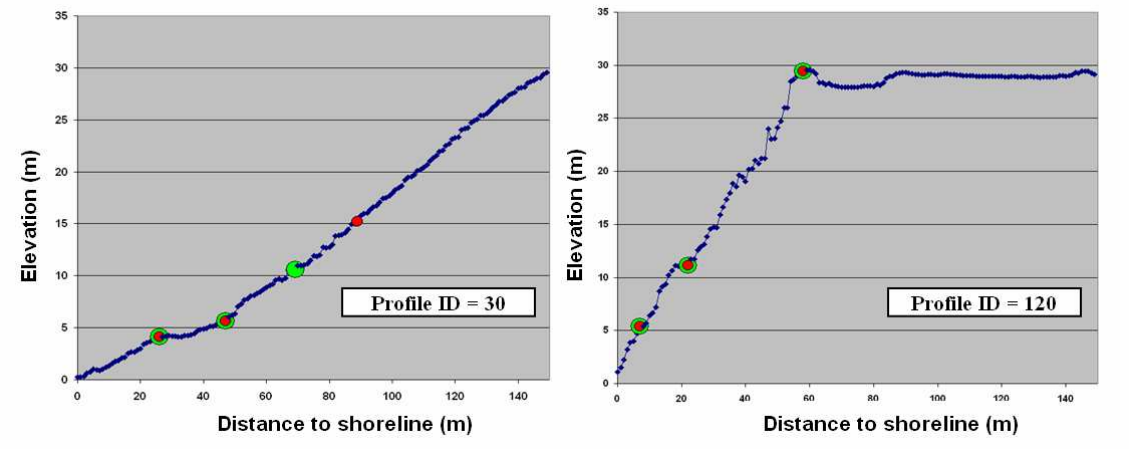

(d) (e)

Figure 6.7 (Continued)

For the 2.1km coastal stretch of the case study area, the algorithms were applied to extract features from each of the 206 profiles for both years (Figure 6.8). As noticed by Thornton et al. (2006), the dune crest in 1998 is relative easy to identify because of the severe erosion during the winter, but the identification of dune crest in fall 1997 is relative difficult because the erosion has not occurred and the edge has been rounded by wind and rain. Also, the dune toe is easier to be identified in spring 1998 because winter waves have cleared off the beach waste, while in fall 1997 the toe has been rounded. For most profiles, the dune crest and toe, as well as the berm crest can be located at reasonable positions. While in some cases, the feature points, especially the berm crest, cannot be clearly identified even by visual interpretation. For each year of study, the distance and elevation of dune crest, dune toe, and berm crest, the slope and height of

dune face, as well as the slope and width of berm were calculated for each individual profile (A portion of results are illustrated in Figure 6.9 and Table 6.1).

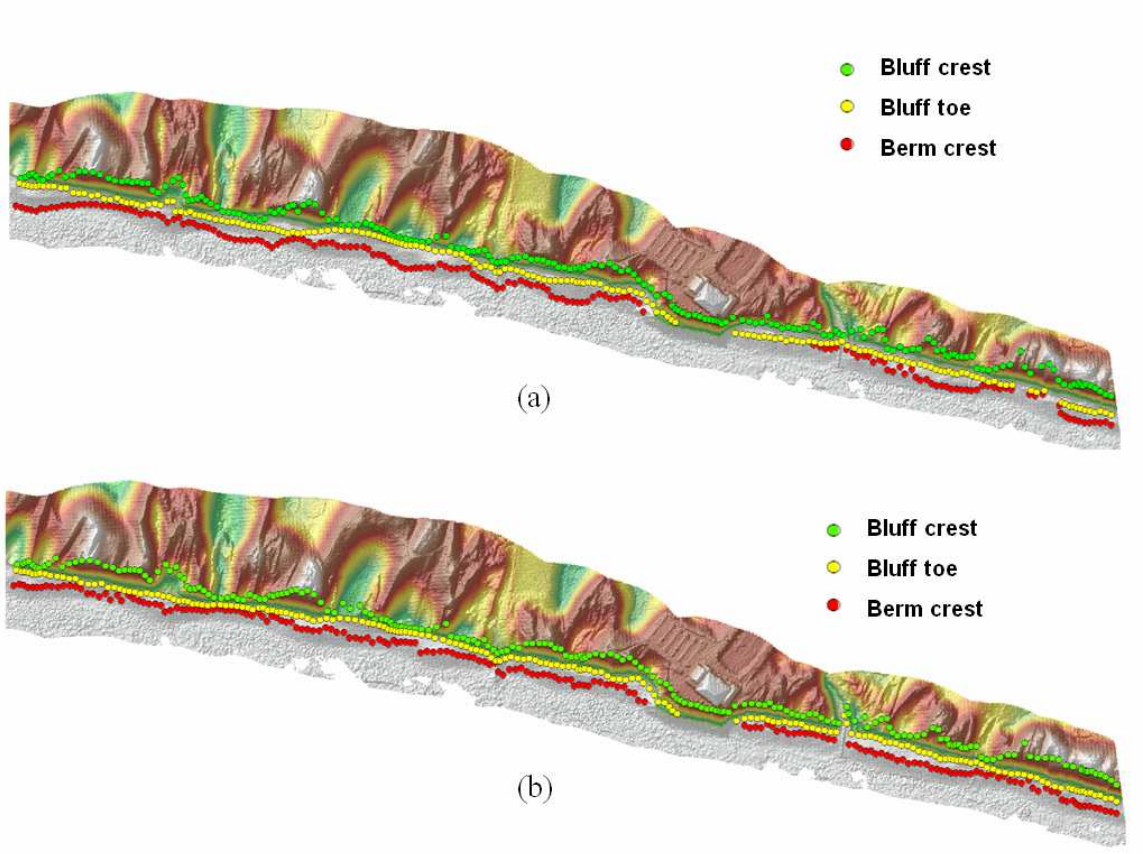

Figure 6.8 Beach feature extraction from fall 1997 and spring 1998 LiDAR data. (a) Feature points identified for fall 1997 LiDAR data; (b) Feature points identified for spring 1998 LiDAR data

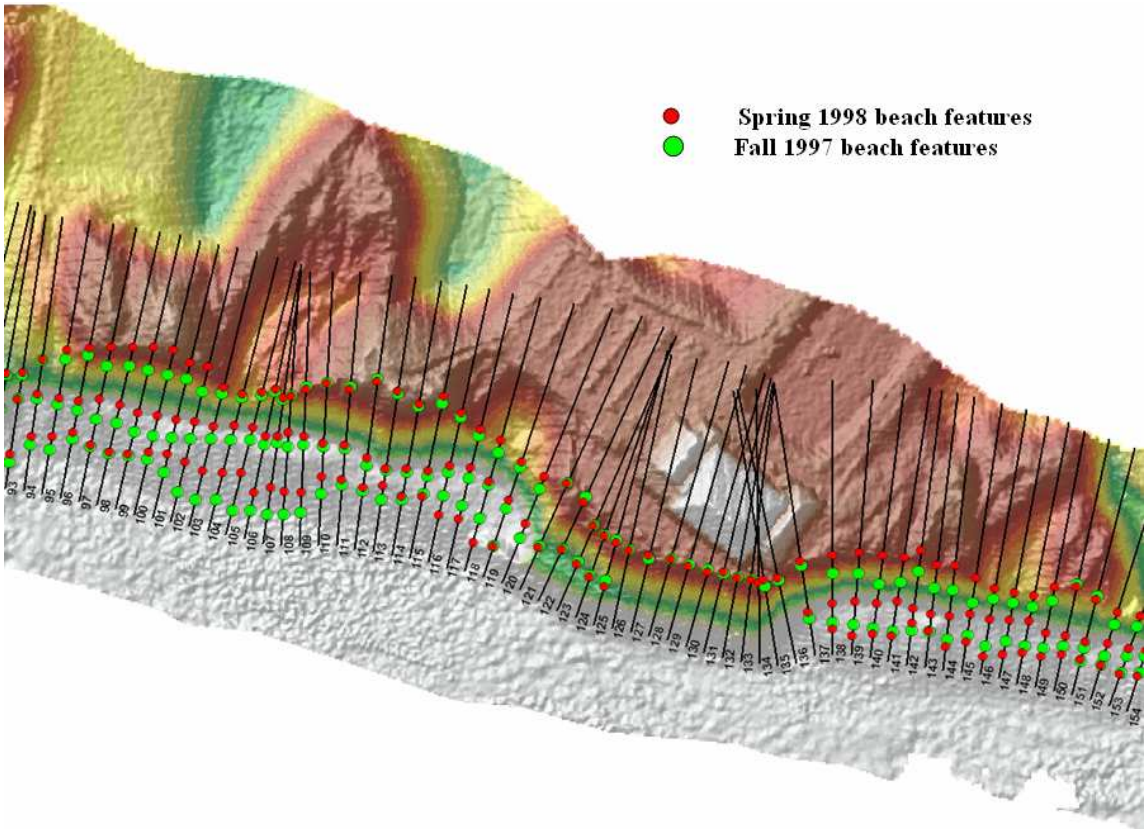

Figure 6.9 Beach feature extraction from fall 1997 and spring 1998 LiDAR data (Profile 93 - 152)

Table 6.1 Beach profile attributes derived for (a) year 1997; (b) year 1998; and (c) changes

(a) Year 1997										
ID	**Berm crest distance (m)**	**Berm crest elevation (m)**	**Bluff crest distance (m)**	**Bluff crest elevation (m)**	**Bluff toe distance (m)**	**Bluff toe elevation (m)**	**Bluff height (m)**	**Bluff slope**	**Berm width (m)**	**Berm slope**
94	24	4.7	74	18.9	49	6.3	12.6	0.50	25	0.07
95	32	5.4	78	26.6	48	6.7	20.0	0.67	16	0.08
96	30	5.3	74	28.0	45	6.8	21.3	0.73	15	0.09
97	28	5.3	76	29.4	45	6.7	22.7	0.73	17	0.08
98	29	5.3	76	29.8	42	5.9	23.9	0.70	13	0.05
99	30	5.3	76	29.7	43	5.9	23.8	0.72	13	0.05
100	25	4.6	76	28.7	44	5.7	23.0	0.72	19	0.06
101	16	3.8	71	25.9	45	6.0	19.9	0.77	29	0.07
102	14	3.4	72	24.1	47	6.1	18.0	0.72	33	0.08
103	17	3.4	73	20.6	50	6.1	14.4	0.63	33	0.08
104	13	3.5	76	21.0	52	6.0	15.0	0.62	39	0.06

Table 6.1 (Continued)

(b) Year 1998										
ID	**Berm crest distance (m)**	**Berm crest elevation (m)**	**Bluff crest distance (m)**	**Bluff crest elevation (m)**	**Bluff toe distance (m)**	**Bluff toe elevation (m)**	**Bluff height (m)**	**Bluff slope**	**Berm width (m)**	**Berm slope**
94	32	1.9	79	20.5	53	4.8	15.8	0.61	21	0.14
95	36	2.5	82	27.4	53	5.9	21.5	0.74	17	0.20
96	31	2.2	85	29.2	56	5.1	24.1	0.83	25	0.12
97	29	1.8	87	30.7	55	5.2	25.5	0.80	26	0.13
98	30	2.6	89	31.6	53	5.1	26.5	0.74	23	0.11
99	34	3.4	90	32.5	54	5.2	27.3	0.76	20	0.09
100	35	4.0	85	29.9	54	5.3	24.6	0.79	19	0.07
101	33	3.5	85	27.7	55	5.5	22.2	0.74	22	0.09
102	30	3.0	76	24.8	54	5.3	19.6	0.89	24	0.10
103	32	3.1	75	20.4	58	6.0	14.5	0.85	26	0.11
104	34	3.1	78	21.3	59	5.5	15.9	0.84	25	0.10

(c) Change (Year 1998 – Year 1997)											
ID	**Berm crest distance (m)**	**Berm crest elevation (m)**	**Bluff crest distance (m)**	**Bluff crest elevation (m)**	**Bluff toe distance (m)**	**Bluff toe elevation (m)**	**Bluff height (m)**	**Bluff slope**	**Berm width (m)**	**Berm slope**	**Bluff volume (m^3)**
94	8	-2.8	5	1.6	4	-1.5	3.2	0.10	-4	0.07	-46.8
95	4	-2.9	4	0.8	5	-0.8	1.6	0.08	1	0.12	-130.5
96	1	-3.2	11	1.2	11	-1.7	2.8	0.10	10	0.02	-233.2
97	1	-3.5	11	1.3	10	-1.5	2.8	0.07	9	0.05	-261.7
98	1	-2.7	13	1.9	11	-0.8	2.7	0.03	10	0.06	-308.3
99	4	-1.9	14	2.9	11	-0.6	3.5	0.04	7	0.05	-306.8
100	10	-0.5	9	1.2	10	-0.4	1.6	0.07	0	0.01	-260.2
101	17	-0.3	14	1.8	10	-0.5	2.3	-0.03	-7	0.02	-212.3
102	16	-0.5	4	0.8	7	-0.8	1.6	0.17	-9	0.01	-119.5
103	15	-0.3	2	-0.1	8	-0.2	0.0	0.22	-7	0.03	-82.2
104	21	-0.4	2	0.4	7	-0.6	0.9	0.21	-14	0.03	-70.7

The bluff rise up to 39.1m within the 2.1km coast in Fort Ord and Marina area and the seaward face of the bluffs is an eroding bluff. A 200m long rock rubble seawall was constructed to protect Stillwell Hall in 1978 and then fixed in 1985 to stop erosion (Figure 6.2). In 1997, along the whole coastline within the study area, the bluff top elevation varies from 10.5m to 39.1m and the bluff height varies from 3.3m to 30.0m.

Within the coastal area nearby Stillwell Hall, although the algorithms identified bluff toes at some profiles across the seawall, part of them were deleted manually because they are not supposed to be located on the seawall. Most part of the seawall plunges directly into the ocean without beach at the foot of the wall. However, some bluff toe points identified on the seawall were kept because they indicate the height of riprap that was used to protect the base of seawalls (Figure 6.10). In this area nearby seawall, the bluff top elevation varies from 16.0m to 33.4m and the bluff height varies from 10.2m to 27.5m (Figure 6.11 and Figure 6.12). The elevation of the bluff toe is relatively consistent.

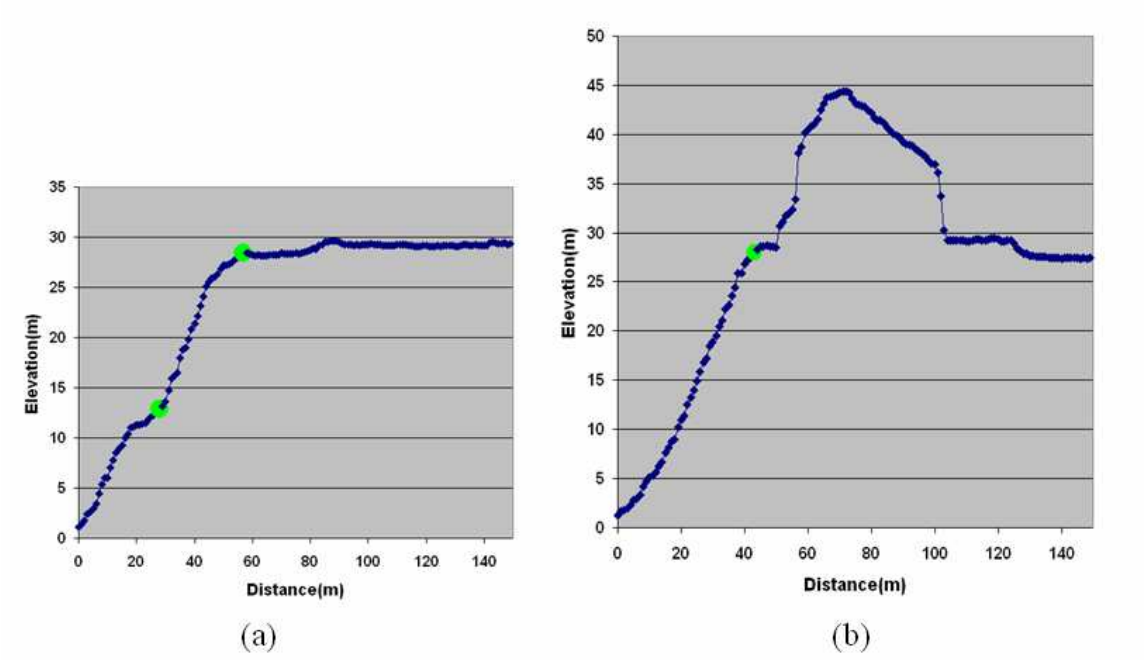

Figure 6.10 Profiles across seawall (fall 1997). (a) Profile 121: bluff toe was identified by the algorithms on the top of the riprap; (b) Profile 130: bluff toe was not identified by the algorithms

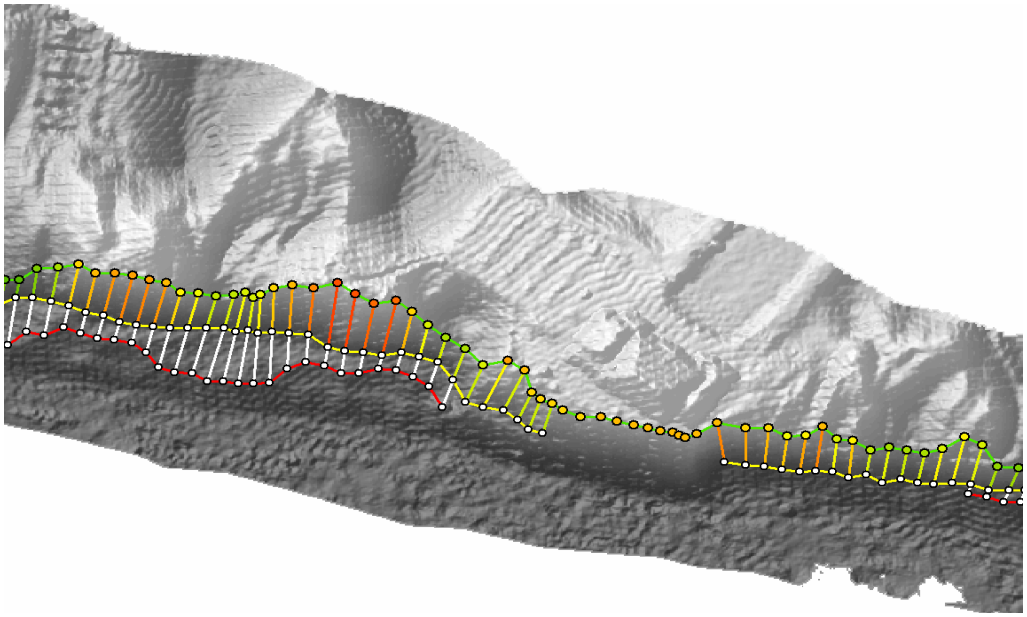

(a)

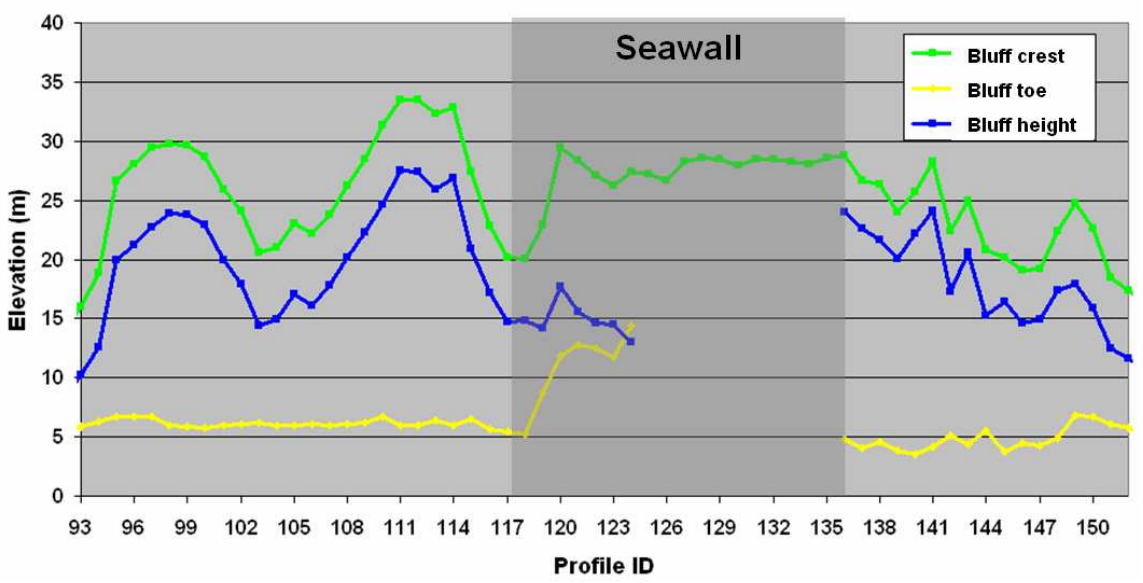

(b)

Figure 6.11 Variations of bluff crest elevation, bluff toe elevation, and bluff height along shoreline in the area nearby seawall (fall 1997)

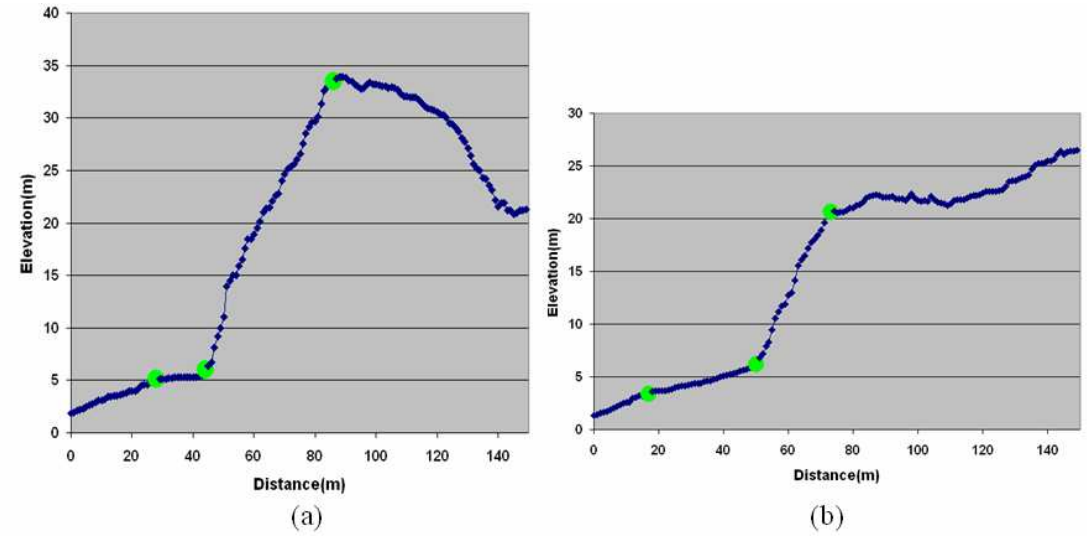

Figure 6.12 Example of high bluff and low bluff. (a) Example of high bluff: profile 112; (b) Example of low bluff: profile 103

After the beach profile feature points were extracted for two successive LiDAR surveys, the change information for the selected attributes was derived for each profile. From the profiles that across Stillwell Hall and the seawall in front of it, the accuracy and repeatability of the LiDAR data are demonstrated (Figure 6.13). The spatial variations of the change attributes can be inspected along the shoreline. The bluff volumetric change was calculated based on the horizontal positions of pre-El Nino bluff toe and the horizontal positions of pre- or post-El Nino bluff crest, whichever is further landward. The beach volumetric change was calculated based on the shoreline position and the horizontal position of pre-El Nino bluff toe.

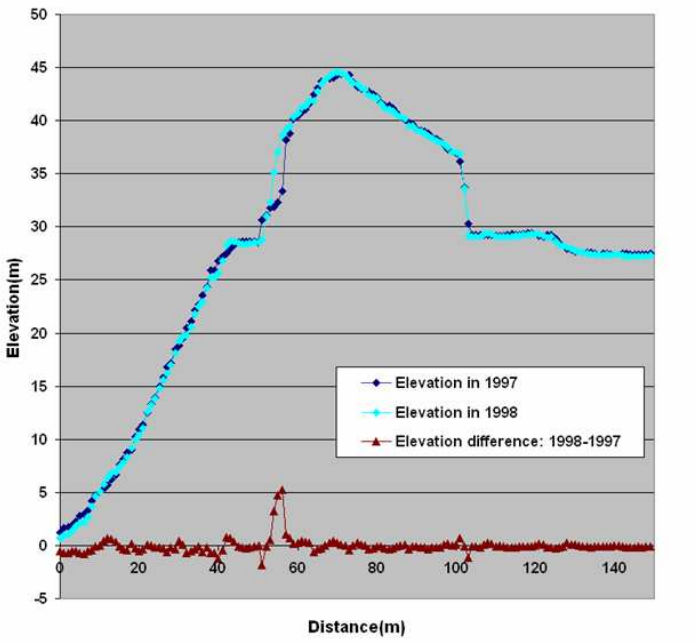

Figure 6.13 Elevation change for Profile 130 (across Stillwell Hall)

The bluff crest recession is the horizontal difference in bluff crests between two surveys, which varies alongshore from -7m to 21m after removing the outliers (Figure 6.14). The bluff toe recession follows the similar trend as bluff crest. The large recession in this area may be explained by the concentration of wave energy at Fort Ord, as well as the storms and higher sea level during El Nino events. From the cross-shore perspective, no obvious erosion is detected for the beach profiles through the Stillwell Hall (Figure 6.13). However, the profile to the north and south of Stillwell Hall shows up to 16m bluff crest recession (Figure 6.15). The bluff toe elevations generally decreased and the bluff crest elevations generally increased (Figure 6.16). The mean toe elevation changes from an average of 6.6 m in 1997 to 5.4m in 1998. The height of bluff toe indicates that the bluff erosion would only occur when the storm waves coincide with high tides.

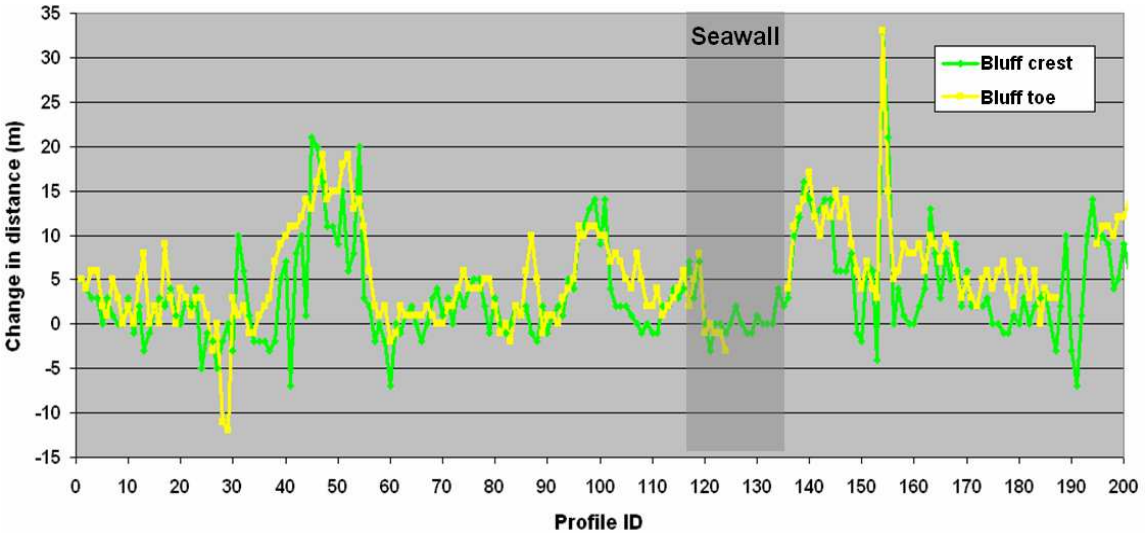

Figure 6.14 Change of bluff crest and bluff toe's distance to the shoreline (year 1998 – year 1997)

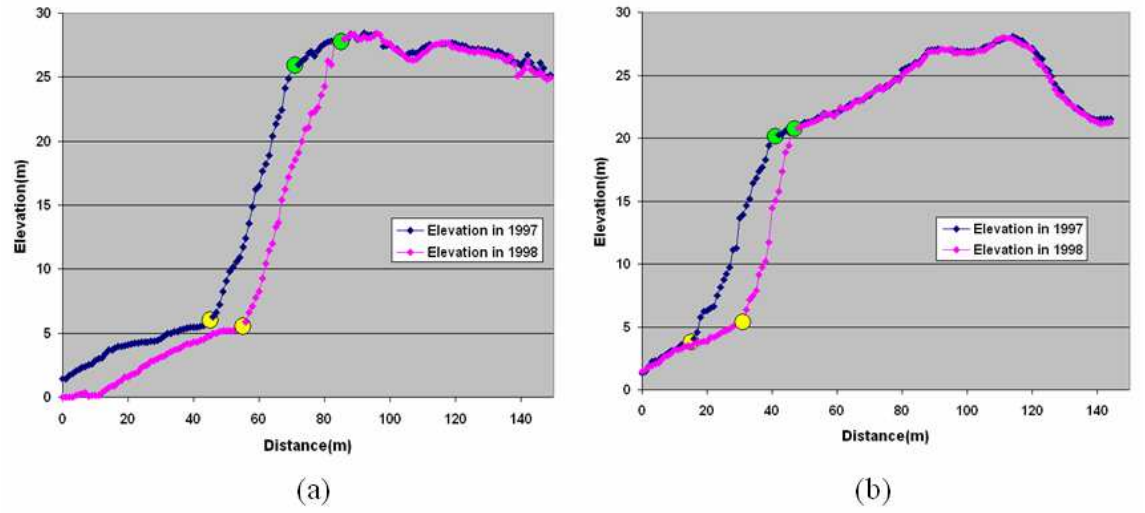

Figure 6.15 Bluff crest and toe recession next to the seawall. (a) Profile101: 200m north to the seawall; (b) Profile139: 50m south to the seawall

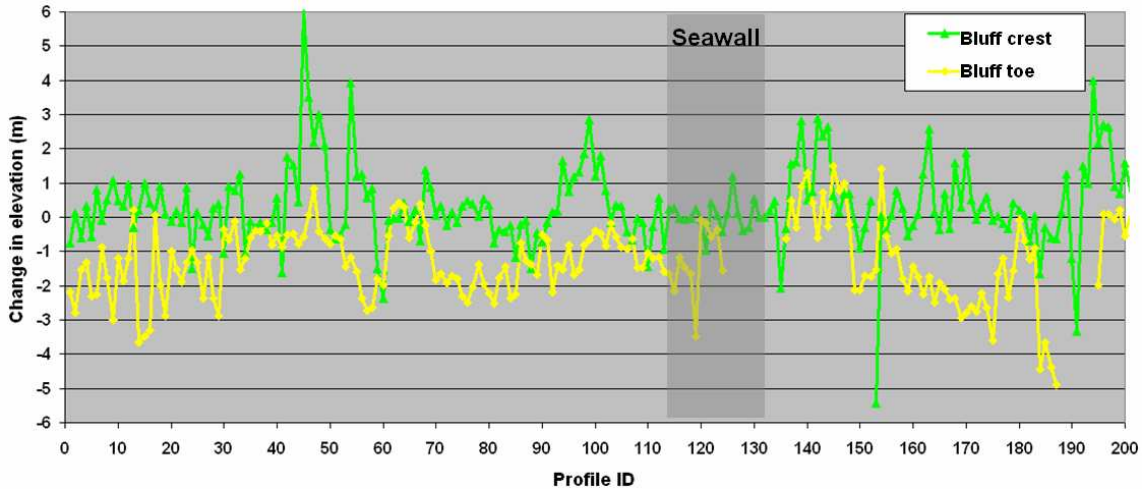

Figure 6.16 Change of bluff crest and bluff toe's elevation (year 1998 – year 1997)

Along the shoreline, the bluff volume change range from an accretion of 3.6 m^3 per meter of shoreline, which is small enough to be considered within error threshold, to erosion up to 468 m^3 per meter of shoreline (Figure 6.17). The total volume loss is about 20910 m^3.Given the limitation of topographic LiDAR system in terms of its water penetration ability, the volume change of the beach portion is only determined above the monthly mean high water level in April 1998. Within this area, the total beach volume loss is about 13518 m^3, with much less variation along shore than the bluff volume change. The beach volume loss is mainly caused by the seasonal beach change, when sand goes offshore in the winter, but there is still some permanent loss to the offshore.

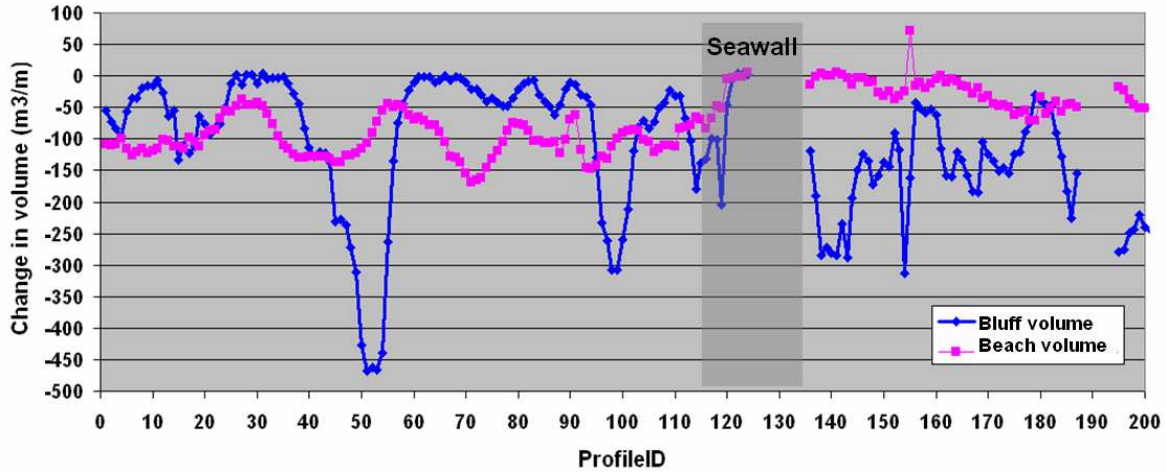

Figure 6.17 Change in bluff and beach volume (year 1998 – year 1997)

6.2 A case study for object-based morphological and volumetric change analysis

The object-based coastal morphological and volumetric change analysis method is applied to a case study area located at Assateague Island, Maryland, in the central Atlantic coast of the US (Figure 6.18). Assateague Island is a barrier island built as wave action piles up sand from the ocean floor, and has been constantly reshaped by the currents, winds, and tides. Barrier islands are characteristic depositional coastal landforms that are quite common all over the world, lying offshore of more than 10% of the world's coastlines. They are most extensive along the east coast of the US, extending from New England down the Atlantic Coast, and south to the Gulf of Mexico.

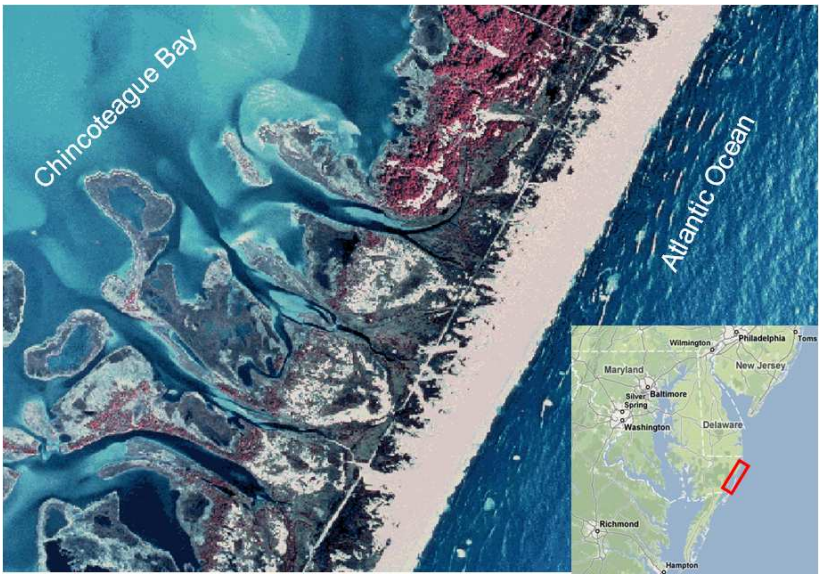

Figure 6.18 The geographical settings of Whittington Point of Assateague Island, Maryland

6.2.1 LiDAR data preprocessing

The analysis on morphological and volumetric change is performed based on two successive LiDAR surveys – the first survey was conducted on September 15th, 1997, and the second was on Septmber 20th, 2000. Both two LiDAR surveys were acquired by NASA's Airborne Topographic Mapper (ATM) LiDAR system through the NOAA/USGS/NASA Airborne LiDAR Assessment of Coastal Erosion (ALACE) Project. The raw LiDAR measurements have a vertical accuracy within 0.15m and a horizontal accuracy around 0.8m. The raw LiDAR points were interpolated into Digital Elevation Model (DEM) at 1m spatial resolution.

Two LiDAR DEMs were projected to the UTM (zone 18) coordinate system and horizontally referenced to North American Datum of 1983 (NAD83). The vertical datum is North American Vertical Datum of 1988 (NAVD88). The overlapping areas were

extracted from two LiDAR surveys to conduct change analysis. The hillshading images were created for both DEMs using common gray scale to provide a three-dimensional perspective of the topography, which could also facilitate the horizontal registration and vertical calibration (Figure 6.19a and Figure 6.19b). The vertical calibration was conducted by using the highway as invariant feature. After vertical adjustment, a 3×3 median filter was applied to both 1997 and 2000 LiDAR DEMs to reduce the random errors.

6.2.2 Morphological and volumetric change analysis

The elevation change grid was created by subtracting the 1997 LiDAR DEM from the 2000 LiDAR DEM as in Equation (6.2):

$$\Delta z_{ij} = z_{ij}^{2000} - z_{ij}^{1997} \tag{6.2}$$

where z_{ij}^{2000} and z_{ij}^{1997} are the elevation measurements for the cell (i, j) respectively at the year 2000 and the year 1997, and Δz_{ij} is the elevation difference for the cell (i, j).

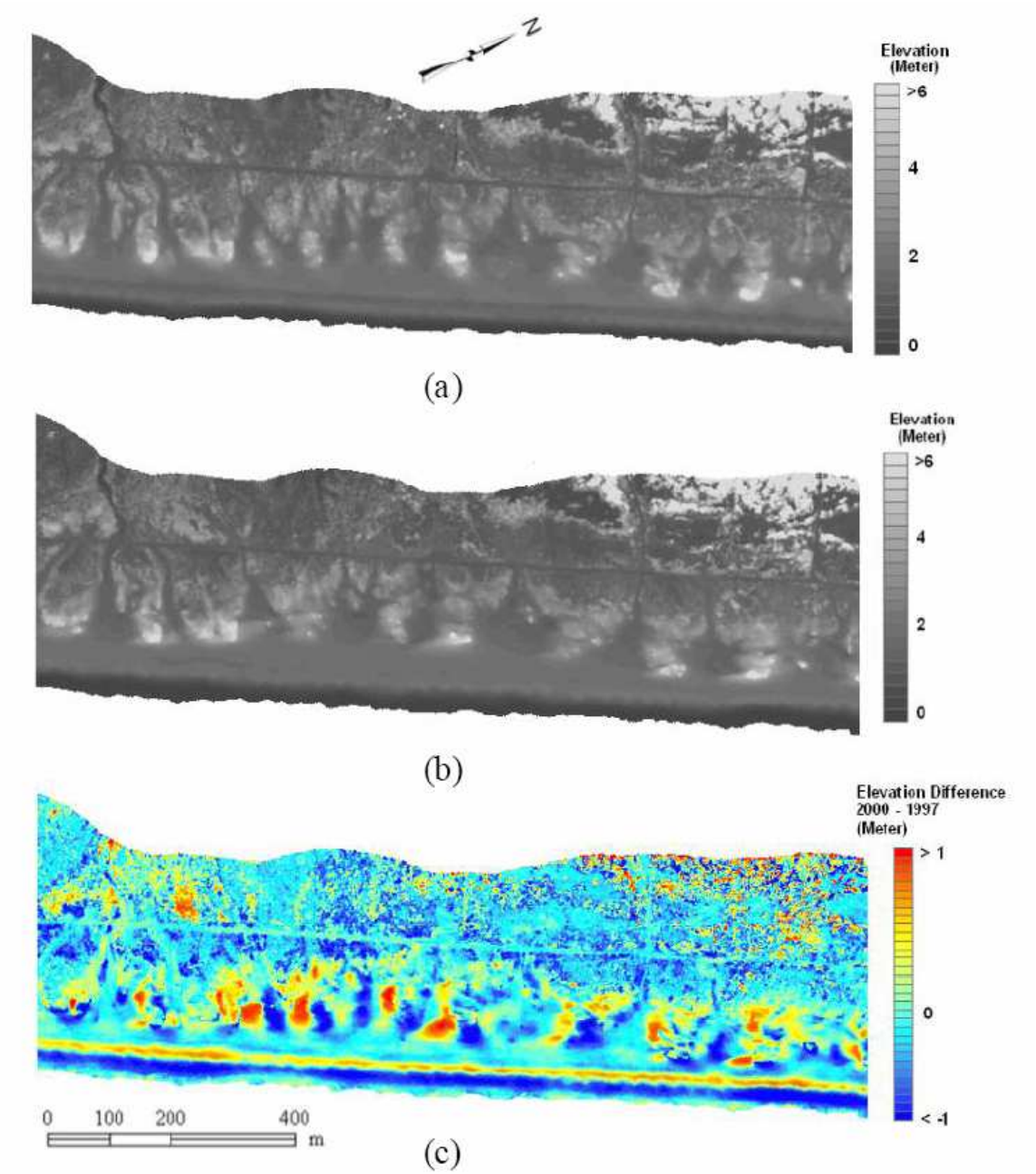

Figure 6.19 LiDAR DEMs and the elevation difference grid. (a) DEM acquired in 1997; (b) DEM acquired in 2000; and (c) Cell-by-cell elevation changes during 1997-2000

Given a vertical accuracy of 0.15 m, the random error of elevation differences could be as large as σ_d = 0.21 m ($\sqrt{2} \times 0.15\,\text{m}$). By setting the multiplicative factor k to 2.0, the criterion of assuming that elevation change has occurred is an absolute change value larger than $k\sigma_d$ = 0.42m. According to this criteria, the elevation differencing image could be reclassified into three categories: positive change (+1), negative change (-1), and unchanged (0).

$$c_{ij} = \begin{cases} 1, & if\ \Delta z_{ij} > 0.42 \\ -1, & if\ \Delta z_{ij} < -0.42 \\ 0, & if -0.42 < \Delta z_{ij} < 0.42 \end{cases} \tag{6.3}$$

where c_{ij} is the morphological change code for the grid cell (i, j).

Based on the classified elevation change imagery, the positive change and negative change objects were identified and delineated automatically (Figure 6.20). The planimatric attributes, shape attributes, surface attributes, and volumetric attributes were calculated for each individual object to perform a further classification.

The initial set of objects identified includes many change patches that were induced by factors other than erosion and deposition, such as vegetation dynamics and wave run-up. In order to focus on the sediment-induced morphological and volumetric changes, the change patches induced by various factors were classified based on the combination of selected attributes. For the change patches induced by vegetation dynamics, they commonly have irregular and rough boundaries as well as many holes and gaps, and therefore have a large fractal dimension. In addition, the changes within vegetation patches are usually discontinuous and hence have a much larger vertical

standard deviation. For the change patches induced by wave run-up, they commonly have a relatively small size. Based on these observations, three attributes were used for the classification in this case study: fractal dimension, standard deviation of vertical changes, and size. A set of criteria was defined to identify and remove change patches induced by vegetation dynamics, wave run-up, and other data noise, which includes: Fractal Dimension (D) > 1.4, or standard deviation of vertical change (Δz_{std}) > 0.6, or Size (A) < 190 m^2. The remaining objects are considered to be changes caused by erosion and deposition. Morphological operations were applied to smooth the remaining erosion and deposition objects (Figure 6.21).

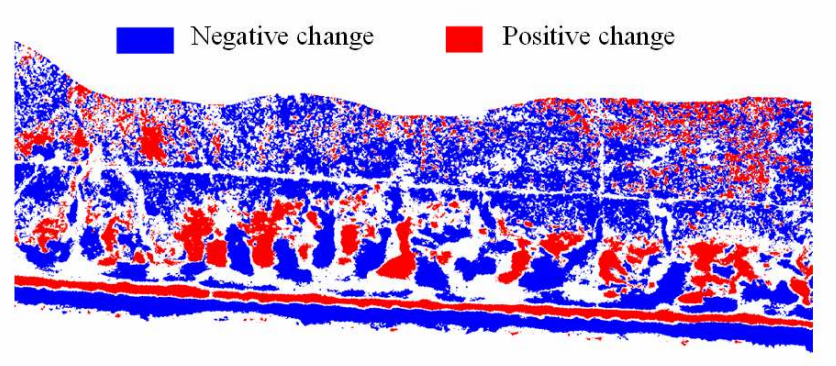

Figure 6.20 Negative change and positive change objects

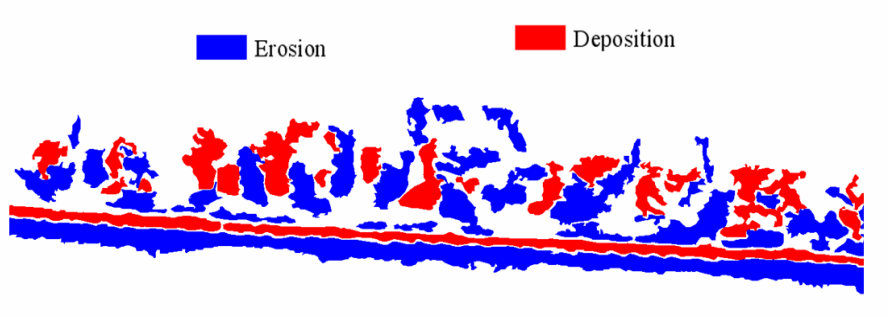

Figure 6.21 Erosion and deposition objects after smoothing

For the 1.85 km coastal stretch of the case study area, totally 34 erosion objects and 23 deposition objects were identified. All the planimetric, shape, surface, and volumetric attributes were calculated for these objects again (Figure 6.22 and Table 6.2). The minimum bounding rectangles and best-fit ellipse were created for each object to generalize the shape (Figure 6.23). The summary statistics were calculated to describe the total erosion, deposition, and net volume change in this area.

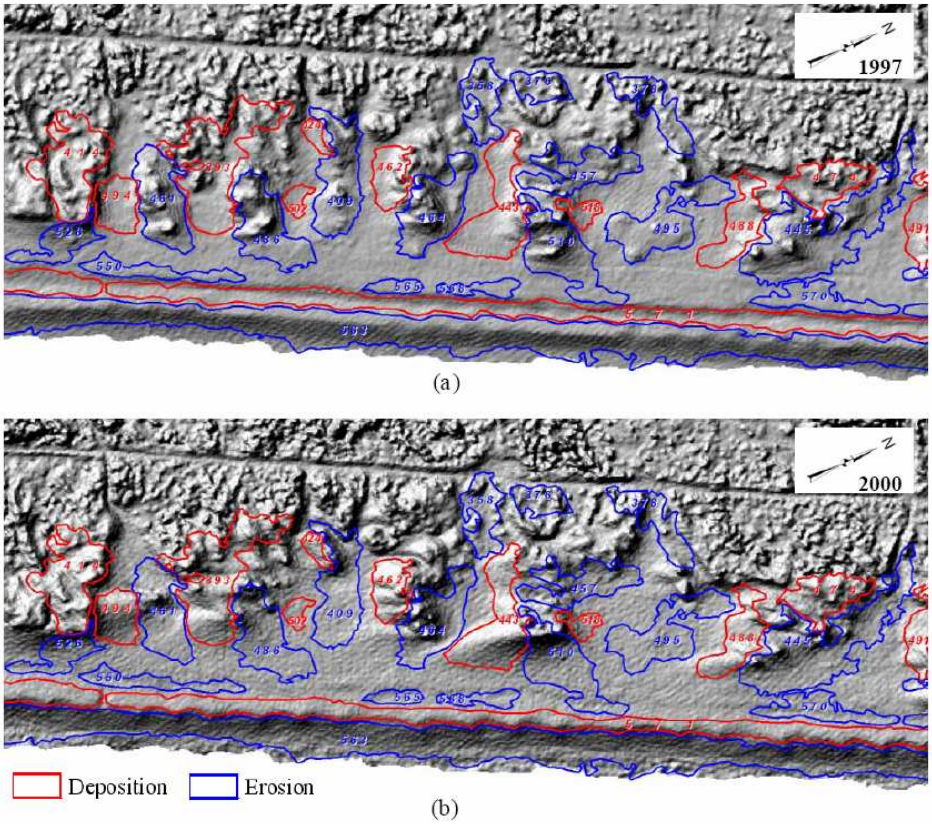

Figure 6.22 Erosion and deposition objects overlaid on the hill-shaded relief images. (a) Relief image derived from 1997 LiDAR data; (b) Relief image derived from 2000 LiDAR data

Table 6.2 Derived attributes values for erosion and deposition objects

ID	Type	x_c (m)	y_c (m)	p (m)	A (m^2)	MDB (m)	l (m)	w (m)	CI	ELG	ASM	ϕ
461	Erosion	481383	4212770	272	2684	16.9	95.0	39.2	0.46	2.42	0.59	170.5
486	Erosion	481469	4212750	337	2826	16.4	94.0	46.0	0.31	2.04	0.51	7.7
563	Erosion	481774	4212650	3683	41549	19.7	1847.0	35.7	0.04	51.68	0.98	62.1
510	Erosion	481712	4212720	391	3062	20.5	107.7	45.4	0.25	2.37	0.58	16.9
409	Erosion	481527	4212790	343	2938	17.0	120.6	41.1	0.31	2.94	0.66	154.4
445	Erosion	481924	4212750	794	5836	23.5	188.3	60.4	0.12	3.12	0.68	98.3
464	Erosion	481607	4212770	344	2896	17.7	96.7	48.5	0.31	1.99	0.50	123.5
378	Erosion	481789	4212840	402	1824	8.8	111.3	32.3	0.14	3.45	0.71	12.6
457	Erosion	481725	4212800	393	2190	8.7	107.7	36.3	0.18	2.97	0.66	73.2
376	Erosion	481693	4212870	153	895	6.4	50.5	25.7	0.48	1.96	0.49	54.4
358	Erosion	481646	4212850	323	1424	9.2	77.4	32.4	0.17	2.39	0.58	158.5
526	Erosion	481299	4212740	286	1344	10.5	79.7	28.5	0.21	2.80	0.64	88.4
495	Erosion	481795	4212750	407	3053	14.5	117.3	47.9	0.23	2.45	0.59	97.3
550	Erosion	481376	4212710	330	1220	6.7	153.6	14.8	0.14	10.39	0.90	60.3
565	Erosion	481575	4212700	112	449	5.5	50.2	12.7	0.45	3.96	0.75	65.2
570	Erosion	481922	4212690	329	1544	8.4	115.2	24.8	0.18	4.65	0.78	58.4
568	Erosion	481645	4212700	174	587	4.5	75.4	13.4	0.24	5.65	0.82	67.3
502	Deposition	481493	4212770	90	365	6.9	29.7	19.4	0.57	1.53	0.35	135.7
518	Deposition	481725	4212760	117	493	5.7	40.5	23.3	0.45	1.74	0.42	58.0
424	Deposition	481509	4212820	94	357	7.4	37.2	15.4	0.51	2.41	0.59	5.9
474	Deposition	481925	4212780	245	1733	10.2	73.4	38.6	0.36	1.90	0.47	81.0
488	Deposition	481853	4212750	272	1863	13.4	92.9	34.5	0.32	2.70	0.63	128.2
571	Deposition	481923	4212670	2484	14699	9.5	1329.2	16.4	0.03	81.20	0.99	62.2
547	Deposition	481156	4212710	790	5684	10.7	434.0	19.0	0.11	22.86	0.96	61.2
414	Deposition	481308	4212800	361	3297	13.4	92.6	55.7	0.32	1.66	0.40	147.8
393	Deposition	481430	4212800	668	4633	17.7	136.3	70.6	0.13	1.93	0.48	131.4
443	Deposition	481657	4212760	371	3151	18.5	124.4	52.3	0.29	2.38	0.58	140.8
462	Deposition	481570	4212790	186	1298	13.4	55.4	32.6	0.47	1.70	0.41	150.5
494	Deposition	481346	4212770	154	1407	16.4	48.9	38.0	0.75	1.29	0.22	157.3

ID	Type	D	REC	ELP	TRI	AV_EL_1	AV_EL_2	AV_EL_DIF	AV_SL_1	AV_SL_2	AV_SL_DIF	AV_AP_1
461	Erosion	1.124	0.72	0.84	0.81	2.78	1.93	-0.85	6.66	3.25	-3.41	169.5
486	Erosion	1.181	0.65	0.69	0.99	3.02	2.29	-0.73	5.20	2.88	-2.32	168.7
563	Erosion	1.187	0.63	0.64	0.94	1.09	0.37	-0.73	4.27	4.19	-0.08	180.4
510	Erosion	1.268	0.63	0.63	0.93	3.32	2.62	-0.70	5.55	3.93	-1.62	163.3
409	Erosion	1.175	0.59	0.57	0.83	2.17	1.54	-0.63	4.70	3.32	-1.38	164.1
445	Erosion	1.250	0.51	0.43	0.62	2.75	2.16	-0.59	5.01	3.86	-1.15	159.2
464	Erosion	1.230	0.62	0.62	0.90	2.75	2.18	-0.57	5.84	5.00	-0.83	155.8
378	Erosion	1.303	0.51	0.42	0.61	2.34	1.80	-0.54	8.18	6.63	-1.55	173.9
457	Erosion	1.334	0.56	0.51	0.74	2.48	2.06	-0.42	4.91	3.96	-0.96	147.7
376	Erosion	1.376	0.69	0.77	0.89	2.01	1.60	-0.41	8.02	5.94	-2.08	164.6
358	Erosion	1.258	0.57	0.52	0.76	1.65	1.26	-0.39	4.26	3.52	-0.75	173.5
526	Erosion	1.214	0.59	0.57	0.83	2.69	2.32	-0.37	4.75	4.53	-0.23	178.6
495	Erosion	1.247	0.54	0.48	0.70	1.93	1.58	-0.35	2.44	1.58	-0.86	157.2
550	Erosion	1.218	0.54	0.47	0.68	2.12	1.84	-0.28	1.17	1.23	0.06	180.3
565	Erosion	1.154	0.70	0.60	0.85	2.09	1.82	-0.28	0.91	1.15	0.24	182.4
570	Erosion	1.269	0.54	0.47	0.69	2.20	1.92	-0.28	0.91	1.20	0.29	177.1
568	Erosion	1.402	0.58	0.55	0.80	2.12	1.87	-0.24	0.79	1.11	0.31	152.8
502	Deposition	1.124	0.63	0.65	0.95	1.40	1.66	0.27	1.48	1.12	-0.35	154.6
518	Deposition	1.319	0.52	0.44	0.65	2.18	2.46	0.28	4.72	4.53	-0.19	86.6
424	Deposition	1.222	0.62	0.63	0.92	1.73	2.16	0.43	5.96	6.53	0.56	231.2
474	Deposition	1.236	0.61	0.61	0.89	2.71	3.15	0.45	5.73	5.04	-0.69	171.7
488	Deposition	1.126	0.58	0.55	0.80	1.94	2.39	0.45	3.65	3.94	0.29	258.4
571	Deposition	1.213	0.68	0.74	0.92	1.60	2.07	0.47	2.49	2.25	-0.24	174.5
547	Deposition	1.159	0.69	0.77	0.89	1.53	2.00	0.48	2.20	1.67	-0.54	173.7
414	Deposition	1.290	0.64	0.66	0.97	3.04	3.57	0.53	7.23	6.59	-0.63	199.3
393	Deposition	1.337	0.48	0.38	0.55	2.46	3.06	0.60	5.85	5.12	-0.72	182.9
443	Deposition	1.178	0.48	0.38	0.56	2.04	2.72	0.68	3.95	5.25	1.30	222.1
462	Deposition	1.141	0.72	0.84	0.81	2.14	2.97	0.84	6.46	7.62	1.16	264.0
494	Deposition	1.134	0.76	0.93	0.74	1.91	2.82	0.91	4.64	4.52	-0.12	157.8

ID	Type	AV_AP_2	AV_AP_DIF	AV_CV_1	AV_CV_2	AV_CV_DIF	Δz_{av} (m)	Δz_{max} (m)	Δz_{std} (m)	ZR (m/yr)	VOL (m^3)	VR (m^3/yr)
461	Erosion	165.3	-4.2	1.13	-1.60	-2.72	-0.85	-2.80	0.55	-0.28	-2270.15	-756.72
486	Erosion	143.6	-25.1	0.91	-1.10	-2.01	-0.73	-3.24	0.56	-0.24	-2054.76	-684.92
563	Erosion	182.6	2.2	0.56	-0.97	-1.53	-0.73	-2.06	0.38	-0.24	-30193.50	-10064.50
510	Erosion	176.0	12.7	1.39	-1.74	-3.13	-0.70	-2.70	0.58	-0.23	-2151.90	-717.30
409	Erosion	153.6	-10.5	0.46	-1.63	-2.09	-0.63	-2.21	0.36	-0.21	-1851.95	-617.32
445	Erosion	154.5	-4.7	1.26	-1.04	-2.30	-0.59	-2.63	0.39	-0.20	-3432.81	-1144.27
464	Erosion	150.4	-5.4	0.95	-1.40	-2.35	-0.57	-1.80	0.31	-0.19	-1660.90	-553.63
378	Erosion	186.9	13.0	3.43	-2.85	-6.29	-0.54	-1.71	0.27	-0.18	-990.99	-330.33
457	Erosion	144.4	-3.3	2.08	-2.07	-4.15	-0.42	-1.23	0.17	-0.14	-910.20	-303.40
376	Erosion	156.9	-7.8	3.87	-1.70	-5.58	-0.41	-1.33	0.21	-0.14	-370.02	-123.34
358	Erosion	175.3	1.8	1.39	-2.22	-3.61	-0.39	-1.12	0.18	-0.13	-559.94	-186.65
526	Erosion	176.7	-1.9	2.02	-2.37	-4.39	-0.37	-1.70	0.20	-0.12	-496.89	-165.63
495	Erosion	152.7	-4.4	0.54	-1.05	-1.59	-0.35	-1.62	0.14	-0.12	-1068.50	-356.17
550	Erosion	181.8	1.5	1.16	-1.14	-2.30	-0.28	-0.46	0.05	-0.09	-341.47	-113.82
565	Erosion	198.5	16.1	1.34	-1.10	-2.45	-0.28	-0.39	0.05	-0.09	-124.61	-41.54
570	Erosion	185.9	8.9	0.73	-0.84	-1.58	-0.28	-0.44	0.05	-0.09	-427.00	-142.33
568	Erosion	178.1	25.3	1.02	-1.54	-2.56	-0.24	-0.35	0.03	-0.08	-143.11	-47.70
502	Deposition	119.1	-35.5	-1.47	0.54	2.01	0.27	0.38	0.05	0.09	96.80	32.27
518	Deposition	73.2	-13.4	-3.61	2.70	6.30	0.28	0.63	0.06	0.09	137.66	45.89
424	Deposition	252.5	21.3	-3.10	3.24	6.35	0.43	0.77	0.15	0.14	152.64	50.88
474	Deposition	182.2	10.4	-2.77	1.69	4.46	0.45	1.07	0.17	0.15	773.20	257.73
488	Deposition	261.0	2.5	-1.87	0.84	2.71	0.45	0.96	0.16	0.15	841.34	280.45
571	Deposition	178.8	4.3	-1.40	1.67	3.07	0.47	1.00	0.16	0.16	6943.01	2314.34
547	Deposition	170.3	-3.4	-1.01	1.13	2.14	0.48	0.93	0.16	0.16	2709.12	903.04
414	Deposition	207.9	8.5	-1.08	2.23	3.31	0.53	1.87	0.25	0.18	1736.17	578.72
393	Deposition	193.0	10.1	-2.55	1.72	4.26	0.60	1.69	0.37	0.20	2774.32	924.77
443	Deposition	249.9	27.8	-1.04	1.57	2.61	0.68	1.81	0.40	0.23	2146.26	715.42
462	Deposition	264.2	0.2	-1.38	2.21	3.59	0.84	2.00	0.49	0.28	1088.06	362.69
494	Deposition	143.3	-14.5	-3.55	0.33	3.88	0.91	1.71	0.44	0.30	1285.00	428.33

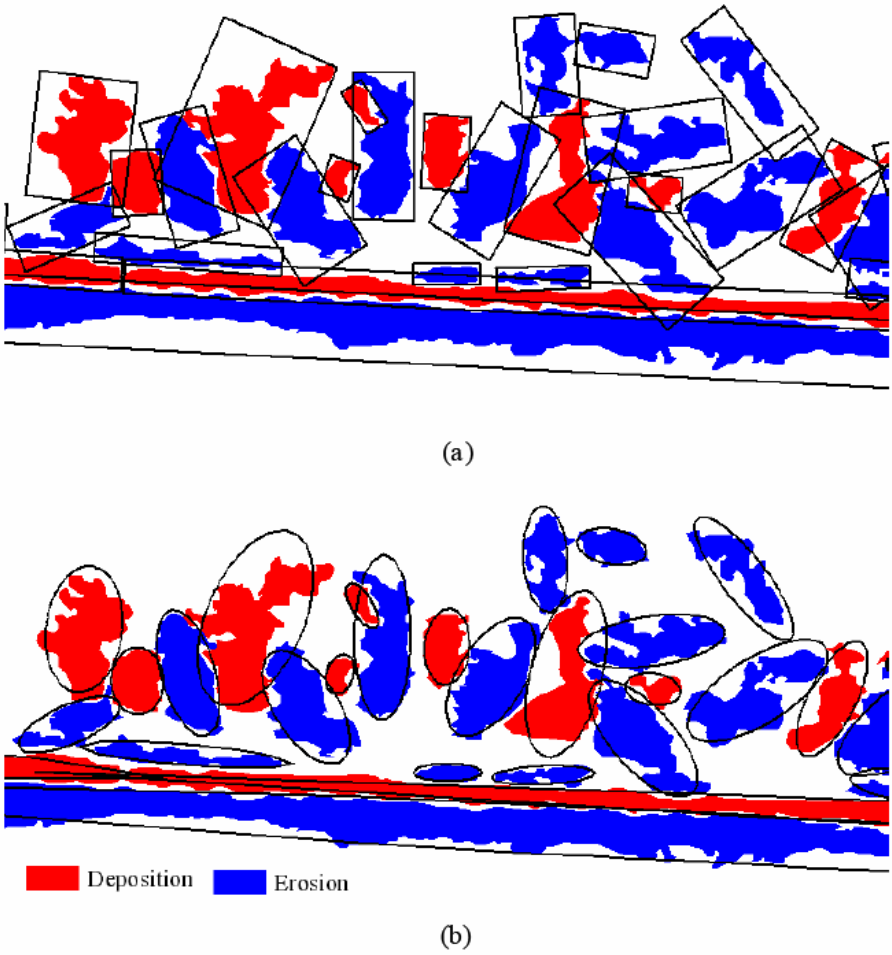

Figure 6.23 Fitted rectangles and ellipse for erosion and deposition objects. (a) Minimum bounding rectangles; (b) Best-fit ellipses

The results indicate severe erosion and morphological change along the beach zone. A continuous, long erosion zone (Object 563) (Figure 6.22 and Table 6.2) is oriented along the shoreline with an azimuth angle of 62° from the true north. This elongated erosion zone has a largest width of 35.7 m and an average erosion depth of 0.73 m. The average elevation of this zone has been reduced from 1.09 m to 0.37 m. The total erosion volume is 10,064 m^3 during 1997-2000, which is 5.448 m^3 per meter of

shoreline stretch. Erosion processes have modified the beach from its slightly convex downward shape (average curvature = 0.56) in 1997 to a concave upward shape (average curvature = -0.97) in 2000. There is landward berm migration (Figure 6.22). Along the back beach, there is a narrow deposition zone (Object 571). It was a long depression feature in 1997 (Figure 6.22a), which was almost filled by sediment in 2000 (Figure 6.22b).This zone has a maximum width of 16.4 m and an average deposition thickness of 0.47 m. The concave surface curvature (-1.40) along the depression disappeared by 2000. Both the erosion and deposition objects in the beach zone have elongated shapes and are oriented parallel to the shoreline (Table 6.2).

The results also indicate significant morphological changes in the dune zone between 1997 and 2000 (Figure 6.22), which shows a general pattern of the dune migration to the southwest direction. Plume-like features can be observed in the south side of many dunes in the 2000 hill-shaded relief image (Figure 6.22b). The significant dune movement is most likely caused by the northeast winds. These winds erode and transport sand from the dune's upwind side and deposit on the leeward side, causing downwind dune migration. Local redistribution of sand has produced many discrete erosion and deposition patches in the dune zone. As expected, erosion patches occurred on the upwind side of dunes, and deposition patches are located on the leeward side of dunes (Figure 6.22a). The erosion patches are interspersed with deposition patches. The position and shape of many dunes were changed considerably by erosion and deposition processes. Compared to the elongated erosion and deposition patches in the beach, most erosion and deposition patches in the dune zone have a more compact shape and are

oriented approximately perpendicular to the shoreline. The surface shape of all erosion patches has been changed from convex to concave (Table 6.2), while the deposition patches generally changed from concave to convex. In the dune zone, the average depth of erosion patches reaches 0.85 m (Object 461).

For the 34 erosion objects and 23 deposition objects within the 1.85 km coastal stretch, the average object size is 3221 m^2 for erosion objects and 2378 m^2 for deposition objects. The total erosion area is 109,506 m^2, and the total erosion volume is estimated to be 66,594 m^3. The total deposition area is 54,699 m^2, and the total deposition volume is estimated to be 28,223 m^3. The net erosion volume is 38,371 m^3. The normalized annual net erosion volume rate is 6.9 m^3 per meter of the shoreline stretch for the case study area. The localized information could be useful for measuring, understanding and predicting coastal morphological changes and designing future erosion control projects, such as beach nourishments and dune management.

7 CONCLUSIONS

Compared to traditional ground survey and photogrammetry techniques, airborne LiDAR remote sensing technology provides a much more cost-effective, efficient means of collecting coastal topography information. This research has developed an analytical framework to extract information and knowledge from the dense datasets acquired by LiDAR surveys, which converts a large volume of raw data into meaningful and organized information that is ready to be used in a variety of studies related to coastal topography.

This research has developed an analytical framework for extracting coastal morphology information. A set of algorithms and tools have been developed for automated extraction of coastal morphological change information from LiDAR data. The methodological contributions of this research include a set of algorithms for automated beach profile feature extraction and change analysis, and an object-based approach for spatial pattern analysis of morphological and volumetric change. The algorithms and tools for automated beach profile feature extraction and change analysis provides the cross-shore view to understand coastal morphological changes. The algorithms and tools provide more efficient means for identifying morphological features and deriving morphological attributes in a large geographic area. The beach profile features and the spatial patterns of the related changes can be visualized and analyzed along the shoreline. The representation of profiles as routes and important features as point events also facilitates the analysis in conjunction with other GIS data

for exploring the causes and impacts of the morphological and volumetric changes in the cross-shore direction.

The object-based methods for morphological and volumetric change analysis provides an explicit object representation of erosion and deposition patches, which makes it easy to localize attributes about individual erosion or deposition hot spots and to analyze the spatial pattern of morphological changes. The comprehensive quantitative information about each individual change object could facilitate the classification of changes induced by various mechanisms, as well as support a better understanding of the characteristics of morphological changes caused by erosion and deposition. The representation of erosion and deposition patches as polygonal objects could also facilitates the analysis in conjunction with other GIS data for exploring the causes and impacts of the morphological and volumetric changes.

Both one-dimensional profile analysis and two-dimensional object-oriented analysis algorithms have been implemented as ArcGIS extension modules. Embedding these algorithms into ArcGIS software allows users to be able to take advantages of the existing powerful ArcGIS functions such as data management, visualization, and spatial analysis. The input raw LiDAR data can be directly loaded, displayed, and pre-processed using core functions of ArcGIS and specialized extensions developed by other organizations. The processed LiDAR datasets can be directly ingested by the volumetric analysis module and the beach profile analysis module. The morphological change analysis results can be immediately displayed and validated using the available ArcGIS

visualization functions. Also, the analysis results can be compared and integrated with other GIS data for map composition and further numerical analysis and modeling.

LiDAR technology makes it possible to create accurate and dense datasets for costal topography mapping and change analysis in a cost-effective manner. However, the LiDAR surveys also suffer from some limitations. For topographic LiDAR systems, the topography mapping in the near-shore zone is limited by its capability of penetrating water. In terms of temporal scale, a complete understanding of the changing coastal morphology may require more frequent surveys such as monthly or quarterly surveys spanning all seasons. The traditional ground survey approach is able to measure the beach up to the wading depth of the near-shore zone. It offers more flexibility in the choice of appropriate survey time. In this sense, the traditional techniques for coastal topography survey are still indispensable to validate, calibrate, and supplement LiDAR data. This research focuses on the methodology for characterizing and analyzing the coastal morphological changes based on airborne LiDAR data. By supplementing the LiDAR datasets with other data sources, the methodology developed in this research could be used to support the change analysis at various temporal scales, such as storm-related changes, seasonal variations, and the long-terms changes caused by sea level rise.

The visual interpretation and automated algorithms for beach profile analysis are complementary. The automated profile analysis algorithms are helpful in extracting information over a large geographic area and locating the area of interests, but visual interpretation is essential for determining reasonable thresholds, validating and adjusting the results from algorithms. In the future, based on the vector representation of cross-

shore morphological features and properties, other ancillary data sources could be incorporated to perform analysis such as conducting coastal classification, evaluating storm hazard vulnerability, as well as evaluating the impacts of human interventions on coastal morphology changes.

The pixel-based and object-based representations of elevation change patches are also complementary. The pixel-based representation provides spatially distributed information of erosion and deposition. The object-based representation is helpful in locating hot spots and classifying the change patches, but a detailed analysis within each erosion and deposition patches is based on the pixel-based elevation change information. In the future, other ancillary data sources such as multispectral remote sensing imagery could be incorporated to derive the thematic attributes of discrete change patches (object). This will be useful for achieving a better classification of change patches induced by various mechanisms and for gaining a better understanding of the causes and impacts of coastal morphological changes.

REFERENCES

Abramowitz, M., and I. A. Stegun. 1964. *Handbook of mathematical functions with formulas, graphs, and mathematical tables*. Washington, DC: U.S. National Bureau of Standards.

Batten, B. K., and N. C. Kraus. 2005. *Regional Morphology Analysis Package (BMAP), Part2: Users guide and tutorial*. Vicksburg, MS: U.S. Army Engineer Research and Development Center, Coastal and Hydraulics Laboratory.

Brennan, P., and M. Harlow. 2002. *Linear referencing in ArcGIS*. Redlands, CA: Environmental Systems Research Institute (ESRI).

Brock, J. C., W. B. Krabill, and A. H. Sallenger Jr. 2004. Barrier island morphodynamic classification based on LiDAR metrics for north Assateague Island, Maryland. *Journal of Coastal Research* 20 (2):498-509.

Burrough, P. A. 1981. Fractal dimension of landscape and other environmental data. *Nature* 294:240-242.

CCSR. 2006. *Mapping the future world population*. http://ccsr.columbia.edu/population/map/ (last accessed 31 August 2008).

Chaudhuri, D., and A. Samal. 2007. A simple method for fitting of bounding rectangle to closed regions. *Pattern Recognition* 40 (7):1981-1989.

Cooper, N. J., D. J. Leggett, and J. P. Lowe. 2000. Beach-profile measurement, theory and analysis: Practical guidance and applied case studies. *Water and Environment Journal* 14 (2):79-88.

Crossett, K. M., T. J. Culliton, P. C. Wiley, and T. R. Goodspeed. 2004. *Population trends along the coastal United States: 1980-2008*. Washington, DC: National Oceanographic and Atmospheric Administration.

Davis, J. C. 2002. *Statistics and data analysis in geology*, 3rd edition. New York: John Wiley & Sons, Inc.

Elko, N. A., A. H. Sallenger Jr, K. Guy, H. F. Stockdon, and K. L. M. Morgan. 2002. *Barrier island elevations relevant to potential storm impacts: 1. Techniques*. USGS Open File Report 02-287. Washington, DC: U.S. Geological Survey.

Finkl, C. W., L. Benedet, and J. L. Andrews. 2005. Interpretation of seabed geomorphology based on spatial analysis of high-density airborne laser bathymetry. *Journal of Coastal Research* 21 (3):501-514.

Flusser, J., and T. Suk. 1993. Pattern recognition by affine moment invariants. *Pattern Recognition* 26 (1):167-174.

Foroutan-pour, K., P. Cutilleul, and D. L. Smith. 1999. Advances in the implementation of the box-counting method of fractal dimension estimation. *Applied Mathematics and Computation* 105:195-210.

Gares, P. A., Y. Wang, and S. A. White. 2006. Using LiDAR to monitor a beach nourishment project at Wrightsville Beach, North Carolina, USA. *Journal of Coastal Research* 22 (5):1206-1219.

Graham, D., M. Sault, and C. Bailey. 2003. National ocean service shoreline: Past, present, and future. *Journal of Coastal Research* 38:14-32.

Halcrow.2008. *SANDS – Managing and understanding coastal data.* http://www.halcrow.com/sands/default.asp (last accessed 5 October 2008)

Hapke, C. J., D. Reid, B. M. Richmond, P. Ruggiero, and J. List. 2006. *National assessment of shoreline change, Part 3: Historical shoreline change and associated coastal land lost along sandy shorelines of the California coast.* USGS Open File Report 2006-1219. Washington, DC: U.S. Geological Survey.

Judge, E. K., M. F. Overton, and J. S. Fisher. 2003. Vulnerability indicators for coastal dunes. *Journal of Waterway, Port, Coastal and Ocean Engineering* 129 (6):270-278.

Lindeberg, T. 1994. Scale-space theory: A basic tool for analysing structures at different scales. *Journal of Applied Statistics* 21 (2):224-270.

Liu, H., and K. Jezek. 2004. Automated extraction of coastline from satellite imagery by integrating Canny edge detector and locally adaptive thresholding method. *International Journal of Remote Sensing* 25 (5):937-958.

Mandelbrot, B. B. 1983. *The fractal geometry of nature*. New York: W.H.Freeman and Company.

Mason, D. C., C. Gurney, and M. Kennett. 2000. Beach topography mapping - A comparison of techniques. *Journal of Coastal Conservation* 6:113-124.

Meredith, A. W., D. Eslinger, and D. Aurin. 1999. *An evaluation of hurricane-induced erosion along the North Carolina coast using airborne LiDAR surveys*. NOAA Coastal

Service Center Technical Report NOAA/CSC/99031-PUB/001.Washington, DC: National Oceanographic and Atmospheric Administration.

Morang, A., and L. E. Parson. 2002. *Coastal Engineering Manual, Part IV - Chapter 1: Coastal terminology and geologic environments*. Coastal Engineering Manual 1110-2-1100. Washington, DC: U.S. Army Coastal Engineering Research Center.

Mulchrone, K. F., and K. R. Choudhury. 2004. Fitting an ellipse to an arbitrary shape: Implications for strain analysis. *Journal of Structural Geology* 26 (1):143-153.

NOAA. 2008. *Remote sensing for coastal management*. http://www.csc.noaa.gov/crs/rs_apps/sensors/lidar.htm (last accessed 30 September 2008).

Robertson, W., K. Zhang, and D. Whitman. 2007. Hurricane-induced beach change derived from airborne laser measurements near Panama City, Florida. *Marine Geology* 237:191-205.

Rosin, P. L. 1993. Ellipse fitting by accumulating five points fits. *Pattern Recognition Letters* 14 (8):661-669.

Sallenger, A. H. 2000. Storm impact scale for barrier islands. *Journal of Coastal Research* 16 (3):890-895.

Sallenger, A. W., W. Krabill, R. Swift, J. Brock, J. List, M. Hansen, R. A. Holman, S. Manizade, J. Sontag, A. Meredith, K. Morgan, J. K. Yunkel, E. Frederick, and H. Stockdon. 2003. Evaluation of airborne scanning LiDAR for coastal change applications. *Journal of Coastal Research* 19 (1):125-133.

Schwartz, M. L. 2005. *Encyclopedia of coastal science*. Dordrecht, The Netherlands: Springer.

Shrestha, R. L., W. E. Carter, M. Sartori, B. J. Luzum, and K. C. Slatton. 2005. Airborne Laser Swath Mapping: Quantifying changes in sandy beaches over time scales of weeks to years. *ISPRS Journal of Photogrammetry and Remote Sensing* 59 (4):222-232.

Sonka, M., V. Hlavac, and R. Boyla. 1999. *Image processing, analysis, and machine vision, 2nd edition*. Pacific Grove, CA: Brooks/Cole Publishing Company.

Stockdon, H. F., A. H. Sallenger Jr, R. A. Holman, and P. A. Howd. 2007. A simple model for the spatially-variable coastal response to hurricanes. *Marine Geology* 238:1-20.

Suesse, H., and K. Voss. 2001. A new efficient algorithm for fitting of rectangles and squares. *Proceedings of IEEE International Conference on Image Processing 2*:809-812.

Teague, M. R. 1980. Image analysis via the general theory of moments. *Journal of the Optical Society of America* 70 (8):920-930.

Thornton, E. B., A. Sallenger, J. C. Sesto, L. Egley, T. McGee, and R. Parsons. 2006. Sand mining impacts on long-term dune erosion in southern Monterey Bay. *Marine Geology* 226:45-58.

USGS. 2008. *Storm-impact scale: First line of defense.* http://coastal.er.usgs.gov/hurricanes/impact-scale/measuringdhigh.html (last accessed 5 November 2008).

Veri-Tech. 2006. *CEDAS 4.01*. http://www.veritechinc.net/products/cedas/ (last accessed 2 October 2008).

White, S. A., and Y. Wang. 2003. Utilizing DEMs derived from LiDAR data to analyze morphologic change in the North Carolina coastline. *Remote Sensing of Environment* 85 (1):39-47.

Wise, R. A. 1995. *Beach Morphology Analysis Package (BMAP), Version1*. Vicksburg, MS: U.S. Army Engineer Research and Development Center, Coastal and Hydraulics Laboratory.

Witkin, A. P. 1983. Scale-space filtering. *Proceedings of International Joint Conference on Artificial Intelligence 2*:1019-1022.

Woolard, J. W., and J. D. Colby. 2002. Spatial characterization, resolution, and volumetric change of coastal dunes using airborne LiDAR: Cape Hatteras, North Carolina. *Geomorphology* 48:269-287.

Zhang, K., D. Whitman, S. Leatherman, and W. Robertson. 2005. Quantification of beach changes caused by Hurricane Floyd along Florida's Atlantic coast using airborne laser surveys. *Journal of Coastal Research* 21 (1):123-134.

VITA

Name: Yige Gao

Address: Department of Geography, Texas A&M University
Room 810, Eller O&M Building, College Station, Texas 77843-3147

Email address: yige@geog.tamu.edu

Education: B.S., Geographical Information System, Peking University, China, 2005

B.S. (Double degree), Mathematics and Applied Mathematics, Peking University, China, 2005

M.S., Geography, Texas A&M University, 2009